Solving Inverse Problems via Diffusion-Based Priors: An Approximation-Free Ensemble Sampling Approach

Anonymous authors
Paper under double-blind review

Abstract

Diffusion models (DMs) have proven to be effective in modeling high-dimensional distributions, leading to their widespread adoption for representing complex priors in Bayesian inverse problems (BIPs). However, current DM-based posterior sampling methods proposed for solving common BIPs rely on heuristic approximations to the generative process. To exploit the generative capability of DMs and avoid the usage of such approximations, we propose an ensemble-based algorithm that performs posterior sampling without the use of heuristic approximations. Our algorithm is motivated by existing work that combines DM-based methods with the sequential Monte Carlo (SMC) method. By examining how the prior evolves through the diffusion process encoded by the pre-trained score function, we derive a modified partial differential equation (PDE) governing the evolution of the corresponding posterior distribution. This PDE includes a modified diffusion term and a reweighting term, which can be simulated via stochastic weighted particle methods. Theoretically, we prove that the error between the true posterior distribution can be bounded in terms of the training error of the pre-trained score function and the number of particles in the ensemble. Empirically, we validate our algorithm on several inverse problems in imaging to show that our method gives more accurate reconstructions compared to existing DM-based methods.

1 Introduction

Inverse problems are fundamentally challenging tasks that span multiple scientific and engineering fields like fluid dynamics (Cotter et al., 2009; Sellier, 2016), geophysics (Richter, 2021), medical imaging (Lustig et al., 2007), microscopy (Choi et al., 2007; Bertero et al., 2021), etc. These problems basically involve reconstructing an unknown parameter x from incomplete and noise-corrupted measurements y. Due to the inherent limitations in measurements, there is often substantial uncertainty in determining the true parameter x. Instead of pursuing a single point estimate, a more principled approach involves adopting a Bayesian framework, where we specify a prior distribution on x and characterize the uncertainty through posterior sampling of $p(x|y)$. However, these high-dimensional and multi-modal posterior distributions typically present significant computational challenges, with which traditional Markov chain Monte Carlo (MCMC) methods (Neal et al., 2011; Welling & Teh, 2011; Cui et al., 2016) often struggle, primarily due to metastability, *i.e.*, the difficulty in transitioning between distinct high-probability modes that are separated by regions of low probability.

To overcome these limitations, deep generative models have been proposed for encoding prior distributions, notably normalizing flows (NFs) (Asim et al., 2020; Hou et al., 2019; Zhang et al., 2021; Whang et al., 2021b;a; Hagemann et al., 2022) and generative adversarial networks (GANs) (Patel & Oberai, 2019; Bora et al., 2017). Recently, Diffusion models (DMs) and probability flow-based models (Albergo et al., 2023b; Albergo & Vanden-Eijnden, 2022; Lipman et al., 2022; Liu et al., 2022b; Sohl-Dickstein et al., 2015; Ho et al., 2020; Song et al., 2020a; 2021a; Song & Ermon, 2019; Song et al., 2020b; Zhang et al., 2018a) have emerged as leading methods in modern generative modeling. These models generate samples from a high-dimensional target distribution p_0 by inverting a diffusion process that transforms the target distribution $\boldsymbol{x}_0 \sim p_0$ into a simple distribution $\boldsymbol{x}_T \sim p_T$ (typically Gaussian). The effectiveness of DMs has led to their adoption as prior distributions in inverse problems, spawning various DM-based posterior sampling methods (Chung et al.,

2022; Song et al., 2023b; Wu et al., 2023; Cardoso et al., 2023; Dou & Song, 2024; Sun et al., 2024; Xu & Chi, 2024; Wu et al., 2024c; Bruna & Han, 2024). For a comprehensive review, we refer the readers to either Appendix A.1 or (Daras et al., 2024a). These methods can be categorized into two main approaches:

1. Methods that leverage Bayes' formula to construct a conditional diffusion model using a pre-trained score function associated with the prior distribution: Specifically, for any time $t \in [0, T]$, applying Bayes' formula $p_t(\boldsymbol{x}_t|\boldsymbol{y}) \propto p_t(\boldsymbol{x}_t)p_t(\boldsymbol{y}|\boldsymbol{x}_t)$ yields

$$\nabla_{\boldsymbol{x}} \log p_t(\boldsymbol{x}_t|\boldsymbol{y}) = \nabla_{\boldsymbol{x}} \log p_t(\boldsymbol{x}_t) + \nabla_{\boldsymbol{x}} \log p_t(\boldsymbol{y}|\boldsymbol{x}_t). \tag{1.1}$$

   To implement this approach, one needs to evaluate the left-hand side of (1.1), which is known as the conditional score function and defines a reverse-time diffusion process from $p_T(\boldsymbol{x}_T|\boldsymbol{y})$ to $p_0(\boldsymbol{x}_0|\boldsymbol{y})$. The first term on the right-hand side is the score function from the pre-trained DM modeling the prior distribution. The second term requires evaluating an integral $p_t(\boldsymbol{y}|\boldsymbol{x}_t) = \int p(\boldsymbol{y}|\boldsymbol{x}_0)p_{0|t}(\boldsymbol{x}_0|\boldsymbol{x}_t)\mathrm{d}\boldsymbol{x}_0$ over all possible $\boldsymbol{x}_0$'s that could lead to $\boldsymbol{x}_t$ through the pre-trained DM, to address which methods in this category employ various approximations for $\nabla_x \log p_t(\boldsymbol{y}|\boldsymbol{x}_t)$.

   Among different methods belonging to this approach, one group of methods (Song et al., 2020b; Choi et al., 2021; Song et al., 2021b; Chung et al., 2022; Song et al., 2023b; Boys et al., 2023; Wu et al., 2023) makes simplifying assumptions, while others (Choi et al., 2021; Wang et al., 2022; Kawar et al., 2022; Rout et al., 2023) use empirically constructed updates without structured assumptions. These heuristic, problem-specific approximations might be inaccurate in certain scenarios. In particular, for the setting of linear inverse problems modeled by $\boldsymbol{y} = \boldsymbol{A}\boldsymbol{x} + \boldsymbol{n}$ with $\boldsymbol{y} \in \mathbb{R}^m$, $\boldsymbol{x} \in \mathbb{R}^n$, $\boldsymbol{A} \in \mathbb{R}^{m \times n}$ and $\boldsymbol{n} \sim \mathcal{N}(\boldsymbol{0}, \sigma^2 \boldsymbol{I}_m)$, examples of approximations to the term $\nabla_x \log p_t(\boldsymbol{y}|\boldsymbol{x}_t)$ used in existing work include but not limit to ILVR (Choi et al., 2021) and DPS (Chung et al., 2022):

$$\nabla_{\boldsymbol{x}} \log p_t(\boldsymbol{y}|\boldsymbol{x}_t) \approx -\left(\boldsymbol{A}^{\mathsf{T}}\boldsymbol{A}\right)^{-1}\boldsymbol{A}^{\mathsf{T}}\left(\boldsymbol{y} - \boldsymbol{A}\boldsymbol{x}_t\right), \tag{ILVR}$$

$$\nabla_{\boldsymbol{x}} \log p_t(\boldsymbol{y}|\boldsymbol{x}_t) \approx \left(\boldsymbol{I}_n + \nabla_{\boldsymbol{x}}^2 \log p_t(\boldsymbol{x}_t)\right)^{\mathsf{T}}\boldsymbol{A}^{\mathsf{T}}\left(\boldsymbol{y} - \boldsymbol{A}\mathbb{E}\left[\boldsymbol{x}_0|\boldsymbol{x}_t\right]\right). \tag{DPS}$$

2. Approximation-free methods that integrate DMs with traditional posterior sampling methods: Examples include split Gibbs sampler (SGS) + DM methods (Xu & Chi, 2024; Wu et al., 2024c; Coeurdoux et al., 2024; Zheng et al., 2025), which are built upon the split Gibbs sampler for Bayesian inference (Vono et al., 2019; Pereyra et al., 2023), and sequential Monte Carlo (SMC) + DM methods (Wu et al., 2023; Cardoso et al., 2023; Dou & Song, 2024; Kelvinius et al., 2025; Skreta et al., 2025; Lee et al., 2025; Holderrieth et al., 2025; Achituve et al., 2025), which combine DMs with SMC (Liu, 2001; Chopin, 2002; Del Moral et al., 2006; Doucet et al., 2009; Del Moral, 2013; Moral, 2004) to obtain asymptotically consistent posterior samples.

We advance the second approach by introducing a novel ensemble-based *Approximation-Free Diffusion Posterior Sampler (AFDPS)*. Our method enhances the synergy between DMs and SMC methods, which use weighted particle ensembles and strategic resampling to approximate the posterior distribution. The key innovation stems from our principled utilization of pre-trained DMs for prior evolution and our derivation of the exact partial differential equation (PDE) governing the corresponding posterior evolution, which reveals fundamentally distinct dynamics compared to existing approaches. Leveraging the flexibility of our framework, we propose two different approaches based on SDE and ODE+Corrector, respectively. Through careful analysis of the discrepancy between the derived PDE dynamics and the time-reversal of the true diffusion process, we establish error bounds for our posterior sampling algorithm based on stochastic weighted particle method. In practice, our algorithm demonstrates versatile compatibility with various pre-trained diffusion models. Extensive experiments on various imaging inverse problems are provided to demonstrate the effectiveness of our method.

Our Contributions. We summarize our main contributions as follows:

- We propose a novel ensemble-based posterior sampling method that integrates sequential Monte Carlo with diffusion models to achieve **exact posterior sampling without heuristic approximations**, founded on rigorously derived, previously unexplored, and more flexible PDE dynamics.

- We provide comprehensive theoretical guarantees demonstrating that our ensemble-based algorithm, implemented via stochastic weighted particle methods, **converges asymptotically to the derived PDE dynamics**. We additionally derive **precise error bounds** relating posterior sampling accuracy to the quality of the pre-trained score function.
- We empirically evaluate our method on multiple imaging inverse problems using large-scale datasets like FFHQ-256 (Karras et al., 2019) and ImageNet-256 (Deng et al., 2009), showing that our method **achieves better reconstruction quality** over existing methods.

2 Preliminaries

In this section, we provide a quick overview of problem setup, basic concepts, and existing work related to solving Bayesian inverse problems (BIPs) with diffusion models.

2.1 Basics of Inverse Problems

In BIPs, we aim to recover a ground truth parameter $\boldsymbol{x}$ from measurements $\boldsymbol{y}$. The relationship between $\boldsymbol{x}$ and $\boldsymbol{y}$ is described by:

$$\boldsymbol{y} = \mathcal{A}(\boldsymbol{x}) + \boldsymbol{n}, \tag{2.1}$$

where $\boldsymbol{x} \in \mathbb{R}^n$, $\boldsymbol{y} \in \mathbb{R}^m$, $\mathcal{A} : \mathbb{R}^n \to \mathbb{R}^m$ is a differentiable forward operator (linear or nonlinear), and $\boldsymbol{n} \in \mathbb{R}^m$ represents measurement noise. Under the Bayesian framework, the posterior distribution we seek to sample from is:

$$p(\boldsymbol{x}|\boldsymbol{y}) \propto p_0(\boldsymbol{x})p(\boldsymbol{y}|\boldsymbol{x}) = p_0(\boldsymbol{x}) \exp(-\mu_{\boldsymbol{y}}(\boldsymbol{x})), \tag{2.2}$$

where $p_0(\boldsymbol{x})$ denotes the prior distribution and $\mu_{\boldsymbol{y}}(\boldsymbol{x}) = -\log p(\boldsymbol{y}|\boldsymbol{x})$ is the negative log-likelihood function for a fixed observation $\boldsymbol{y}$.

Many practical inverse problems are ill-posed due to measurement noise and non-injective forward models, making unique solutions impossible to obtain. Traditional optimization-based methods often fail to capture the complex solution landscape, motivating the use of Bayesian formulations where posterior sampling methods can systematically account for uncertainty and explore multiple plausible solutions. For a comprehensive treatment of BIPs, we refer readers to (Stuart, 2010).

Deep generative models have emerged as powerful prior distributions that can capture complex solution spaces while remaining computationally tractable. Unlike traditional priors that rely on structural assumptions, these models effectively represent high-dimensional and multi-modal distributions given sufficient training data. In this work, we focus on diffusion models (DMs), which represent the current state-of-the-art in generative modeling with successful applications across physics (Cotler & Rezchikov, 2023; Habibi et al., 2024; Zhu et al., 2024c), chemistry (Xu et al., 2022; Alakhdar et al., 2024; Riesel et al., 2024), biology (Alamdari et al., 2023; Watson et al., 2023), computer vision (Rombach et al., 2022; Chan et al., 2024), and natural language processing (Li et al., 2022b).

2.2 Diffusion Models: the EDM Framework

We adopt the Elucidating the design space of Diffusion Models (EDM) framework from (Karras et al., 2022) to model prior distributions. The EDM framework provides a unified approach for the design of diffusion models by systematically analyzing noise schedules, sampling algorithms, and training objectives.

Building on the continuous formulation of diffusion models (Song et al., 2020b), the framework starts off with a forward diffusion process governed by the stochastic differential equation (SDE):

$$\mathrm{d}\boldsymbol{x}_s = F(s)\boldsymbol{x}_s\mathrm{d}s + G(s)\mathrm{d}\boldsymbol{w}_s. \tag{2.3}$$

where $(\boldsymbol{w}_s)_{s \geq 0}$ is a standard Brownian motion and p_s denotes the distribution of $\boldsymbol{x}_s$, with p_0 being the prior distribution from (2.2). Following (Anderson, 1982), the corresponding reverse-time SDE is:

$$\mathrm{d}\bar{\boldsymbol{x}}_t = \left[-F(t)\bar{\boldsymbol{x}}_t + \frac{G(t)^2 + V(t)^2}{2} \nabla_{\boldsymbol{x}} \log \bar{p}_t(\bar{\boldsymbol{x}}_t) \right] \mathrm{d}t + V(t)\mathrm{d}\boldsymbol{w}_t, \tag{2.4}$$

where $\breve{p}_0 = p_T$, $\breve{p}_T = p_0$, $\breve{*}_t$ denotes $*_{T-t}$, and $V : \mathbb{R} \to \mathbb{R}$ is a scalar-valued function. The score function $\nabla \log \breve{p}_t(\boldsymbol{x})$ is typically approximated by a neural network $\boldsymbol{\phi}_\theta(\boldsymbol{x}, t)$ trained via score matching (Hyvärinen & Dayan, 2005; Vincent, 2011). We use $\widehat{\breve{\boldsymbol{x}}}_t$ and $\widehat{\breve{p}}_t$ to denote the particle trajectory and its distribution when using the approximated score function $\boldsymbol{\phi}_\theta(\boldsymbol{x}, t)$, with $\widehat{\breve{p}}_0$ being exactly Gaussian and $\widehat{\breve{p}}_T$ approximating the target distribution p_0.

The EDM framework reparameterizes the drift coefficient $F(t)$ and diffusion coefficient $G(t)$ using

$$s(t) := \exp\left(\int_0^t F(\xi)\mathrm{d}\xi\right) \quad \text{and} \quad \sigma(t) := \sqrt{\int_0^t \frac{G(\xi)^2}{s(\xi)^2}\mathrm{d}\xi},$$

yielding $F(t) = \frac{\dot{s}(t)}{s(t)}$ and $G(t) = s(t)\sqrt{2\dot{\sigma}(t)\sigma(t)}$. This reparameterization enables more accurate score estimation under appropriate choices of s and σ, as demonstrated empirically in (Karras et al., 2022) and theoretically in (Wang et al., 2024). Also, the framework allows for different implementations based on the choice of diffusion coefficient V. Setting $V(t) = G(t) = s(t)\sqrt{2\dot{\sigma}(t)\sigma(t)}$ yields the SDE implementation:

$$\mathrm{d}\widehat{\breve{\boldsymbol{x}}}_t = \left[-\frac{\dot{s}(t)}{s(t)}\widehat{\breve{\boldsymbol{x}}}_t + 2s(t)^2\dot{\sigma}(t)\sigma(t)\boldsymbol{\phi}_\theta(\widehat{\breve{\boldsymbol{x}}}_t, t)\right]\mathrm{d}t + s(t)\sqrt{2\dot{\sigma}(t)\sigma(t)}\mathrm{d}\boldsymbol{w}_t. \tag{2.5}$$

Alternatively, setting $V(t) = 0$ yields the probability-flow ODE (PF-ODE) implementation:

$$\mathrm{d}\widehat{\breve{\boldsymbol{x}}}_t = \left[-\frac{\dot{s}(t)}{s(t)}\widehat{\breve{\boldsymbol{x}}}_t + s(t)^2\dot{\sigma}(t)\sigma(t)\boldsymbol{\phi}_\theta(\widehat{\breve{\boldsymbol{x}}}_t, t)\right]\mathrm{d}t. \tag{2.6}$$

3 Methodology

In this section, we present the key derivation underlying our posterior sampling algorithm. Our approach can be interpreted as solving a high-dimensional PDE that governs posterior distribution evolution using either the (stochastic) weighted particle method (Degond & Mas-Gallic, 1989; Degond & Mustieles, 1990; Rjasanow & Wagner, 1996; Bossy & Talay, 1997; Talay & Vaillant, 2003; Raviart, 2006; Chertock, 2017) or the SMC method (Chopin, 2002; Del Moral et al., 2006; Doucet et al., 2009; Del Moral, 2013; Moral, 2004). Throughout the derivation, we assume the log-likelihood function $\mu_{\boldsymbol{y}}(\boldsymbol{x})$ is at least twice differentiable w.r.t. $\boldsymbol{x}$ for fixed $\boldsymbol{y}$. Details of both algorithmic variants are given in the pseudocode in subsection 3.2.

3.1 Algorithm Outline

Following the setting in Section 2, we assume the prior distribution $p(\boldsymbol{x})$ is represented by a DM under the EDM framework. Specifically, $p_0(\boldsymbol{x})$ is approximated by $\widehat{\breve{p}}_T(\boldsymbol{x})$, obtained by simulating (2.5) or (2.6) from a Gaussian $\widehat{\breve{p}}_0$. We define the time-dependent posterior distribution as:

$$\widehat{q}_{\boldsymbol{y}}(\boldsymbol{x}, t) := \frac{\widehat{\breve{p}}_t(\boldsymbol{x})e^{-\mu_{\boldsymbol{y}}(\boldsymbol{x})}}{\int_{\mathbb{R}^n} \widehat{\breve{p}}_t(\boldsymbol{x})e^{-\mu_{\boldsymbol{y}}(\boldsymbol{x})}\mathrm{d}\boldsymbol{x}} := \frac{\widehat{Q}_{\boldsymbol{y}}(\boldsymbol{x}, t)}{\widehat{Z}_{\boldsymbol{y}}(t)}, \tag{3.1}$$

where $\widehat{Q}_{\boldsymbol{y}}(\boldsymbol{x}, t) = \widehat{\breve{p}}_t(\boldsymbol{x})e^{-\mu_{\boldsymbol{y}}(\boldsymbol{x})}$ is the unnormalized posterior, and $\widehat{Z}_{\boldsymbol{y}}(t) = \int_{\mathbb{R}^n} \widehat{Q}_{\boldsymbol{y}}(\boldsymbol{x}, t)\mathrm{d}\boldsymbol{x}$ is the normalizing constant.

Our algorithm consists of the following two stages:
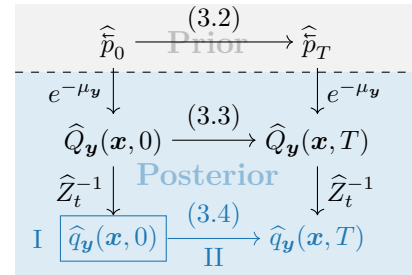

Figure 1: A roadmap for our posterior sampling method. I, II refers to the two stages of the proposed algorithm.

Stage I: Sample from the initial distribution $\widehat{q}_{\boldsymbol{y}}(\boldsymbol{x}, 0)$.
We first sample from $\widehat{q}_{\boldsymbol{y}}(\boldsymbol{x}, 0) \propto \widehat{\breve{p}}_0(\boldsymbol{x})e^{-\mu_{\boldsymbol{y}}(\boldsymbol{x})}$, which is analogous to the likelihood step in (Wu et al., 2024c). Given differentiable $\mu_{\boldsymbol{y}}(\boldsymbol{x})$, we can employ well-known gradient-based samplers like Metropolis Adjusted Langevin Algorithm (MALA) (Roberts & Stramer, 2002), Annealed Importance Sampling (AIS) (Neal, 2001), or more advanced methods (Lu et al., 2019b; Tan & Lu, 2023; Chen & Ying, 2024a; Lindsey et al., 2022). For linear BIPs with Gaussian noise, where $\mathcal{A} := \boldsymbol{A} \in \mathbb{R}^{m \times n}$ and $\boldsymbol{n} \sim \mathcal{N}(\boldsymbol{0}, \boldsymbol{\Sigma})$, assuming $\widehat{\breve{p}}_0 = \mathcal{N}(\boldsymbol{0}, \rho^2\boldsymbol{I}_n)$, the initial distribution simplifies to:

$$\widehat{q}_{\boldsymbol{y}}(\boldsymbol{x}, 0) \propto \exp\left(-(\boldsymbol{y} - \boldsymbol{A}\boldsymbol{x})^\intercal\boldsymbol{\Sigma}^{-1}(\boldsymbol{y} - \boldsymbol{A}\boldsymbol{x}) - \frac{1}{2\rho^2}\|\boldsymbol{x}\|_2^2\right) = \mathcal{N}(\boldsymbol{\gamma}, \boldsymbol{\Lambda}^{-1}),$$

where $\boldsymbol{\Lambda} = \boldsymbol{A}^{\intercal}\boldsymbol{\Sigma}^{-1}\boldsymbol{A} + \frac{1}{\rho^2}\boldsymbol{I}_n$ and $\boldsymbol{\gamma} = \boldsymbol{\Lambda}^{-1}\boldsymbol{A}^{\intercal}\boldsymbol{\Sigma}^{-1}\boldsymbol{y}$.

Stage II: Solve the PDE dynamics governing the posterior evolution. Below we first derive the PDE dynamics $(\widehat{Q}_{\boldsymbol{y}}(\boldsymbol{x},t))_{t\in[0,T]}$ based on the diffusion process (2.4) from $(\widehat{\overline{p}}_t)_{t\in[0,T]}$. Then normalizing these dynamics yields the PDE that evolves $(\widehat{q}_{\boldsymbol{y}}(\boldsymbol{x},t))_{t\in[0,T]}$, as illustrated in Figure 1.

1. The Fokker-Planck equation evolving from $\widehat{\overline{p}}_0$ to $\widehat{\overline{p}}_T$ is:

$$\frac{\partial}{\partial t}\widehat{\overline{p}}_t = -\nabla_{\boldsymbol{x}} \cdot \left(\left(-F(t)\boldsymbol{x} + \frac{G(t)^2+V(t)^2}{2}\boldsymbol{\phi}_\theta(\boldsymbol{x},t)\right)\widehat{\overline{p}}_t\right) + \frac{1}{2}V(t)^2\Delta_{\boldsymbol{x}}\widehat{\overline{p}}_t. \tag{3.2}$$

2. Substituting $\widehat{\overline{p}}_t(\boldsymbol{x}) = \widehat{Q}_{\boldsymbol{y}}(\boldsymbol{x},t)\exp(\mu_{\boldsymbol{y}})$ into (3.2) yields:

$$\begin{aligned}
\frac{\partial}{\partial t}\widehat{Q}_{\boldsymbol{y}} = & -\nabla_{\boldsymbol{x}} \cdot \left(\left(\widehat{\boldsymbol{H}}(\boldsymbol{x},t) - V(t)^2\nabla_{\boldsymbol{x}}\mu_{\boldsymbol{y}}\right)\widehat{Q}_{\boldsymbol{y}}\right) + \frac{1}{2}V(t)^2\Delta_x\widehat{Q}_{\boldsymbol{y}} \\
& + \left(\frac{1}{2}V(t)^2\left(\|\nabla_{\boldsymbol{x}}\mu_{\boldsymbol{y}}\|_2^2 - \Delta_{\boldsymbol{x}}\mu_{\boldsymbol{y}}\right) - \widehat{\boldsymbol{H}}(\boldsymbol{x},t)^{\intercal}\nabla_{\boldsymbol{x}}\mu_{\boldsymbol{y}}\right)\widehat{Q}_{\boldsymbol{y}},
\end{aligned} \tag{3.3}$$

where $\widehat{\boldsymbol{H}}(\boldsymbol{x},t) := -F(t)\boldsymbol{x} + \frac{G(t)^2+V(t)^2}{2}\boldsymbol{\phi}_\theta(\boldsymbol{x},t)$ is the original drift. A complete derivation of (3.3) is postponed to Lemma B.1 in Appendix B.

3. Defining $U(\boldsymbol{x},t) := \frac{1}{2}V(t)^2\left(\|\nabla_{\boldsymbol{x}}\mu_{\boldsymbol{y}}\|_2^2 - \Delta_{\boldsymbol{x}}\mu_{\boldsymbol{y}}\right)$, we have the following PDE for $\widehat{q}_{\boldsymbol{y}}(\boldsymbol{x},t)$:

PDE Dynamics for Posterior Evolution

$$\begin{aligned}
\frac{\partial}{\partial t}\widehat{q}_{\boldsymbol{y}} = & -\nabla_{\boldsymbol{x}} \cdot \left(\left(\widehat{\boldsymbol{H}}(\boldsymbol{x},t) - V(t)^2\nabla_{\boldsymbol{x}}\mu_{\boldsymbol{y}}\right)\widehat{q}_{\boldsymbol{y}}\right) + \frac{1}{2}V(t)^2\Delta_x\widehat{q}_{\boldsymbol{y}} \\
& + \left(U(\boldsymbol{x},t) - \widehat{\boldsymbol{H}}(\boldsymbol{x},t)^{\intercal}\nabla_{\boldsymbol{x}}\mu_{\boldsymbol{y}} - \int_{\mathbb{R}^n}\left(U(\boldsymbol{x},t) - \widehat{\boldsymbol{H}}(\boldsymbol{x},t)^{\intercal}\nabla_{\boldsymbol{x}}\mu_{\boldsymbol{y}}\right)\widehat{q}_{\boldsymbol{y}}\mathrm{d}\boldsymbol{x}\right)\widehat{q}_{\boldsymbol{y}}.
\end{aligned} \tag{3.4}$$

This derivation involves averaging the linear term in (3.3), a technique used in recent works (Skreta et al., 2025; Lee et al., 2025; Holderrieth et al., 2025). For a complete proof one may refer to Lemma B.2 in Appendix B.

3.2 Posterior Sampling via Weighted Particles

We now present two ensemble-based posterior samplers within the SMC framework, which can also be interpreted as solving the PDE (3.4) numerically via (stochastic) weighted particles.

(Stochastic) Weighted Particle / Sequential Monte Carlo Methods. As shown in Lemma B.4 of Appendix B, the posterior evolution (3.4) can be simulated via the following dynamics of a single weighted particle $(\boldsymbol{x}_t, \beta_t)$:

$$\begin{cases}
\mathrm{d}\boldsymbol{x}_t &= \left(\widehat{\boldsymbol{H}}(\boldsymbol{x}_t,t) - V(t)^2\nabla_{\boldsymbol{x}}\mu_{\boldsymbol{y}}(\boldsymbol{x}_t)\right)\mathrm{d}t + V(t)\mathrm{d}\boldsymbol{w}_t, \\
\mathrm{d}\beta_t &= \left(U(\boldsymbol{x}_t,t) - \widehat{\boldsymbol{H}}(\boldsymbol{x}_t,t)^{\intercal}\nabla_{\boldsymbol{x}}\mu_{\boldsymbol{y}}(\boldsymbol{x}_t)\right)\beta_t\mathrm{d}t \\
&\quad - \left(\int_{\mathbb{R}^n}\left(U(\boldsymbol{x},t) - \widehat{\boldsymbol{H}}(\boldsymbol{x},t)^{\intercal}\nabla_{\boldsymbol{x}}\mu_{\boldsymbol{y}}(\boldsymbol{x})\right)(P_\beta\gamma_t)(\boldsymbol{x})\mathrm{d}\boldsymbol{x}\right)\beta_t\mathrm{d}t,
\end{cases} \tag{3.5}$$

where $\gamma_t(\boldsymbol{x},\beta)$ denotes the joint probability distribution of $(\boldsymbol{x}_t, \beta_t)$ and $P_\beta\gamma_t(\boldsymbol{x}) := \int_{\mathbb{R}}\beta\gamma_t(\boldsymbol{x},\beta)\mathrm{d}\beta$ denotes the weighted projection of γ_t onto $\boldsymbol{x}$. To effectively approximate the integral in $P_\beta\gamma_t$, we then use the empirical measure $\gamma_t(\boldsymbol{x},\beta) \approx \frac{1}{N}\sum_{i=1}^N \delta_{(\boldsymbol{x}_t^{(i)},\beta_t^{(i)})}$ formed by N weighted particles to approximate $\gamma_t(\boldsymbol{x},\beta)$. This leads to the following joint dynamics for $\{(\boldsymbol{x}_t^{(i)},\beta_t^{(i)})\}_{i=1}^N$:

Weighted Particle Dynamics for Posterior Evolution

$$
\begin{cases}
\mathrm{d}\boldsymbol{x}_t^{(i)} &= \left(\widehat{\boldsymbol{H}}(\boldsymbol{x}_t^{(i)}, t) - V(t)^2 \nabla_{\boldsymbol{x}} \mu_{\boldsymbol{y}}(\boldsymbol{x}_t^{(i)}) \right) \mathrm{d}t + V(t) \mathrm{d}\boldsymbol{w}_t^{(i)}, \\
\mathrm{d}\beta_t^{(i)} &= \left(U(\boldsymbol{x}_t^{(i)}, t) - \widehat{\boldsymbol{H}}(\boldsymbol{x}_t^{(i)}, t)^{\intercal} \nabla_{\boldsymbol{x}} \mu_{\boldsymbol{y}}(\boldsymbol{x}_t^{(i)}) \right) \beta_t^{(i)} \mathrm{d}t \\
&\quad - \left(\frac{1}{N} \sum_{j=1}^{N} \left(U(\boldsymbol{x}_t^{(j)}, t) - \widehat{\boldsymbol{H}}(\boldsymbol{x}_t^{(j)}, t)^{\intercal} \nabla_{\boldsymbol{x}} \mu_{\boldsymbol{y}}(\boldsymbol{x}_t^{(j)}) \right) \beta_t^{(j)} \right) \beta_t^{(i)} \mathrm{d}t,
\end{cases}
\tag{3.6}
$$

with initial conditions $\boldsymbol{x}_0^{(i)} \sim \widehat{q}_{\boldsymbol{y}}(\cdot, 0)$ and $\beta_0^{(i)} = 1$, for $i \in [N]$. The weighted projection equals $\frac{1}{N} \beta_t^{(j)}$ when $\boldsymbol{x} = \boldsymbol{x}_t^{(j)}$ for some j, and zero otherwise.

Algorithm 1: Resampling Step

Input: Threshold $c \in (0, 1)$, weighted particles $\{(\boldsymbol{x}^{(j)}, \beta^{(j)})\}_{j=1}^{N}$
Output: Updated particles $\{(\widehat{\boldsymbol{x}}^{(j)}, \widehat{\beta}^{(j)})\}_{j=1}^{N}$

1 **if** $ESS = \dfrac{\left(N^{-1} \sum_{j=1}^{N} \beta^{(j)} \right)^2}{N^{-1} \sum_{j=1}^{N} (\beta^{(j)})^2} < c$ **then**

2 $\quad$ Sample $\{\widehat{\boldsymbol{x}}^{(j)}\}_{j=1}^{N}$ with replacement from $\{\boldsymbol{x}^{(j)}\}_{j=1}^{N}$ with probability $\left\{ \dfrac{\beta^{(j)}}{\sum_{i=1}^{N} \beta^{(i)}} \right\}_{j=1}^{N}$;

3 $\quad \widehat{\beta}^{(j)} \leftarrow 1$, for $j \in [N]$;

4 **else**

5 $\quad \{(\widehat{\boldsymbol{x}}^{(j)}, \widehat{\beta}^{(j)})\}_{j=1}^{N} \leftarrow \{(\boldsymbol{x}^{(j)}, \beta^{(j)})\}_{j=1}^{N}$;

6 **end**

While numerical discretization of (3.6) yields a prototypical sampling algorithm, the particle weights $\beta_t^{(i)}$ may diverge during simulation, reducing the ensemble's Effective Sample Size (ESS). To address this, we employ a resampling strategy commonly used in the SMC methods (Liu, 2001; Chopin, 2002; Del Moral et al., 2006; Doucet et al., 2009; Del Moral, 2013; Moral, 2004), whose detailed description is provided in Algorithm 1. Such resampling sub-routine essentially performs global moves by eliminating low-weight particles and duplicating high-weight ones, similar to the birth-death process used in (Moral, 2004; Lu et al., 2019b; Tan & Lu, 2023; Chen & Ying, 2024a; Lindsey et al., 2022). However, the resampling approach is computationally more efficient as the weight dynamics (3.6) can be parallelized.

SDE Approach (AFDPS-SDE). We first consider the SDE implementation (2.5) of the diffusion model, where $V(t) = G(t) = s(t)\sqrt{2\dot{\sigma}(t)\sigma(t)}$. We directly discretize (3.6) with an Euler-Maruyama scheme and add Algorithm 1 as an adjustment step at the end of each iteration, which leads to Algorithm 2. We have omitted the averaging term, *i.e.*, the last line of (3.6) in Algorithm 2, in practical implementation since the update is the same for all particles and therefore cancels out when we normalize the weights. Such cancellation property also holds for the ODE approach presented below. For high-dimensional problems, we can further reduce the computational cost of both the SDE and the ODE approach via practical techniques like using a smaller ensemble, omitting the resampling step, and simply returning the particle with the highest weight as the best estimator, as discussed in Appendix D.

ODE+Corrector Approach (AFDPS-ODE). Next, we consider an alternative implementation based on the probability flow ODE (2.6) by setting $V(t) = 0$. While this leads to the ODE dynamics (3.6), relying solely on deterministic evolution may not sufficiently explore the target distribution. To enhance exploration, we incorporate a stochastic corrector step inspired by predictor-corrector schemes in diffusion models (Song et al., 2020b; Chen et al., 2024c; Bradley & Nakkiran, 2024). The corrector uses the Unadjusted Langevin Algorithm (ULA, Algorithm 3) to draw samples from the intermediate posterior distribution $\widehat{q}_{\boldsymbol{y}}(\boldsymbol{x}, t) \propto \widehat{\overline{p}}_t(\boldsymbol{x}) \exp(-\mu_{\boldsymbol{y}}(\boldsymbol{x}))$ at each timestep. The complete ODE+Corrector algorithm (Algorithm 4) is thus obtained by discretizing the probability flow ODE (3.6), and applying both resampling (Algorithm 1) and ULA correction (Algorithm 3) steps for adjustments.

Algorithm 2: Approximation-Free Diffusion Posterior Sampler via SDE (AFDPS-SDE)

Input: Noisy observation $\boldsymbol{y}$, log-likelihood $\mu_{\boldsymbol{y}}(\cdot)$, functions $s(t)$ and $\sigma(t)$, time grid $\{t_i\}_{i=0}^{K}$ with $t_0 = 0$ and $t_K = T$, thresholds $\{c_l\}_{l=1}^{K}$, score function $\boldsymbol{\phi}_\theta(\cdot, t)$, ensemble size N, initial weights $\beta_0^{(j)} = 1$ for $j \in [N]$.

Output: Posterior approximation $\sum_{j=1}^{N} \beta_T^{(j)} \delta_{\boldsymbol{x}_T^{(j)}} / \sum_{j=1}^{N} \beta_T^{(j)}$.

1 Draw $\{\boldsymbol{x}_0^{(i)}\}_{i=1}^{N}$ i.i.d. from $\widehat{q}_{\boldsymbol{y}}(\cdot, 0)$ via Stage I samplers in Section 3.1;

2 for $k = 0$ **to** $K - 1$ **do**

3   Draw $\{\xi_k^{(j)}\}_{j=1}^{N}$ i.i.d. from $\mathcal{N}(\boldsymbol{0}, \boldsymbol{I}_n)$;

4   **for** $j = 1$ **to** N **do**

5 $\widehat{\boldsymbol{x}}_{t_{k+1}}^{(j)} \leftarrow \left(1 - (t_{k+1} - t_k)\frac{\dot{s}(t_k)}{s(t_k)}\right)\boldsymbol{x}_{t_k}^{(j)} + s(t_k)\sqrt{2\dot{\sigma}(t_k)\sigma(t_k)(t_{k+1} - t_k)}\xi_k^{(j)}$

        $+ 2(t_{k+1} - t_k)s(t_k)^2\dot{\sigma}(t_k)\sigma(t_k)\left(\boldsymbol{\phi}_\theta(\boldsymbol{x}_{t_k}^{(j)}, t_k) - \nabla_{\boldsymbol{x}}\mu_{\boldsymbol{y}}(\boldsymbol{x}_{t_k}^{(j)})\right)$;

     $\log \widehat{\beta}_{t_{k+1}}^{(j)} \leftarrow \log \beta_{t_{k+1}}^{(j)} + (t_{k+1} - t_k)\frac{\dot{s}(t_k)}{s(t_k)}\nabla_{\boldsymbol{x}}\mu_{\boldsymbol{y}}(\boldsymbol{x}_{t_k}^{(j)})^{\mathsf{T}}\boldsymbol{x}_{t_k}^{(j)}$

6 $- 2(t_{k+1} - t_k)s(t_k)^2\dot{\sigma}(t_k)\sigma(t_k)\nabla_{\boldsymbol{x}}\mu_{\boldsymbol{y}}(\boldsymbol{x}_{t_k}^{(j)})^{\mathsf{T}}\boldsymbol{\phi}_\theta(\boldsymbol{x}_{t_k}^{(j)}, t_k)$

        $+ (t_{k+1} - t_k)s(t_k)^2\dot{\sigma}(t_k)\sigma(t_k)\left(\|\nabla_{\boldsymbol{x}}\mu_{\boldsymbol{y}}(\boldsymbol{x}_{t_k}^{(j)})\|_2^2 - \Delta_{\boldsymbol{x}}\mu_{\boldsymbol{y}}(\boldsymbol{x}_{t_k}^{(j)})\right)$;

7   **end**

8 $\{(\boldsymbol{x}_{t_{k+1}}^{(j)}, \beta_{t_{k+1}}^{(j)})\}_{j=1}^{N} \leftarrow$ Algorithm 1$\left(c_{k+1}, \{(\widehat{\boldsymbol{x}}_{t_{k+1}}^{(j)}, \widehat{\beta}_{t_{k+1}}^{(j)})\}_{j=1}^{N}\right)$;

9 end

Algorithm 3: Corrector Step

Input: Initialization $\widehat{x}_0$, time t, iterations L, stepsize h, log-likelihood $\mu_{\boldsymbol{y}}(\cdot)$, score function $\boldsymbol{\phi}_\theta(\cdot)$.

Output: Sample $\widehat{x}_L \sim \widehat{q}_{\boldsymbol{y}}(\boldsymbol{x}, t) \propto \widehat{\overline{p}}_t(\boldsymbol{x})\exp(-\mu_{\boldsymbol{y}}(\boldsymbol{x}))$.

1 Draw $\{\xi_l\}_{l=1}^{L}$ i.i.d. from $\mathcal{N}(\boldsymbol{0}, \boldsymbol{I}_n)$;

2 for $l = 0$ **to** $L - 1$ **do**

3 $\widehat{\boldsymbol{x}}_{l+1} \leftarrow \widehat{\boldsymbol{x}}_l + h\left(\boldsymbol{\phi}_\theta(\widehat{\boldsymbol{x}}_l, t) - \nabla_{\boldsymbol{x}}\mu_{\boldsymbol{y}}(\widehat{\boldsymbol{x}}_l)\right) + \sqrt{2h}\xi_{l+1}$;

4 end

Algorithm 4: Approx.-Free Diffusion Posterior Sampler via ODE+Corrector (AFDPS-ODE)

Input: Noisy observation $\boldsymbol{y}$, log-likelihood $\mu_{\boldsymbol{y}}(\cdot)$, functions $s(t)$ and $\sigma(t)$, time grid $\{t_i\}_{i=0}^{K}$ with $t_0 = 0$ and $t_K = T$, thresholds $\{c_l\}_{l=1}^{K}$, score function $\boldsymbol{\phi}_\theta(\cdot, t)$, corrector iterations n_c, stepsize h_c, ensemble size N, initial weights $\beta_0^{(j)} = 1$ for $j \in [N]$.

Output: Posterior approximation $\sum_{j=1}^{N} \beta_T^{(j)} \delta_{\boldsymbol{x}_T^{(j)}} / \sum_{j=1}^{N} \beta_T^{(j)}$.

1 Draw $\{\boldsymbol{x}_0^{(i)}\}_{i=1}^{N}$ i.i.d. from $\widehat{q}_{\boldsymbol{y}}(\cdot, 0)$ via Stage I samplers in Section 3.1;

2 for $k = 0$ **to** $K - 1$ **do**

3   **for** $j = 1$ **to** N **do**

4 $\widetilde{\boldsymbol{x}}_{t_{k+1}}^{(j)} \leftarrow \left(1 - (t_{k+1} - t_k)\frac{\dot{s}(t_k)}{s(t_k)}\right)\boldsymbol{x}_{t_k}^{(j)} + (t_{k+1} - t_k)s(t_k)^2\dot{\sigma}(t_k)\sigma(t_k)\boldsymbol{\phi}_\theta(\boldsymbol{x}_{t_k}^{(j)}, t_k)$;

5 $\widehat{\boldsymbol{x}}_{t_{k+1}}^{(j)} \leftarrow$ Algorithm 3$\left(\widetilde{\boldsymbol{x}}_{t_{k+1}}^{(j)}, t_{k+1}, n_c, h_c, \mu_{\boldsymbol{y}}(\cdot), \boldsymbol{\phi}_\theta(\cdot, t)\right)$;

     $\log \widehat{\beta}_{t_{k+1}}^{(j)} \leftarrow \log \beta_{t_{k+1}}^{(j)} + (t_{k+1} - t_k)\frac{\dot{s}(t_k)}{s(t_k)}\nabla_{\boldsymbol{x}}\mu_{\boldsymbol{y}}\left(\boldsymbol{x}_{t_k}^{(j)}\right)^{\mathsf{T}}\boldsymbol{x}_{t_k}^{(j)}$

6 $- (t_{k+1} - t_k)s(t_k)^2\dot{\sigma}(t_k)\sigma(t_k)\nabla_{\boldsymbol{x}}\mu_{\boldsymbol{y}}\left(\boldsymbol{x}_{t_k}^{(j)}\right)^{\mathsf{T}}\boldsymbol{\phi}_\theta\left(\boldsymbol{x}_{t_k}^{(j)}, t_k\right)$;

7   **end**

8 $\{(\boldsymbol{x}_{t_{k+1}}^{(j)}, \beta_{t_{k+1}}^{(j)})\}_{j=1}^{N} \leftarrow$ Algorithm 1$\left(c_{k+1}, \{(\widehat{\boldsymbol{x}}_{t_{k+1}}^{(j)}, \widehat{\beta}_{t_{k+1}}^{(j)})\}_{j=1}^{N}\right)$;

9 end

Remark 3.1 (Connection with Feynman-Kac corrector (Skreta et al., 2025) and Guidance (Dhariwal & Nichol, 2021; Bradley & Nakkiran, 2024)). *A recent work (Skreta et al., 2025) proposed a related ensemble-based sampler within the SMC framework. However, the dynamics derived in our setting differ from those in Proposition D.5 of (Skreta et al., 2025), which is essentially the ODE case without correctors in our method. The key difference is the presence of a gradient term, $\nabla_{\boldsymbol{x}}\mu_{\boldsymbol{y}}$, in the dynamics of $\boldsymbol{x}_t$ (3.5), which is absent in their formulation. Such component, previously used in SGS + DM methods (Xu & Chi, 2024; Wu et al., 2024c) and in optimization-based denoising algorithms such as ADMM (Gabay & Mercier, 1976; Wang et al., 2008; Boyd et al., 2011; Sun et al., 2016; Chan et al., 2016; Ryu et al., 2019) and FISTA (Beck & Teboulle, 2009; Zhang & Ghanem, 2018; Xiang et al., 2021), is incorporated into our DM-based framework in a systematic way. The derivation illustrated in Figure 1 is shown to be essential for the method's empirical performance (cf. Section 5). A detailed comparison is given in Remark B.8 of Appendix B.*

In contrast to prior work on guided diffusion sampling (Dhariwal & Nichol, 2021; Bradley & Nakkiran, 2024; Wu et al., 2024a; Chidambaram et al., 2024) and its extensions (Ho & Salimans, 2022; Bansal et al., 2023; Song et al., 2023c; He et al., 2023; Guo et al., 2024; Lu & Wang, 2024; Zheng et al., 2024; Ye et al., 2024), which augment single-particle dynamics with a gradient term such as $\nabla_{\boldsymbol{x}}\log p_t(\boldsymbol{y}|\boldsymbol{x}_t)$ or $\nabla_{\boldsymbol{x}}\log p_t(\boldsymbol{x}_t|\boldsymbol{y})$, our PDE-based derivation naturally yields the gradient term $\nabla_{\boldsymbol{x}}\mu_{\boldsymbol{y}}$ within a principled framework. Additionally, our formulation introduces a linear term that must be simulated via an ensemble of weighted particles, rather than from a single trajectory. Such ensemble-based structure allows us to integrate gradient-based guidance and diffusion sampling under the SMC framework in a unified way, resulting in improved empirical performance.

4 Theoretical Analysis

In this section, we present our theoretical results of the ensemble-based posterior samplers introduced in Section 3. Our analysis is conducted in continuous time, based on the weighted particle dynamics (3.4) and (3.6). The impact of numerical discretization, as implemented in Algorithm 2 and Algorithm 4, is not considered here and is left for future work. Without loss of generality, we focus on the backward SDE setting (2.5), specifically using $s(t) = 1$ and $\sigma(t) = t$. We begin by introducing several technical assumptions.

Assumption 4.1 (Regularity of the log-likelihood). *The log-likelihood function $\mu_{\boldsymbol{y}}$ is twice differentiable and lower bounded by some constant $C_{\boldsymbol{y}}^{(1)}$ depending only on the observation $\boldsymbol{y}$.*

Assumption 4.2 (Bounded second moment). *The prior distribution p_0 satisfies a second-moment bound: $\mathbb{E}p_0\left[\|\boldsymbol{x}\|_2^2\right] \le m_2^2$.*

Assumption 4.3 (Score matching error). *The neural network estimator $\boldsymbol{\phi}_\theta(\boldsymbol{x}, t)$ approximates the score function $\nabla_{\boldsymbol{x}}\log \breve{p}_t(\boldsymbol{x})$ with uniformly bounded error across $t \in [0, T]$:*

$$\int_{\mathbb{R}^n} \|\boldsymbol{\phi}_\theta(\boldsymbol{x}, t) - \nabla_{\boldsymbol{x}}\log \breve{p}_t(\boldsymbol{x})\|_2^2 \, \breve{p}_t(\boldsymbol{x})\mathrm{d}\boldsymbol{x} \le \epsilon_{\boldsymbol{s}}^2. \tag{4.1}$$

Assumption 4.1 ensures the absence of singularities in the log-likelihood $\mu_{\boldsymbol{y}}$, which is a condition adopted in existing work on BIPs (Stuart, 2010) and satisfied by common noise models such as Gaussian and Poisson (with $C_{\boldsymbol{y}}^{(1)} = 0$). Assumptions 4.2 and 4.3 are aligned with recent theoretical frameworks for diffusion models (Wang et al., 2024; Chen et al., 2022; 2023a; Benton et al., 2023; Chen et al., 2024c). Particularly, Assumption 4.3 quantifies the approximation error due to neural network training and reflects the quality of the pre-trained score function. We now present our first main result, which quantifies the discrepancy between the true posterior $q_{\boldsymbol{y},0}$ and the distribution $\widehat{q}_{\boldsymbol{y},T}$ obtained by evolving our derived PDE dynamics (3.4) for time T.

Theorem 4.1 (Error Bound for Posterior Estimation). *Under Assumptions 4.1, 4.2, and 4.3, the total variation (TV) distance between the approximate and true posterior satisfies:*

$$\mathrm{TV}(\widehat{q}_{\boldsymbol{y},T}, q_{\boldsymbol{y},0}) \le C_{\boldsymbol{y}}^{(2)} \sqrt{\frac{m_2^2}{T^2} + T^2 \epsilon_{\boldsymbol{s}}^2}$$

where $q_{\boldsymbol{y},0}(\boldsymbol{x}) \propto p_0(\boldsymbol{x}) \exp(-\mu_{\boldsymbol{y}}(\boldsymbol{x}))$ is the exact posterior, and $\widehat{q}_{\boldsymbol{y},t}$ is the solution to the posterior evolution (3.4). The constant $C_{\boldsymbol{y}}^{(2)}$ depends only on the observation $\boldsymbol{y}$. Optimizing the right-hand side yields the asymptotic bound $\mathrm{TV}(\widehat{q}_{\boldsymbol{y},T}, q_{\boldsymbol{y},0}) \lesssim \sqrt{\epsilon_{\boldsymbol{s}}}$ when $T \asymp \sqrt{\epsilon_{\boldsymbol{s}}^{-1}}$.

A detailed proof of Theorem 4.1 can be found in Section C.1. It essentially combines techniques from the theory of diffusion models (Chen et al., 2023a; Wang et al., 2024) and the well-posedness theory of Bayesian inverse problems, which is closely related to (Purohit et al., 2024, Theorem 4.1). The result of Theorem 4.1 reveals a trade-off controlled by the time horizon T between the prior mismatch and score approximation error. Next, we study the particle approximation to the PDE solution (3.4). In particular, we examine the convergence of the dynamics of the weighted particle ensemble (3.6) in the many-particle limit.

Assumption 4.4 (Boundedness and Lipschitz continuity of I). *Define the function*

$$I(\boldsymbol{x}, t) := \|\nabla_{\boldsymbol{x}} \mu_{\boldsymbol{y}}(\boldsymbol{x})\|_2^2 - \Delta_{\boldsymbol{x}} \mu_{\boldsymbol{y}}(\boldsymbol{x}) - 2\phi_\theta(\boldsymbol{x}, t)^\intercal \nabla_{\boldsymbol{x}} \mu_{\boldsymbol{y}}(\boldsymbol{x}).$$

We assume that $I(\boldsymbol{x}, t)$ is uniformly bounded and Lipschitz continuous over $\mathbb{R}^n \times [0, T]$: $\max\{\|I\|_{L^\infty(\mathbb{R}^n \times [0,T])}, \mathrm{Lip}(I)\} \le B_{\boldsymbol{y}}$, for some constant $B_{\boldsymbol{y}}$ depending only on $\boldsymbol{y}$.

Assumption 4.4 ensures stability of the evolving particle weights, preventing degeneracy or explosion over time. In practice, this condition is enforced via the resampling step in Algorithm 1. While we adopt this assumption for analytical tractability, relaxing it and developing a rigorous theory of the resampling step remain important future directions, which might link to existing theoretical studies (Lu et al., 2023; Chen et al., 2023b; Yan et al., 2024) on sampling algorithms that use birth-death dynamics or Fisher–Rao gradient flow.

Theorem 4.2 (Convergence in the Many-Particle Limit). *Under Assumptions 4.1–4.4, the empirical distribution of the particle system converges to the solution of the posterior PDE. Specifically, for all $t \in [0, T]$,*

$$\lim_{N \to \infty} \mathbb{E}[\mathcal{W}_2^2(\gamma_t^N, \gamma_t)] = 0,$$

where γ_t is the law of a single weighted particle pair $(\boldsymbol{x}_t, \beta_t)$ governed by (3.5), such that the marginal $\widehat{q}_{\boldsymbol{y}}(\cdot, t)$ is recovered via $P_\beta \gamma_t(\cdot) = \int_{\mathbb{R}} \beta \gamma_t(\cdot, \beta) \mathrm{d}\beta = \widehat{q}_{\boldsymbol{y}}(\cdot, t)$, and γ_t^N is the empirical measure of the N-particle system $\left\{\left(\boldsymbol{x}_t^{(i)}, \beta_t^{(i)}\right)\right\}_{i=1}^N$ governed by (3.6).

Theorem 4.2 establishes the mean-field consistency of the weighted ensemble approximation in the 2-Wasserstein sense. Its proof, which is presented in Appendix C.2, is based on results from propagation of chaos (Sznitman, 1991; Lacker, 2018). Together with Theorem 4.1, our theoretical results provide both rigorous guarantee for the accuracy of the continuum posterior approximation and justification of the proposed ensemble-based implementation.

5 Experiments

In this section, we evaluate the empirical performance of our method on several BIPs in imaging. Additional implementation details and experimental results can be found in Appendix D and E, respectively.

Problem Setting. We consider four canonical inverse problems: Gaussian Deblurring (GD), Motion Deblurring (MD), Super Resolution (SR), and Box Inpaint (BI). In all these tasks, we assume that the observational noise is isotropic Gaussian with variance 0.2, *i.e.*, $\boldsymbol{n} \sim \mathcal{N}(\boldsymbol{0}, 0.2\boldsymbol{I}_m)$ in (2.1), a more challenging setting compared to the commonly used low-noise scenario with variance 2.5×10^{-3} (Dou & Song, 2024; Wu

et al., 2024c). Experiments are conducted on FFHQ-256 (Karras et al., 2019) and ImageNet-256 (Deng et al., 2009), two widely used datasets in imaging and vision.

Baselines. We compare our proposed algorithms with several state-of-the-art diffusion model-based posterior sampling methods:

- *DPS (Chung et al., 2022)*: a sampler that guides the pretrained DM with approximations of manifold-constrained gradients derived from the measurement likelihood.
- *DCDP (Li et al., 2024b)*: a framework alternating between optimization steps that ensure data consistency and pretrained DMs for posterior sampling.
- *SGS-EDM (Wu et al., 2024c)*: a split Gibbs sampler coupled with a DM for efficient posterior inference.
- *FK-Corrector (Skreta et al., 2025)*: an SMC-based sampler using Feynman-Kac formula to correct trajectories.
- *PF-SMC-DM (Dou & Song, 2024)*: a particle filtering framework combining SMC with diffusion models.

Experimental Settings. To ensure a fair comparison, we use the same checkpoints for the two pre-trained score functions provided in (Chung et al., 2022) and fix the number of function evaluations (NFE) to 2×10^4 across all methods. For ensemble-based approaches, the number of particles is set to $N = 10$. In the case of AFDPS-ODE (Algorithm 4), we reduce the number of particles to $N = 5$ to offset the additional computational cost from the corrector step, while maintaining the total NFE consistent with AFDPS-SDE (Algorithm 2). We evaluate reconstruction quality using two metrics: PSNR (Peak Signal-to-Noise Ratio), which quantifies pixel-level accuracy, and LPIPS (Learned Perceptual Image Patch Similarity) (Zhang et al., 2018b), which measures perceptual similarity; both metrics are computed between the reconstructed sample mean and the ground truth image over a set of 100 randomly selected validation images.

Figure 2: Visualization of posterior samples by AFDPS. **Upper:** Original; **Middle:** Blurred; **Lower:** Reconstructed.

Table 1: Results on 4 inverse problems for 100 validation images from FFHQ-256.

Method	Gaussian Deblurring		Motion Deblurring		Super Resolution		Box Inpainting	
	PSNR (↑)	LPIPS (↓)	PSNR (↑)	LPIPS (↓)	PSNR (↑)	LPIPS (↓)	PSNR (↑)	LPIPS (↓)
DPS (Chung et al., 2022)	22.57	0.2976	21.00	0.3280	19.09	0.5627	21.57	0.3245
DCDP (Li et al., 2024b)	24.77	0.2868	21.57	0.3487	21.23	0.5139	22.05	0.4525
SGS-EDM (Wu et al., 2024c)	24.78	0.2776	23.45	0.3009	22.41	0.3225	23.69	0.2301
FK-Corrector (Skreta et al., 2025)	21.22	0.4023	20.51	0.4275	20.67	0.4133	16.97	0.5490
PF-SMC-DM (Dou & Song, 2024)	23.00	0.3940	**26.59**	0.3435	18.92	0.5049	25.54	0.3391
AFDPS-SDE (Alg. 2)	24.83	0.2580	23.58	**0.2869**	**22.96**	**0.3063**	25.45	0.2084
AFDPS-ODE (Alg. 4)	**24.98**	**0.2560**	23.52	0.2905	21.47	0.3345	**25.73**	**0.1969**

Table 2: Results on 4 inverse problems for 100 validation images from ImageNet-256.

Method	Gaussian Deblurring		Motion Deblurring		Super Resolution		Box Inpainting	
	PSNR (↑)	LPIPS (↓)	PSNR (↑)	LPIPS (↓)	PSNR (↑)	LPIPS (↓)	PSNR (↑)	LPIPS (↓)
DPS (Chung et al., 2022)	20.60	0.4351	20.46	0.5328	19.17	0.4940	22.70	0.3765
DCDP (Li et al., 2024b)	22.34	0.4821	20.59	0.5338	20.26	0.5597	21.67	0.4344
SGS-EDM (Wu et al., 2024c)	19.31	0.4807	20.54	0.4653	19.61	0.4986	21.42	0.4643
FK-Corrector (Skreta et al., 2025)	18.39	0.5973	18.34	0.6022	18.57	0.5887	16.28	0.7132
PF-SMC-DM (Dou & Song, 2024)	20.06	0.5927	**23.91**	**0.4195**	18.42	0.6462	21.34	0.4195
AFDPS-SDE (Alg. 2)	22.38	**0.3925**	19.46	0.4936	**20.97**	**0.4643**	**23.15**	0.3051
AFDPS-ODE (Alg. 4)	**22.42**	0.4633	21.54	0.4944	19.60	0.5634	22.76	**0.2716**

Results. The quantitative performance of our proposed methods - AFDPS-SDE (Algorithm 2) and AFDPS-ODE (Algorithm 4) - is presented in Table 1 for the FFHQ-256 dataset and Table 2 for the ImageNet-256

dataset. On FFHQ-256, both methods consistently demonstrate strong or highly competitive results across all evaluated inverse problems, frequently outperforming existing baselines in terms of both PSNR and LPIPS. The two variants show complementary strengths across different tasks, underscoring the benefit of incorporating both formulations. Similar trends are observed on the more diverse ImageNet-256 dataset, where both AFDPS methods continue to achieve robust and often superior performance. Qualitative examples are provided in Figure 2 and more in Appendix E, illustrating the visual quality of reconstructions across tasks with comparisons to baselines.

6 Discussion and Conclusion

In this paper, we introduced a new method for solving Bayesian inverse problems using diffusion models as the prior. Our method derives a novel PDE that exactly characterizes the exact posterior dynamics under an evolving diffusion prior, avoiding the heuristic approximations employed by previous methods and leading to better SMC-type algorithms in practice. Theoretically, we provide the error bounds of the posterior sampling algorithm in terms of the score function error, and justify the convergence of the ensemble method in the many-particle limit. Empirically, our method outperforms state-of-the-art diffusion-based solvers across a range of computational imaging tasks.

This work opens several promising directions for future research. Our method applies to other inverse problems arising in various fields with twice-differentiable log-likelihoods, including optics, medical imaging, video analytics, geoscience, astronomy, fluid dynamics, chemistry and biology (Sun et al., 2024; Wu et al., 2024c; Zheng et al., 2025; Jaganathan et al., 2016; Fienup, 1982; Candes et al., 2015b;a; Kantas et al., 2014; Daras et al., 2024b; Zhang et al., 2025a; Jing et al., 2024; Maddipatla et al., 2025; Sridharan et al., 2022; Hu et al., 2024). Methodologically, our framework could be extended to settings such as multi-marginal sampling (Albergo et al., 2023a; Lindsey, 2025), conditional sampling (Zhu et al., 2023), reward-guided sampling (Uehara et al., 2025), and other variants of DMs, such as latent diffusion models (LDMs) (Rombach et al., 2022; Song et al., 2023a), discrete diffusion models (Murata et al., 2024; Luan et al., 2025; Chu et al., 2025; Austin et al., 2021; Hoogeboom et al., 2021a;b; Meng et al., 2022; Sun et al., 2022; Richemond et al., 2022; Lou et al., 2023; Floto et al., 2023; Santos et al., 2023; Chen & Ying, 2024b; Ren et al., 2024a), flow matching (Zhang et al., 2024c), or to the general framework of denoising Markov model with variants like generator matching (Benton et al., 2024; Holderrieth et al., 2024; Ren et al., 2025b). Theoretically, further work could explore numerical analysis of our method (Chen et al., 2022; 2023a; 2024c) or incorporate it with faster inference methods like parallel sampling (Shih et al., 2024; Tang et al., 2024; Cao et al., 2024; Selvam et al., 2024; Chen et al., 2024a; Gupta et al., 2024), high-order solvers (Karras et al., 2022; Lu et al., 2022b; Liu et al., 2022a; Lu et al., 2022a; Zheng et al., 2023; Li et al., 2024a; Wu et al., 2024b; Ren et al., 2025a) and their variants.

References

Idan Achituve, Hai Victor Habi, Amir Rosenfeld, Arnon Netzer, Idit Diamant, and Ethan Fetaya. Inverse problem sampling in latent space using sequential monte carlo. *arXiv preprint arXiv:2502.05908*, 2025.

Amira Alakhdar, Barnabas Poczos, and Newell Washburn. Diffusion models in de novo drug design. *Journal of Chemical Information and Modeling*, 2024.

Sarah Alamdari, Nitya Thakkar, Rianne van den Berg, Alex X Lu, Nicolo Fusi, Ava P Amini, and Kevin K Yang. Protein generation with evolutionary diffusion: sequence is all you need. *BioRxiv*, pp. 2023–09, 2023.

Michael S Albergo and Eric Vanden-Eijnden. Building normalizing flows with stochastic interpolants. *arXiv preprint arXiv:2209.15571*, 2022.

Michael S Albergo and Eric Vanden-Eijnden. Nets: A non-equilibrium transport sampler. *arXiv preprint arXiv:2410.02711*, 2024.

Michael S Albergo, Nicholas M Boffi, Michael Lindsey, and Eric Vanden-Eijnden. Multimarginal generative modeling with stochastic interpolants. *arXiv preprint arXiv:2310.03695*, 2023a.

Michael S Albergo, Nicholas M Boffi, and Eric Vanden-Eijnden. Stochastic interpolants: A unifying framework for flows and diffusions. *arXiv preprint arXiv:2303.08797*, 2023b.

Brian DO Anderson. Reverse-time diffusion equation models. *Stochastic Processes and their Applications*, 12 (3):313–326, 1982.

Abdul Fatir Ansari, Ming Liang Ang, and Harold Soh. Refining deep generative models via discriminator gradient flow. *arXiv preprint arXiv:2012.00780*, 2020.

Simon Arridge, Peter Maass, Ozan Öktem, and Carola-Bibiane Schönlieb. Solving inverse problems using data-driven models. *Acta Numerica*, 28:1–174, 2019.

Muhammad Asim, Max Daniels, Oscar Leong, Ali Ahmed, and Paul Hand. Invertible generative models for inverse problems: mitigating representation error and dataset bias. In *International conference on machine learning*, pp. 399–409. PMLR, 2020.

Jacob Austin, Daniel D Johnson, Jonathan Ho, Daniel Tarlow, and Rianne Van Den Berg. Structured denoising diffusion models in discrete state-spaces. *Advances in Neural Information Processing Systems*, 34:17981–17993, 2021.

Arpit Bansal, Hong-Min Chu, Avi Schwarzschild, Soumyadip Sengupta, Micah Goldblum, Jonas Geiping, and Tom Goldstein. Universal guidance for diffusion models. In *Proceedings of the IEEE/CVF Conference on Computer Vision and Pattern Recognition*, pp. 843–852, 2023.

Federico Becca and Sandro Sorella. *Quantum Monte Carlo approaches for correlated systems*. Cambridge University Press, 2017.

Amir Beck and Marc Teboulle. A fast iterative shrinkage-thresholding algorithm for linear inverse problems. *SIAM journal on imaging sciences*, 2(1):183–202, 2009.

Joe Benton, Valentin De Bortoli, Arnaud Doucet, and George Deligiannidis. Linear convergence bounds for diffusion models via stochastic localization. *arXiv preprint arXiv:2308.03686*, 2023.

Joe Benton, Yuyang Shi, Valentin De Bortoli, George Deligiannidis, and Arnaud Doucet. From denoising diffusions to denoising markov models. *Journal of the Royal Statistical Society Series B: Statistical Methodology*, 86(2):286–301, 2024.

Mario Bertero, Patrizia Boccacci, and Christine De Mol. *Introduction to inverse problems in imaging*. CRC press, 2021.

Alexandros Beskos, Dan Crisan, and Ajay Jasra. On the stability of sequential monte carlo methods in high dimensions. *The Annals of Applied Probability*, 24(4):1396–1445, 2014a.

Alexandros Beskos, Dan O Crisan, Ajay Jasra, and Nick Whiteley. Error bounds and normalising constants for sequential monte carlo samplers in high dimensions. *Advances in Applied Probability*, 46(1):279–306, 2014b.

Alexandros Beskos, Ajay Jasra, Nikolas Kantas, and Alexandre Thiery. On the convergence of adaptive sequential monte carlo methods. *The Annals of Applied Probability*, 26(2):1111–1146, 2016.

Nicholas M Boffi, Michael S Albergo, and Eric Vanden-Eijnden. Flow map matching. *arXiv preprint arXiv:2406.07507*, 2024.

Ashish Bora, Ajil Jalal, Eric Price, and Alexandros G Dimakis. Compressed sensing using generative models. In *International conference on machine learning*, pp. 537–546. PMLR, 2017.

Giacomo Borghi and Lorenzo Pareschi. Wasserstein convergence rates for stochastic particle approximation of boltzmann models. *arXiv preprint arXiv:2504.10091*, 2025.

Mireille Bossy and Denis Talay. A stochastic particle method for the mckean-vlasov and the burgers equation. *Mathematics of computation*, 66(217):157–192, 1997.

Stephen Boyd, Neal Parikh, Eric Chu, Borja Peleato, Jonathan Eckstein, et al. Distributed optimization and statistical learning via the alternating direction method of multipliers. *Foundations and Trends® in Machine learning*, 3(1):1–122, 2011.

Benjamin Boys, Mark Girolami, Jakiw Pidstrigach, Sebastian Reich, Alan Mosca, and O Deniz Akyildiz. Tweedie moment projected diffusions for inverse problems. *arXiv preprint arXiv:2310.06721*, 2023.

Arwen Bradley and Preetum Nakkiran. Classifier-free guidance is a predictor-corrector. *arXiv preprint arXiv:2408.09000*, 2024.

Joan Bruna and Jiequn Han. Provable posterior sampling with denoising oracles via tilted transport. *Advances in Neural Information Processing Systems*, 37:82863–82894, 2024.

Michel Caffarel and Pierre Claverie. Development of a pure diffusion quantum monte carlo method using a full generalized feynman–kac formula. i. formalism. *The Journal of chemical physics*, 88(2):1088–1099, 1988a.

Michel Caffarel and Pierre Claverie. Development of a pure diffusion quantum monte carlo method using a full generalized feynman–kac formula. ii. applications to simple systems. *The Journal of chemical physics*, 88(2):1100–1109, 1988b.

Emmanuel J Candes, Xiaodong Li, and Mahdi Soltanolkotabi. Phase retrieval from coded diffraction patterns. *Applied and Computational Harmonic Analysis*, 39(2):277–299, 2015a.

Emmanuel J Candes, Xiaodong Li, and Mahdi Soltanolkotabi. Phase retrieval via wirtinger flow: Theory and algorithms. *IEEE Transactions on Information Theory*, 61(4):1985–2007, 2015b.

Jiezhang Cao, Yue Shi, Kai Zhang, Yulun Zhang, Radu Timofte, and Luc Van Gool. Deep equilibrium diffusion restoration with parallel sampling. In *Proceedings of the IEEE/CVF Conference on Computer Vision and Pattern Recognition*, pp. 2824–2834, 2024.

Xiang Cao and Xiaoqun Zhang. Subspace diffusion posterior sampling for travel-time tomography. *Inverse Problems*, 2024.

Gabriel Cardoso, Sylvain Le Corff, Eric Moulines, et al. Monte carlo guided denoising diffusion models for bayesian linear inverse problems. In *The Twelfth International Conference on Learning Representations*, 2023.

José A Carrillo and Urbain Vaes. Wasserstein stability estimates for covariance-preconditioned fokker–planck equations. *Nonlinearity*, 34(4):2275, 2021.

Stanley Chan et al. Tutorial on diffusion models for imaging and vision. *Foundations and Trends® in Computer Graphics and Vision*, 16(4):322–471, 2024.

Stanley H Chan, Xiran Wang, and Omar A Elgendy. Plug-and-play admm for image restoration: Fixed-point convergence and applications. *IEEE Transactions on Computational Imaging*, 3(1):84–98, 2016.

Haoxuan Chen and Lexing Ying. Ensemble-based annealed importance sampling. *arXiv preprint arXiv:2401.15645*, 2024a.

Haoxuan Chen, Yinuo Ren, Lexing Ying, and Grant Rotskoff. Accelerating diffusion models with parallel sampling: Inference at sub-linear time complexity. *Advances in Neural Information Processing Systems*, 37: 133661–133709, 2024a.

Hongrui Chen and Lexing Ying. Convergence analysis of discrete diffusion model: Exact implementation through uniformization. *arXiv preprint arXiv:2402.08095*, 2024b.

Hongrui Chen, Holden Lee, and Jianfeng Lu. Improved analysis of score-based generative modeling: User-friendly bounds under minimal smoothness assumptions. In *International Conference on Machine Learning*, pp. 4735–4763. PMLR, 2023a.

Junhua Chen, Lorenz Richter, Julius Berner, Denis Blessing, Gerhard Neumann, and Anima Anandkumar. Sequential controlled langevin diffusions. *arXiv preprint arXiv:2412.07081*, 2024b.

Sitan Chen, Sinho Chewi, Jerry Li, Yuanzhi Li, Adil Salim, and Anru R Zhang. Sampling is as easy as learning the score: theory for diffusion models with minimal data assumptions. *arXiv preprint arXiv:2209.11215*, 2022.

Sitan Chen, Sinho Chewi, Holden Lee, Yuanzhi Li, Jianfeng Lu, and Adil Salim. The probability flow ode is provably fast. *Advances in Neural Information Processing Systems*, 36, 2024c.

Yifan Chen, Daniel Zhengyu Huang, Jiaoyang Huang, Sebastian Reich, and Andrew M Stuart. Sampling via gradient flows in the space of probability measures. *arXiv preprint arXiv:2310.03597*, 2023b.

Yifan Chen, Mark Goldstein, Mengjian Hua, Michael S Albergo, Nicholas M Boffi, and Eric Vanden-Eijnden. Probabilistic forecasting with stochastic interpolants and f\" ollmer processes. *arXiv preprint arXiv:2403.13724*, 2024d.

Yifan Chen, Daniel Zhengyu Huang, Jiaoyang Huang, Sebastian Reich, and Andrew M Stuart. Efficient, multimodal, and derivative-free bayesian inference with fisher–rao gradient flows. *Inverse Problems*, 40(12): 125001, 2024e.

Zhuo Chen, Jacob McCarran, Esteban Vizcaino, Marin Soljacic, and Di Luo. Teng: Time-evolving natural gradient for solving pdes with deep neural nets toward machine precision. In *Forty-first International Conference on Machine Learning*, 2024f.

Xiuyuan Cheng, Jianfeng Lu, Yixin Tan, and Yao Xie. Convergence of flow-based generative models via proximal gradient descent in wasserstein space. *IEEE Transactions on Information Theory*, 2024a.

Ziheng Cheng, Shiyue Zhang, Longlin Yu, and Cheng Zhang. Particle-based variational inference with generalized wasserstein gradient flow. *Advances in Neural Information Processing Systems*, 36, 2024b.

Alina Chertock. A practical guide to deterministic particle methods. In *Handbook of numerical analysis*, volume 18, pp. 177–202. Elsevier, 2017.

Muthu Chidambaram, Khashayar Gatmiry, Sitan Chen, Holden Lee, and Jianfeng Lu. What does guidance do? a fine-grained analysis in a simple setting. *arXiv preprint arXiv:2409.13074*, 2024.

Lenaic Chizat, Gabriel Peyré, Bernhard Schmitzer, and François-Xavier Vialard. An interpolating distance between optimal transport and fisher–rao metrics. *Foundations of Computational Mathematics*, 18:1–44, 2018.

Jaemoo Choi, Jaewoong Choi, and Myungjoo Kang. Scalable wasserstein gradient flow for generative modeling through unbalanced optimal transport. *arXiv preprint arXiv:2402.05443*, 2024.

Jooyoung Choi, Sungwon Kim, Yonghyun Jeong, Youngjune Gwon, and Sungroh Yoon. Ilvr: Conditioning method for denoising diffusion probabilistic models. *arXiv preprint arXiv:2108.02938*, 2021.

Wonshik Choi, Christopher Fang-Yen, Kamran Badizadegan, Seungeun Oh, Niyom Lue, Ramachandra R Dasari, and Michael S Feld. Tomographic phase microscopy. *Nature methods*, 4(9):717–719, 2007.

Nicolas Chopin. A sequential particle filter method for static models. *Biometrika*, 89(3):539–552, 2002.

Wenda Chu, Yang Song, and Yisong Yue. Split gibbs discrete diffusion posterior sampling. *arXiv preprint arXiv:2503.01161*, 2025.

Hyungjin Chung and Jong Chul Ye. Score-based diffusion models for accelerated mri. *Medical image analysis*, 80:102479, 2022.

Hyungjin Chung, Jeongsol Kim, Michael T Mccann, Marc L Klasky, and Jong Chul Ye. Diffusion posterior sampling for general noisy inverse problems. *arXiv preprint arXiv:2209.14687*, 2022.

Florentin Coeurdoux, Nicolas Dobigeon, and Pierre Chainais. Plug-and-play split gibbs sampler: embedding deep generative priors in bayesian inference. *IEEE Transactions on Image Processing*, 2024.

Jordan Cotler and Semon Rezchikov. Renormalizing diffusion models. *arXiv preprint arXiv:2308.12355*, 2023.

Simon L Cotter, Massoumeh Dashti, James Cooper Robinson, and Andrew M Stuart. Bayesian inverse problems for functions and applications to fluid mechanics. *Inverse problems*, 25(11):115008, 2009.

Tiangang Cui, Kody JH Law, and Youssef M Marzouk. Dimension-independent likelihood-informed mcmc. *Journal of Computational Physics*, 304:109–137, 2016.

Giannis Daras, Hyungjin Chung, Chieh-Hsin Lai, Yuki Mitsufuji, Jong Chul Ye, Peyman Milanfar, Alexandros G Dimakis, and Mauricio Delbracio. A survey on diffusion models for inverse problems. *arXiv preprint arXiv:2410.00083*, 2024a.

Giannis Daras, Weili Nie, Karsten Kreis, Alex Dimakis, Morteza Mardani, Nikola Kovachki, and Arash Vahdat. Warped diffusion: Solving video inverse problems with image diffusion models. *Advances in Neural Information Processing Systems*, 37:101116–101143, 2024b.

Agnimitra Dasgupta, Alexsander Marciano da Cunha, Ali Fardisi, Mehrnegar Aminy, Brianna Binder, Bryan Shaddy, and Assad A Oberai. Unifying and extending diffusion models through pdes for solving inverse problems. *arXiv preprint arXiv:2504.07437*, 2025.

Pierre Degond and Sylvie Mas-Gallic. The weighted particle method for convection-diffusion equations. i. the case of an isotropic viscosity. *Mathematics of computation*, 53(188):485–507, 1989.

Pierre Degond and Francisco-José Mustieles. A deterministic approximation of diffusion equations using particles. *SIAM Journal on Scientific and Statistical Computing*, 11(2):293–310, 1990.

Pierre Del Moral. Mean field simulation for monte carlo integration. *Monographs on Statistics and Applied Probability*, 126(26):6, 2013.

Pierre Del Moral, Arnaud Doucet, and Ajay Jasra. Sequential monte carlo samplers. *Journal of the Royal Statistical Society Series B: Statistical Methodology*, 68(3):411–436, 2006.

Jia Deng, Wei Dong, Richard Socher, Li-Jia Li, Kai Li, and Li Fei-Fei. Imagenet: A large-scale hierarchical image database. In *2009 IEEE conference on computer vision and pattern recognition*, pp. 248–255. Ieee, 2009.

Prafulla Dhariwal and Alexander Nichol. Diffusion models beat gans on image synthesis. *Advances in neural information processing systems*, 34:8780–8794, 2021.

Michael Ziyang Diao, Krishna Balasubramanian, Sinho Chewi, and Adil Salim. Forward-backward gaussian variational inference via jko in the bures-wasserstein space. In *International Conference on Machine Learning*, pp. 7960–7991. PMLR, 2023.

Zhao Ding, Chenguang Duan, Yuling Jiao, Jerry Zhijian Yang, Cheng Yuan, and Pingwen Zhang. Nonlinear assimilation with score-based sequential langevin sampling. *arXiv preprint arXiv:2411.13443*, 2024.

Zhiyan Ding and Qin Li. Ensemble kalman inversion: mean-field limit and convergence analysis. *Statistics and Computing*, 31:1–21, 2021a.

Zhiyan Ding and Qin Li. Ensemble kalman sampler: Mean-field limit and convergence analysis. *SIAM Journal on Mathematical Analysis*, 53(2):1546–1578, 2021b.

Carles Domingo-Enrich, Samy Jelassi, Arthur Mensch, Grant Rotskoff, and Joan Bruna. A mean-field analysis of two-player zero-sum games. *Advances in neural information processing systems*, 33:20215–20226, 2020.

Zehao Dou and Yang Song. Diffusion posterior sampling for linear inverse problem solving: A filtering perspective. In *The Twelfth International Conference on Learning Representations*, 2024.

Arnaud Doucet, Adam M Johansen, et al. A tutorial on particle filtering and smoothing: Fifteen years later. *Handbook of nonlinear filtering*, 12(656-704):3, 2009.

Andreas Eberle and Carlo Marinelli. Convergence of sequential markov chain monte carlo methods: I. nonlinear flow of probability measures. *arXiv preprint math/0612074*, 2006.

Andreas Eberle and Carlo Marinelli. Quantitative approximations of evolving probability measures and sequential markov chain monte carlo methods. *Probability Theory and Related Fields*, 155:665–701, 2013.

Jiaojiao Fan, Qinsheng Zhang, Amirhossein Taghvaei, and Yongxin Chen. Variational wasserstein gradient flow. *arXiv preprint arXiv:2112.02424*, 2021.

Yuwei Fan and Lexing Ying. Solving inverse wave scattering with deep learning. *arXiv preprint arXiv:1911.13202*, 2019a.

Yuwei Fan and Lexing Ying. Solving optical tomography with deep learning. *arXiv preprint arXiv:1910.04756*, 2019b.

Yuwei Fan and Lexing Ying. Solving electrical impedance tomography with deep learning. *Journal of Computational Physics*, 404:109119, 2020.

Yuwei Fan and Lexing Ying. Solving traveltime tomography with deep learning. *Communications in Mathematics and Statistics*, 11(1):3–19, 2023.

James R Fienup. Phase retrieval algorithms: a comparison. *Applied optics*, 21(15):2758–2769, 1982.

Griffin Floto, Thorsteinn Jonsson, Mihai Nica, Scott Sanner, and Eric Zhengyu Zhu. Diffusion on the probability simplex. *arXiv preprint arXiv:2309.02530*, 2023.

Romain Fournier, Lei Wang, Oleg V Yazyev, and QuanSheng Wu. Artificial neural network approach to the analytic continuation problem. *Physical Review Letters*, 124(5):056401, 2020.

Daniel Gabay and Bertrand Mercier. A dual algorithm for the solution of nonlinear variational problems via finite element approximation. *Computers & mathematics with applications*, 2(1):17–40, 1976.

Marylou Gabrié, Grant M Rotskoff, and Eric Vanden-Eijnden. Adaptive monte carlo augmented with normalizing flows. *Proceedings of the National Academy of Sciences*, 119(10):e2109420119, 2022.

Yuan Gao, Yuling Jiao, Yang Wang, Yao Wang, Can Yang, and Shunkang Zhang. Deep generative learning via variational gradient flow. In *International Conference on Machine Learning*, pp. 2093–2101. PMLR, 2019.

Davis Gilton, Greg Ongie, and Rebecca Willett. Neumann networks for linear inverse problems in imaging. *IEEE Transactions on Computational Imaging*, 6:328–343, 2019.

François Giraud and Pierre Del Moral. Nonasymptotic analysis of adaptive and annealed feynman–kac particle models. *Bernoulli*, 23(1):670–709, 2017.

Jonathan Goodman, Thomas Y Hou, and John Lowengrub. Convergence of the point vortex method for the 2-d euler equations. *Communications on Pure and Applied Mathematics*, 43(3):415–430, 1990.

James Gubernatis, Naoki Kawashima, and Philipp Werner. *Quantum Monte Carlo Methods*. Cambridge University Press, 2016.

Yingqing Guo, Hui Yuan, Yukang Yang, Minshuo Chen, and Mengdi Wang. Gradient guidance for diffusion models: An optimization perspective. *arXiv preprint arXiv:2404.14743*, 2024.

Shivam Gupta, Linda Cai, and Sitan Chen. Faster diffusion-based sampling with randomized midpoints: Sequential and parallel. *arXiv preprint arXiv:2406.00924*, 2024.

Diaa E Habibi, Gert Aarts, Lingxiao Wang, and Kai Zhou. Diffusion models learn distributions generated by complex langevin dynamics. *arXiv preprint arXiv:2412.01919*, 2024.

Paul Hagemann, Johannes Hertrich, and Gabriele Steidl. Stochastic normalizing flows for inverse problems: A markov chains viewpoint. *SIAM/ASA Journal on Uncertainty Quantification*, 10(3):1162–1190, 2022.

Jiequn Han, Jianfeng Lu, and Mo Zhou. Solving high-dimensional eigenvalue problems using deep neural networks: A diffusion monte carlo like approach. *Journal of Computational Physics*, 423:109792, 2020.

Yutong He, Naoki Murata, Chieh-Hsin Lai, Yuhta Takida, Toshimitsu Uesaka, Dongjun Kim, Wei-Hsiang Liao, Yuki Mitsufuji, J Zico Kolter, Ruslan Salakhutdinov, et al. Manifold preserving guided diffusion. *arXiv preprint arXiv:2311.16424*, 2023.

Jonathan Ho and Tim Salimans. Classifier-free diffusion guidance. *arXiv preprint arXiv:2207.12598*, 2022.

Jonathan Ho, Ajay Jain, and Pieter Abbeel. Denoising diffusion probabilistic models. *Advances in neural information processing systems*, 33:6840–6851, 2020.

Peter Holderrieth, Marton Havasi, Jason Yim, Neta Shaul, Itai Gat, Tommi Jaakkola, Brian Karrer, Ricky TQ Chen, and Yaron Lipman. Generator matching: Generative modeling with arbitrary markov processes. *arXiv preprint arXiv:2410.20587*, 2024.

Peter Holderrieth, Michael S Albergo, and Tommi Jaakkola. Leaps: A discrete neural sampler via locally equivariant networks. *arXiv preprint arXiv:2502.10843*, 2025.

Emiel Hoogeboom, Alexey A Gritsenko, Jasmijn Bastings, Ben Poole, Rianne van den Berg, and Tim Salimans. Autoregressive diffusion models. *arXiv preprint arXiv:2110.02037*, 2021a.

Emiel Hoogeboom, Didrik Nielsen, Priyank Jaini, Patrick Forré, and Max Welling. Argmax flows and multinomial diffusion: Learning categorical distributions. *Advances in Neural Information Processing Systems*, 34:12454–12465, 2021b.

Thomas Y Hou, Ka Chun Lam, Pengchuan Zhang, and Shumao Zhang. Solving bayesian inverse problems from the perspective of deep generative networks. *Computational Mechanics*, 64:395–408, 2019.

Chloe Hsu, Robert Verkuil, Jason Liu, Zeming Lin, Brian Hie, Tom Sercu, Adam Lerer, and Alexander Rives. Learning inverse folding from millions of predicted structures. In *International conference on machine learning*, pp. 8946–8970. PMLR, 2022.

Frank Hu, Michael S Chen, Grant M Rotskoff, Matthew W Kanan, and Thomas E Markland. Accurate and efficient structure elucidation from routine one-dimensional nmr spectra using multitask machine learning. *ACS Central Science*, 10(11):2162–2170, 2024.

Kaitong Hu, Zhenjie Ren, David Šiška, and Łukasz Szpruch. Mean-field langevin dynamics and energy landscape of neural networks. In *Annales de l'Institut Henri Poincare (B) Probabilites et statistiques*, volume 57, pp. 2043–2065. Institut Henri Poincaré, 2021.

Aapo Hyvärinen and Peter Dayan. Estimation of non-normalized statistical models by score matching. *Journal of Machine Learning Research*, 6(4), 2005.

Kishore Jaganathan, Yonina C Eldar, and Babak Hassibi. Phase retrieval: An overview of recent developments. *Optical Compressive Imaging*, pp. 279–312, 2016.

Enze Jiang, Jishen Peng, Zheng Ma, and Xiong-Bin Yan. Ode-dps: Ode-based diffusion posterior sampling for linear inverse problems in partial differential equation. *Journal of Scientific Computing*, 102(3):69, 2025.

Bowen Jing, Bonnie Berger, and Tommi Jaakkola. Alphafold meets flow matching for generating protein ensembles. *arXiv preprint arXiv:2402.04845*, 2024.

Richard Jordan, David Kinderlehrer, and Felix Otto. The variational formulation of the fokker–planck equation. *SIAM journal on mathematical analysis*, 29(1):1–17, 1998.

Nikolas Kantas, Alexandros Beskos, and Ajay Jasra. Sequential monte carlo methods for high-dimensional inverse problems: A case study for the navier–stokes equations. *SIAM/ASA Journal on Uncertainty Quantification*, 2(1):464–489, 2014.

Tero Karras, Samuli Laine, and Timo Aila. A style-based generator architecture for generative adversarial networks. In *Proceedings of the IEEE/CVF conference on computer vision and pattern recognition*, pp. 4401–4410, 2019.

Tero Karras, Miika Aittala, Timo Aila, and Samuli Laine. Elucidating the design space of diffusion-based generative models. *Advances in Neural Information Processing Systems*, 35:26565–26577, 2022.

Parnian Kassraie, Aram-Alexandre Pooladian, Michal Klein, James Thornton, Jonathan Niles-Weed, and Marco Cuturi. Progressive entropic optimal transport solvers. *arXiv preprint arXiv:2406.05061*, 2024.

Bahjat Kawar, Michael Elad, Stefano Ermon, and Jiaming Song. Denoising diffusion restoration models. *Advances in Neural Information Processing Systems*, 35:23593–23606, 2022.

David TB Kelly, Kody JH Law, and Andrew M Stuart. Well-posedness and accuracy of the ensemble kalman filter in discrete and continuous time. *Nonlinearity*, 27(10):2579, 2014.

Filip Ekström Kelvinius, Zheng Zhao, and Fredrik Lindsten. Solving linear-gaussian bayesian inverse problems with decoupled diffusion sequential monte carlo. *arXiv preprint arXiv:2502.06379*, 2025.

Yuehaw Khoo and Lexing Ying. Switchnet: a neural network model for forward and inverse scattering problems. *SIAM Journal on Scientific Computing*, 41(5):A3182–A3201, 2019.

Stanislav Kondratyev, Léonard Monsaingeon, and Dmitry Vorotnikov. A new optimal transport distance on the space of finite radon measures. *Advances in Differential Equations*, 21(11-12):1117–1164, 2016.

Karsten Kreis, Tim Dockhorn, Zihao Li, and Ellen Zhong. Latent space diffusion models of cryo-em structures. *arXiv preprint arXiv:2211.14169*, 2022.

Daniel Lacker. Mean field games and interacting particle systems. *preprint*, 2018.

Marc Lambert, Sinho Chewi, Francis Bach, Silvère Bonnabel, and Philippe Rigollet. Variational inference via wasserstein gradient flows. *Advances in Neural Information Processing Systems*, 35:14434–14447, 2022.

Razvan-Andrei Lascu, Mateusz B Majka, and Łukasz Szpruch. A fisher-rao gradient flow for entropic mean-field min-max games. *arXiv preprint arXiv:2405.15834*, 2024.

Cheuk Kit Lee, Paul Jeha, Jes Frellsen, Pietro Lio, Michael Samuel Albergo, and Francisco Vargas. Debiasing guidance for discrete diffusion with sequential monte carlo. *arXiv preprint arXiv:2502.06079*, 2025.

Axel Levy, Eric R Chan, Sara Fridovich-Keil, Frédéric Poitevin, Ellen D Zhong, and Gordon Wetzstein. Solving inverse problems in protein space using diffusion-based priors. *arXiv preprint arXiv:2406.04239*, 2024.

Gen Li, Yu Huang, Timofey Efimov, Yuting Wei, Yuejie Chi, and Yuxin Chen. Accelerating convergence of score-based diffusion models, provably. *arXiv preprint arXiv:2403.03852*, 2024a.

Matthew Li, Laurent Demanet, and Leonardo Zepeda-Núñez. Accurate and robust deep learning framework for solving wave-based inverse problems in the super-resolution regime. *arXiv preprint arXiv:2106.01143*, 2021.

Matthew Li, Laurent Demanet, and Leonardo Zepeda-Núñez. Wide-band butterfly network: stable and efficient inversion via multi-frequency neural networks. *Multiscale Modeling & Simulation*, 20(4):1191–1227, 2022a.

Xiang Li, John Thickstun, Ishaan Gulrajani, Percy S Liang, and Tatsunori B Hashimoto. Diffusion-lm improves controllable text generation. *Advances in Neural Information Processing Systems*, 35:4328–4343, 2022b.

Xiang Li, Soo Min Kwon, Ismail R Alkhouri, Saiprasad Ravishankar, and Qing Qu. Decoupled data consistency with diffusion purification for image restoration. *arXiv preprint arXiv:2403.06054*, 2024b.

Matthias Liero, Alexander Mielke, and Giuseppe Savaré. Optimal entropy-transport problems and a new hellinger–kantorovich distance between positive measures. *Inventiones mathematicae*, 211(3):969–1117, 2018.

Michael Lindsey. Mne: overparametrized neural evolution with applications to diffusion processes and sampling. *arXiv preprint arXiv:2502.03645*, 2025.

Michael Lindsey, Jonathan Weare, and Anna Zhang. Ensemble markov chain monte carlo with teleporting walkers. *SIAM/ASA Journal on Uncertainty Quantification*, 10(3):860–885, 2022.

Yaron Lipman, Ricky TQ Chen, Heli Ben-Hamu, Maximilian Nickel, and Matt Le. Flow matching for generative modeling. *arXiv preprint arXiv:2210.02747*, 2022.

Jun S Liu. *Monte Carlo strategies in scientific computing*, volume 75. Springer, 2001.

Luping Liu, Yi Ren, Zhijie Lin, and Zhou Zhao. Pseudo numerical methods for diffusion models on manifolds. *arXiv preprint arXiv:2202.09778*, 2022a.

Xingchao Liu, Chengyue Gong, and Qiang Liu. Flow straight and fast: Learning to generate and transfer data with rectified flow. *arXiv preprint arXiv:2209.03003*, 2022b.

Aaron Lou, Chenlin Meng, and Stefano Ermon. Discrete diffusion language modeling by estimating the ratios of the data distribution. *arXiv preprint arXiv:2310.16834*, 2023.

Cheng Lu, Yuhao Zhou, Fan Bao, Jianfei Chen, Chongxuan Li, and Jun Zhu. Dpm-solver: A fast ode solver for diffusion probabilistic model sampling in around 10 steps. *Advances in Neural Information Processing Systems*, 35:5775–5787, 2022a.

Cheng Lu, Yuhao Zhou, Fan Bao, Jianfei Chen, Chongxuan Li, and Jun Zhu. Dpm-solver++: Fast solver for guided sampling of diffusion probabilistic models. *arXiv preprint arXiv:2211.01095*, 2022b.

Jianfeng Lu and Yuliang Wang. Guidance for twisted particle filter: a continuous-time perspective. *arXiv preprint arXiv:2409.02399*, 2024.

Jianfeng Lu and Zhe Wang. The full configuration interaction quantum monte carlo method through the lens of inexact power iteration. *SIAM Journal on Scientific Computing*, 42(1):B1–B29, 2020.

Jianfeng Lu, Yulong Lu, and James Nolen. Scaling limit of the stein variational gradient descent: The mean field regime. *SIAM Journal on Mathematical Analysis*, 51(2):648–671, 2019a.

Yulong Lu, Jianfeng Lu, and James Nolen. Accelerating langevin sampling with birth-death. *arXiv preprint arXiv:1905.09863*, 2019b.

Yulong Lu, Dejan Slepčev, and Lihan Wang. Birth–death dynamics for sampling: global convergence, approximations and their asymptotics. *Nonlinearity*, 36(11):5731, 2023.

Hao Luan, See-Kiong Ng, and Chun Kai Ling. Ddps: Discrete diffusion posterior sampling for paths in layered graphs. *arXiv preprint arXiv:2504.20754*, 2025.

Michael Lustig, David Donoho, and John M Pauly. Sparse mri: The application of compressed sensing for rapid mr imaging. *Magnetic Resonance in Medicine: An Official Journal of the International Society for Magnetic Resonance in Medicine*, 58(6):1182–1195, 2007.

Advaith Maddipatla, Nadav Bojan Sellam, Meital Bojan, Sanketh Vedula, Paul Schanda, Ailie Marx, and Alex M Bronstein. Inverse problems with experiment-guided alphafold. *arXiv preprint arXiv:2502.09372*, 2025.

Aimee Maurais and Youssef Marzouk. Sampling in unit time with kernel fisher-rao flow. *arXiv preprint arXiv:2401.03892*, 2024.

Song Mei, Theodor Misiakiewicz, and Andrea Montanari. Mean-field theory of two-layers neural networks: dimension-free bounds and kernel limit. In *Conference on learning theory*, pp. 2388–2464. PMLR, 2019.

Owen Melia, Olivia Tsang, Vasileios Charisopoulos, Yuehaw Khoo, Jeremy Hoskins, and Rebecca Willett. Multi-frequency progressive refinement for learned inverse scattering. *Journal of Computational Physics*, pp. 113809, 2025.

Chenlin Meng, Kristy Choi, Jiaming Song, and Stefano Ermon. Concrete score matching: Generalized score matching for discrete data. *Advances in Neural Information Processing Systems*, 35:34532–34545, 2022.

Roberto Molinaro, Yunan Yang, Björn Engquist, and Siddhartha Mishra. Neural inverse operators for solving pde inverse problems. *arXiv preprint arXiv:2301.11167*, 2023.

Roberto Molinaro, Samuel Lanthaler, Bogdan Raonić, Tobias Rohner, Victor Armegioiu, Stephan Simonis, Dana Grund, Yannick Ramic, Zhong Yi Wan, Fei Sha, et al. Generative ai for fast and accurate statistical computation of fluids. *arXiv preprint arXiv:2409.18359*, 2024.

Pierre Del Moral. *Feynman-Kac formulae: genealogical and interacting particle systems with applications*. Springer, 2004.

Johannes Müller, Semih Çaycı, and Guido Montúfar. Fisher-rao gradient flows of linear programs and state-action natural policy gradients. *arXiv preprint arXiv:2403.19448*, 2024.

Adrian Muntean, Jens Rademacher, and Antonios Zagaris. *Macroscopic and large scale phenomena: coarse graining, mean field limits and ergodicity*. Springer, 2016.

Naoki Murata, Chieh-Hsin Lai, Yuhta Takida, Toshimitsu Uesaka, Bac Nguyen, Stefano Ermon, and Yuki Mitsufuji. G2d2: Gradient-guided discrete diffusion for image inverse problem solving. *arXiv preprint arXiv:2410.14710*, 2024.

Radford M Neal. Annealed importance sampling. *Statistics and computing*, 11:125–139, 2001.

Radford M Neal et al. Mcmc using hamiltonian dynamics. *Handbook of markov chain monte carlo*, 2(11):2, 2011.

Kirill Neklyudov, Jannes Nys, Luca Thiede, Juan Carrasquilla, Qiang Liu, Max Welling, and Alireza Makhzani. Wasserstein quantum monte carlo: a novel approach for solving the quantum many-body schrödinger equation. *Advances in Neural Information Processing Systems*, 36, 2024.

Jun H Park, Juyeob Lee, and Jungseek Hwang. Solving inverse problems using normalizing flow prior: Application to optical spectra. *Physical Review B*, 109(16):165130, 2024.

Dhruv Patel and Assad A Oberai. Bayesian inference with generative adversarial network priors. *arXiv preprint arXiv:1907.09987*, 2019.

Sahani Pathiraja and Philipp Wacker. Connections between sequential bayesian inference and evolutionary dynamics. *arXiv preprint arXiv:2411.16366*, 2024.

Marcelo Pereyra, Luis A Vargas-Mieles, and Konstantinos C Zygalakis. The split gibbs sampler revisited: improvements to its algorithmic structure and augmented target distribution. *SIAM Journal on Imaging Sciences*, 16(4):2040–2071, 2023.

Vishal Purohit, Matthew Repasky, Jianfeng Lu, Qiang Qiu, Yao Xie, and Xiuyuan Cheng. Posterior sampling via langevin dynamics based on generative priors. *arXiv preprint arXiv:2410.02078*, 2024.

Luping Qu, Mauricio Araya-Polo, and Laurent Demanet. Uncertainty quantification in seismic inversion through integrated importance sampling and ensemble methods. *arXiv preprint arXiv:2409.06840*, 2024.

Pierre-Arnaud Raviart. An analysis of particle methods. In *Numerical Methods in Fluid Dynamics: Lectures given at the 3rd 1983 Session of the Centro Internationale Matematico Estivo (CIME) held at Como, Italy, July 7–15, 1983*, pp. 243–324. Springer, 2006.

Yinuo Ren, Haoxuan Chen, Grant M Rotskoff, and Lexing Ying. How discrete and continuous diffusion meet: Comprehensive analysis of discrete diffusion models via a stochastic integral framework. *arXiv preprint arXiv:2410.03601*, 2024a.

Yinuo Ren, Tesi Xiao, Tanmay Gangwani, Anshuka Rangi, Holakou Rahmanian, Lexing Ying, and Subhajit Sanyal. Multi-objective optimization via wasserstein-fisher-rao gradient flow. In *International Conference on Artificial Intelligence and Statistics*, pp. 3862–3870. PMLR, 2024b.

Yinuo Ren, Haoxuan Chen, Yuchen Zhu, Wei Guo, Yongxin Chen, Grant M Rotskoff, Molei Tao, and Lexing Ying. Fast solvers for discrete diffusion models: Theory and applications of high-order algorithms. *arXiv preprint arXiv:2502.00234*, 2025a.

Yinuo Ren, Grant M Rotskoff, and Lexing Ying. A unified approach to analysis and design of denoising markov models. *arXiv preprint arXiv:2504.01938*, 2025b.

Pierre H Richemond, Sander Dieleman, and Arnaud Doucet. Categorical sdes with simplex diffusion. *arXiv preprint arXiv:2210.14784*, 2022.

Mathias Richter. *Inverse problems: Basics, theory and applications in geophysics*. Springer Nature, 2021.

Eric A Riesel, Tsach Mackey, Hamed Nilforoshan, Minkai Xu, Catherine K Badding, Alison B Altman, Jure Leskovec, and Danna E Freedman. Crystal structure determination from powder diffraction patterns with generative machine learning. *Journal of the American Chemical Society*, 146(44):30340–30348, 2024.

Sergej Rjasanow and Wolfgang Wagner. A stochastic weighted particle method for the boltzmann equation. *Journal of Computational Physics*, 124(2):243–253, 1996.

Gareth O Roberts and Osnat Stramer. Langevin diffusions and metropolis-hastings algorithms. *Methodology and computing in applied probability*, 4:337–357, 2002.

Robin Rombach, Andreas Blattmann, Dominik Lorenz, Patrick Esser, and Björn Ommer. High-resolution image synthesis with latent diffusion models. In *Proceedings of the IEEE/CVF conference on computer vision and pattern recognition*, pp. 10684–10695, 2022.

Litu Rout, Negin Raoof, Giannis Daras, Constantine Caramanis, Alex Dimakis, and Sanjay Shakkottai. Solving linear inverse problems provably via posterior sampling with latent diffusion models. *Advances in Neural Information Processing Systems*, 36:49960–49990, 2023.

Ernest Ryu, Jialin Liu, Sicheng Wang, Xiaohan Chen, Zhangyang Wang, and Wotao Yin. Plug-and-play methods provably converge with properly trained denoisers. In *International Conference on Machine Learning*, pp. 5546–5557. PMLR, 2019.

Javier E Santos, Zachary R Fox, Nicholas Lubbers, and Yen Ting Lin. Blackout diffusion: generative diffusion models in discrete-state spaces. In *International Conference on Machine Learning*, pp. 9034–9059. PMLR, 2023.

Claudia Schillings and Andrew M Stuart. Analysis of the ensemble kalman filter for inverse problems. *SIAM Journal on Numerical Analysis*, 55(3):1264–1290, 2017.

Claudia Schillings and Andrew M Stuart. Convergence analysis of ensemble kalman inversion: the linear, noisy case. *Applicable Analysis*, 97(1):107–123, 2018.

Nikolaus Schweizer. Non-asymptotic error bounds for sequential mcmc and stability of feynman-kac propagators. *arXiv preprint arXiv:1204.2382*, 2012.

Mathieu Sellier. Inverse problems in free surface flows: a review. *Acta Mechanica*, 227(3):913–935, 2016.

Nikil Roashan Selvam, Amil Merchant, and Stefano Ermon. Self-refining diffusion samplers: Enabling parallelization via parareal iterations. *arXiv preprint arXiv:2412.08292*, 2024.

Neta Shaul, Ricky TQ Chen, Maximilian Nickel, Matthew Le, and Yaron Lipman. On kinetic optimal probability paths for generative models. In *International Conference on Machine Learning*, pp. 30883–30907. PMLR, 2023.

Andy Shih, Suneel Belkhale, Stefano Ermon, Dorsa Sadigh, and Nima Anari. Parallel sampling of diffusion models. *Advances in Neural Information Processing Systems*, 36, 2024.

Marta Skreta, Tara Akhound-Sadegh, Viktor Ohanesian, Roberto Bondesan, Alán Aspuru-Guzik, Arnaud Doucet, Rob Brekelmans, Alexander Tong, and Kirill Neklyudov. Feynman-kac correctors in diffusion: Annealing, guidance, and product of experts. *arXiv preprint arXiv:2503.02819*, 2025.

Jascha Sohl-Dickstein, Eric Weiss, Niru Maheswaranathan, and Surya Ganguli. Deep unsupervised learning using nonequilibrium thermodynamics. In *International Conference on Machine Learning*, pp. 2256–2265. PMLR, 2015.

Bowen Song, Soo Min Kwon, Zecheng Zhang, Xinyu Hu, Qing Qu, and Liyue Shen. Solving inverse problems with latent diffusion models via hard data consistency. *arXiv preprint arXiv:2307.08123*, 2023a.

Jiaming Song, Chenlin Meng, and Stefano Ermon. Denoising diffusion implicit models. *arXiv preprint arXiv:2010.02502*, 2020a.

Jiaming Song, Arash Vahdat, Morteza Mardani, and Jan Kautz. Pseudoinverse-guided diffusion models for inverse problems. In *International Conference on Learning Representations*, 2023b.

Jiaming Song, Qinsheng Zhang, Hongxu Yin, Morteza Mardani, Ming-Yu Liu, Jan Kautz, Yongxin Chen, and Arash Vahdat. Loss-guided diffusion models for plug-and-play controllable generation. In *International Conference on Machine Learning*, pp. 32483–32498. PMLR, 2023c.

Yang Song and Stefano Ermon. Generative modeling by estimating gradients of the data distribution. *Advances in neural information processing systems*, 32, 2019.

Yang Song, Jascha Sohl-Dickstein, Diederik P Kingma, Abhishek Kumar, Stefano Ermon, and Ben Poole. Score-based generative modeling through stochastic differential equations. *arXiv preprint arXiv:2011.13456*, 2020b.

Yang Song, Conor Durkan, Iain Murray, and Stefano Ermon. Maximum likelihood training of score-based diffusion models. *Advances in neural information processing systems*, 34:1415–1428, 2021a.

Yang Song, Liyue Shen, Lei Xing, and Stefano Ermon. Solving inverse problems in medical imaging with score-based generative models. *arXiv preprint arXiv:2111.08005*, 2021b.

Bhuvanesh Sridharan, Sarvesh Mehta, Yashaswi Pathak, and U Deva Priyakumar. Deep reinforcement learning for molecular inverse problem of nuclear magnetic resonance spectra to molecular structure. *The Journal of Physical Chemistry Letters*, 13(22):4924–4933, 2022.

Andrew M Stuart. Inverse problems: a bayesian perspective. *Acta numerica*, 19:451–559, 2010.

Haoran Sun, Lijun Yu, Bo Dai, Dale Schuurmans, and Hanjun Dai. Score-based continuous-time discrete diffusion models. *arXiv preprint arXiv:2211.16750*, 2022.

Hongyu Sun and Laurent Demanet. Extrapolated full-waveform inversion with deep learning. *Geophysics*, 85 (3):R275–R288, 2020.

Hongyu Sun and Laurent Demanet. Deep learning for low-frequency extrapolation of multicomponent data in elastic fwi. *IEEE Transactions on Geoscience and Remote Sensing*, 60:1–11, 2021.

Jian Sun, Huibin Li, Zongben Xu, et al. Deep admm-net for compressive sensing mri. *Advances in neural information processing systems*, 29, 2016.

Yu Sun, Zihui Wu, Yifan Chen, Berthy T Feng, and Katherine L Bouman. Provable probabilistic imaging using score-based generative priors. *IEEE Transactions on Computational Imaging*, 2024.

Alain-Sol Sznitman. Topics in propagation of chaos. *Ecole d'été de probabilités de Saint-Flour XIX—1989*, 1464:165–251, 1991.

Denis Talay and Olivier Vaillant. A stochastic particle method with random weights for the computation of statistical solutions of mckean-vlasov equations. *The Annals of Applied Probability*, 13(1):140–180, 2003.

Lezhi Tan and Jianfeng Lu. Accelerate langevin sampling with birth-death process and exploration component. *arXiv preprint arXiv:2305.05529*, 2023.

Zhiwei Tang, Jiasheng Tang, Hao Luo, Fan Wang, and Tsung-Hui Chang. Accelerating parallel sampling of diffusion models. *arXiv preprint arXiv:2402.09970*, 2024.

Pingping Tao, Haixia Liu, Jing Su, Xiaochen Yang, and Hongchen Tan. Map-based problem-agnostic diffusion model for inverse problems. *arXiv preprint arXiv:2501.15128*, 2025.

Jiachen Tu, Yaokun Shi, and Fan Lam. Score-based self-supervised mri denoising. In *The Thirteenth International Conference on Learning Representations*, 2025.

Masatoshi Uehara, Yulai Zhao, Chenyu Wang, Xiner Li, Aviv Regev, Sergey Levine, and Tommaso Biancalani. Reward-guided controlled generation for inference-time alignment in diffusion models: Tutorial and review. *arXiv preprint arXiv:2501.09685*, 2025.

Francisco Vargas, Shreyas Padhy, Denis Blessing, and Nikolas Nüsken. Transport meets variational inference: Controlled monte carlo diffusions. *arXiv preprint arXiv:2307.01050*, 2023.

Alexander Vidal, Samy Wu Fung, Luis Tenorio, Stanley Osher, and Levon Nurbekyan. Taming hyperparameter tuning in continuous normalizing flows using the jko scheme. *Scientific reports*, 13(1):4501, 2023.

Pascal Vincent. A connection between score matching and denoising autoencoders. *Neural computation*, 23 (7):1661–1674, 2011.

Maxime Vono, Nicolas Dobigeon, and Pierre Chainais. Split-and-augmented gibbs sampler—application to large-scale inference problems. *IEEE Transactions on Signal Processing*, 67(6):1648–1661, 2019.

Austin Wang, Hongkai Zheng, Zihui Wu, Ricardo Baptista, Daniel Zhengyu Huang, and Yisong Yue. Ensemble kalman sampling and diffusion prior in tandem: A split gibbs framework. In *Frontiers in Probabilistic Inference: Learning meets Sampling*, 2025.

Yilun Wang, Junfeng Yang, Wotao Yin, and Yin Zhang. A new alternating minimization algorithm for total variation image reconstruction. *SIAM Journal on Imaging Sciences*, 1(3):248–272, 2008.

Yinhuai Wang, Jiwen Yu, and Jian Zhang. Zero-shot image restoration using denoising diffusion null-space model. *arXiv preprint arXiv:2212.00490*, 2022.

Yuqing Wang, Ye He, and Molei Tao. Evaluating the design space of diffusion-based generative models. *arXiv preprint arXiv:2406.12839*, 2024.

Joseph L Watson, David Juergens, Nathaniel R Bennett, Brian L Trippe, Jason Yim, Helen E Eisenach, Woody Ahern, Andrew J Borst, Robert J Ragotte, Lukas F Milles, et al. De novo design of protein structure and function with rfdiffusion. *Nature*, 620(7976):1089–1100, 2023.

Max Welling and Yee W Teh. Bayesian learning via stochastic gradient langevin dynamics. In *Proceedings of the 28th international conference on machine learning (ICML-11)*, pp. 681–688. Citeseer, 2011.

Jay Whang, Qi Lei, and Alex Dimakis. Solving inverse problems with a flow-based noise model. In *International Conference on Machine Learning*, pp. 11146–11157. PMLR, 2021a.

Jay Whang, Erik Lindgren, and Alex Dimakis. Composing normalizing flows for inverse problems. In *International Conference on Machine Learning*, pp. 11158–11169. PMLR, 2021b.

Veit David Wild, Sahra Ghalebikesabi, Dino Sejdinovic, and Jeremias Knoblauch. A rigorous link between deep ensembles and (variational) bayesian methods. *Advances in Neural Information Processing Systems*, 36:39782–39811, 2023.

Luhuan Wu, Brian Trippe, Christian Naesseth, David Blei, and John P Cunningham. Practical and asymptotically exact conditional sampling in diffusion models. *Advances in Neural Information Processing Systems*, 36:31372–31403, 2023.

Yuchen Wu, Minshuo Chen, Zihao Li, Mengdi Wang, and Yuting Wei. Theoretical insights for diffusion guidance: A case study for gaussian mixture models. *arXiv preprint arXiv:2403.01639*, 2024a.

Yuchen Wu, Yuxin Chen, and Yuting Wei. Stochastic runge-kutta methods: Provable acceleration of diffusion models. *arXiv preprint arXiv:2410.04760*, 2024b.

Zihui Wu, Yu Sun, Yifan Chen, Bingliang Zhang, Yisong Yue, and Katherine Bouman. Principled probabilistic imaging using diffusion models as plug-and-play priors. *Advances in Neural Information Processing Systems*, 37:118389–118427, 2024c.

Jinxi Xiang, Yonggui Dong, and Yunjie Yang. Fista-net: Learning a fast iterative shrinkage thresholding network for inverse problems in imaging. *IEEE Transactions on Medical Imaging*, 40(5):1329–1339, 2021.

Yao Xie and Xiuyuan Cheng. Flow-based generative models as iterative algorithms in probability space. *arXiv preprint arXiv:2502.13394*, 2025.

Chen Xu, Xiuyuan Cheng, and Yao Xie. Normalizing flow neural networks by jko scheme. *Advances in Neural Information Processing Systems*, 36, 2024.

Minkai Xu, Lantao Yu, Yang Song, Chence Shi, Stefano Ermon, and Jian Tang. Geodiff: A geometric diffusion model for molecular conformation generation. *arXiv preprint arXiv:2203.02923*, 2022.

Wuzhe Xu, Yulong Lu, Anqing Xuan, Ali Barzegari, et al. Diffusion-based models for unpaired super-resolution in fluid dynamics. *arXiv preprint arXiv:2504.05443*, 2025.

Xingyu Xu and Yuejie Chi. Provably robust score-based diffusion posterior sampling for plug-and-play image reconstruction. *arXiv preprint arXiv:2403.17042*, 2024.

Yuling Yan, Kaizheng Wang, and Philippe Rigollet. Learning gaussian mixtures using the wasserstein–fisher–rao gradient flow. *The Annals of Statistics*, 52(4):1774–1795, 2024.

Rentian Yao, Linjun Huang, and Yun Yang. Minimizing convex functionals over space of probability measures via kl divergence gradient flow. In *International Conference on Artificial Intelligence and Statistics*, pp. 2530–2538. PMLR, 2024.

Haotian Ye, Haowei Lin, Jiaqi Han, Minkai Xu, Sheng Liu, Yitao Liang, Jianzhu Ma, James Y Zou, and Stefano Ermon. Tfg: Unified training-free guidance for diffusion models. *Advances in Neural Information Processing Systems*, 37:22370–22417, 2024.

Lexing Ying. On lyapunov functions and particle methods for regularized minimax problems. *Research in the Mathematical Sciences*, 9(2):18, 2022a.

Lexing Ying. Solving inverse problems with deep learning. In *Proceedings of the International Congress of Mathematicians*, volume 7, pp. 5154–5175, 2022b.

Hongkee Yoon, Jae-Hoon Sim, and Myung Joon Han. Analytic continuation via domain knowledge free machine learning. *Physical Review B*, 98(24):245101, 2018.

Benjamin J Zhang and Markos A Katsoulakis. A mean-field games laboratory for generative modeling. *arXiv preprint arXiv:2304.13534*, 2023.

Bingliang Zhang, Zihui Wu, Berthy T Feng, Yang Song, Yisong Yue, and Katherine L Bouman. Step: A general and scalable framework for solving video inverse problems with spatiotemporal diffusion priors. *arXiv preprint arXiv:2504.07549*, 2025a.

Borong Zhang, Martín Guerra, Qin Li, and Leonardo Zepeda-Núñez. Back-projection diffusion: Solving the wideband inverse scattering problem with diffusion models. *arXiv preprint arXiv:2408.02866*, 2024a.

Huan Zhang, Yifan Chen, Eric Vanden-Eijnden, and Benjamin Peherstorfer. Sequential-in-time training of nonlinear parametrizations for solving time-dependent partial differential equations. *arXiv preprint arXiv:2404.01145*, 2024b.

Jian Zhang and Bernard Ghanem. Ista-net: Interpretable optimization-inspired deep network for image compressive sensing. In *Proceedings of the IEEE conference on computer vision and pattern recognition*, pp. 1828–1837, 2018.

Leo Zhang, Peter Potaptchik, Arnaud Doucet, Hai-Dang Dau, and Saifuddin Syed. Generalised parallel tempering: Flexible replica exchange via flows and diffusions. *arXiv preprint arXiv:2502.10328*, 2025b.

Linfeng Zhang, Weinan E, and Lei Wang. Monge-ampère flow for generative modeling. *arXiv preprint arXiv:1809.10188*, 2018a.

Richard Zhang, Phillip Isola, Alexei A Efros, Eli Shechtman, and Oliver Wang. The unreasonable effectiveness of deep features as a perceptual metric. In *Proceedings of the IEEE conference on computer vision and pattern recognition*, pp. 586–595, 2018b.

Shumao Zhang, Pengchuan Zhang, and Thomas Y Hou. Multiscale invertible generative networks for high-dimensional bayesian inference. In *International Conference on Machine Learning*, pp. 12632–12641. PMLR, 2021.

Yasi Zhang, Peiyu Yu, Yaxuan Zhu, Yingshan Chang, Feng Gao, Ying Nian Wu, and Oscar Leong. Flow priors for linear inverse problems via iterative corrupted trajectory matching. *arXiv preprint arXiv:2405.18816*, 2024c.

Hongkai Zheng, Wenda Chu, Austin Wang, Nikola Kovachki, Ricardo Baptista, and Yisong Yue. Ensemble kalman diffusion guidance: A derivative-free method for inverse problems. *arXiv preprint arXiv:2409.20175*, 2024.

Hongkai Zheng, Wenda Chu, Bingliang Zhang, Zihui Wu, Austin Wang, Berthy T Feng, Caifeng Zou, Yu Sun, Nikola Kovachki, Zachary E Ross, et al. Inversebench: Benchmarking plug-and-play diffusion priors for inverse problems in physical sciences. *arXiv preprint arXiv:2503.11043*, 2025.

Kaiwen Zheng, Cheng Lu, Jianfei Chen, and Jun Zhu. Dpm-solver-v3: Improved diffusion ode solver with empirical model statistics. *Advances in Neural Information Processing Systems*, 36:55502–55542, 2023.

Mo Zhou, Jiequn Han, Manas Rachh, and Carlos Borges. A neural network warm-start approach for the inverse acoustic obstacle scattering problem. *Journal of Computational Physics*, 490:112341, 2023.

Huminhao Zhu, Fangyikang Wang, Chao Zhang, Hanbin Zhao, and Hui Qian. Neural sinkhorn gradient flow. *arXiv preprint arXiv:2401.14069*, 2024a.

Yiheng Zhu, Jialu Wu, Qiuyi Li, Jiahuan Yan, Mingze Yin, Wei Wu, Mingyang Li, Jieping Ye, Zheng Wang, and Jian Wu. Bridge-if: Learning inverse protein folding with markov bridges. *arXiv preprint arXiv:2411.02120*, 2024b.

Yuanzhi Zhu, Zhaohai Li, Tianwei Wang, Mengchao He, and Cong Yao. Conditional text image generation with diffusion models. In *Proceedings of the IEEE/CVF Conference on Computer Vision and Pattern Recognition*, pp. 14235–14245, 2023.

Yuchen Zhu, Tianrong Chen, Evangelos A Theodorou, Xie Chen, and Molei Tao. Quantum state generation with structure-preserving diffusion model. *arXiv preprint arXiv:2404.06336*, 2024c.

A   Further Discussion on Related Work and Notations

In this section, we provide additional discussion and context around our work through a comprehensive literature review and clarification of notations used throughout the paper.

A.1   Related Work

In this subsection, we provide a more comprehensive overview of related work.

Solving Inverse Problems via Machine Learning Techniques   A wide body of work has tried applying machine learning (ML) based techniques to tackle inverse problems. In particular, one class of such ML-based methods deploy the Maximum a posteriori (MAP) approach by directly modeling the inverse mapping via some neural network. In the context of physical sciences, examples of work include (Yoon et al., 2018; Khoo & Ying, 2019; Fan & Ying, 2019a;b; 2020; Fournier et al., 2020; Sun & Demanet, 2020; 2021; Li et al., 2021; 2022a; Zhou et al., 2023; Fan & Ying, 2023; Molinaro et al., 2023; Melia et al., 2025). For a more detailed overview of methods belonging to such class, one may refer to (Arridge et al., 2019; Ying, 2022b). Similar methodologies (Zhang & Ghanem, 2018; Gilton et al., 2019; Xiang et al., 2021) have also been applied to inverse problems in computational imaging and computer vision. The second class of ML-based methods (Hou et al., 2019; Zhang et al., 2021; Whang et al., 2021a; Park et al., 2024; Tao et al., 2025; Dasgupta et al., 2025), however, employ a Bayesian approach by leveraging generative priors like normalizing flows and diffusion models. Such methods have been widely applied in various areas like medical imaging (Song et al., 2021b; Chung & Ye, 2022; Tu et al., 2025), cryo-electron microscopy (Kreis et al., 2022; Levy et al., 2024), PDE-constrained inverse problems (Jiang et al., 2025), sampling marginal densities (Lindsey, 2025), inverse scattering (Zhang et al., 2024a), traveltime tomography (Cao & Zhang, 2024), nonlinear data assimilation (Ding et al., 2024), inverse protein folding (Hsu et al., 2022; Zhu et al., 2024b), as well as fluid dynamics (Chen et al., 2024d; Xu et al., 2025; Molinaro et al., 2024). For a complete review of applying diffusion models to solve inverse problems, one may refer to (Daras et al., 2024a). Moreover,

for the second class of methods that deploy a posterior sampling approach, recent work have also tried to combine diffusion models with existing sampling methods like SMC (Wu et al., 2023; Cardoso et al., 2023; Dou & Song, 2024; Albergo & Vanden-Eijnden, 2024; Chen et al., 2024b; Vargas et al., 2023), SGS (Xu & Chi, 2024; Wu et al., 2024c; Wang et al., 2025), parallel tempering (Zhang et al., 2025b) and ensemble Kalman filtering (Zheng et al., 2024). For methods using gradients of the log-likelihood in their algorithm design, we note that they also relate to guidance-based methods (Dhariwal & Nichol, 2021; Wu et al., 2024a; Chidambaram et al., 2024; Ho & Salimans, 2022; Bansal et al., 2023; Song et al., 2023c; He et al., 2023; Guo et al., 2024; Ye et al., 2024) proposed for conditional sampling.

Gradient Flows for Sampling and Generative Modeling Gradient flow perspectives, particularly those based on the Wasserstein metric with foundational insights stemming from optimal transport and the JKO scheme (Jordan et al., 1998), have been extensively studied for both sampling and variational inference. Recent work in this direction includes (Gao et al., 2019; Ansari et al., 2020; Fan et al., 2021; Lambert et al., 2022; Diao et al., 2023), with ongoing developments such as (Wild et al., 2023; Shaul et al., 2023; Zhang & Katsoulakis, 2023; Cheng et al., 2024b; Yao et al., 2024; Choi et al., 2024; Zhu et al., 2024a). Other recent work (Vidal et al., 2023; Cheng et al., 2024a; Xu et al., 2024; Xie & Cheng, 2025; Boffi et al., 2024; Kassraie et al., 2024) also discuss algorithms formulated via proximal operators and local-map learning strategies. Related developments in quantum Monte Carlo (QMC), particularly diffusion Monte Carlo (DMC) (Caffarel & Claverie, 1988a;b), are reviewed in (Gubernatis et al., 2016; Becca & Sorella, 2017) with further applications to quantum many-body problems discussed in (Lu & Wang, 2020).

(Stochastic) Weighted Particle Methods and Wasserstein-Fisher-Rao Dynamics Weighted particle methods, such as those based on the birth-death process and Wasserstein–Fisher–Rao (WFR) distances (Kondratyev et al., 2016; Liero et al., 2018; Chizat et al., 2018)has motivated a series of studies on ensemble-based sampling dynamics (Lindsey et al., 2022; Lu et al., 2019b; Maurais & Marzouk, 2024; Gabrié et al., 2022; Tan & Lu, 2023; Chen & Ying, 2024a; Pathiraja & Wacker, 2024) that have been applied to solving high-dimensional Bayesian inverse problems (Qu et al., 2024; Chen et al., 2024e) and PDEs (Han et al., 2020; Zhang et al., 2024b; Neklyudov et al., 2024; Chen et al., 2024f). These techniques have also been applied to multi-objective optimization (Ren et al., 2024b), density estimation via Gaussian mixtures (Chen et al., 2023b; Yan et al., 2024), and reinforcement learning and MDPs (Müller et al., 2024). Their connection to min-max optimization is explored in (Domingo-Enrich et al., 2020; Ying, 2022a; Lascu et al., 2024).

A.2 Notations

We use $\nabla_{\boldsymbol{x}}, \nabla_{\boldsymbol{x}}\cdot$ and $\Delta_{\boldsymbol{x}}$ to denote the gradient, divergence, and Laplacian operators with respect to any fixed variable $\boldsymbol{x}$. The set of positive real numbers is denoted by $\mathbb{R}^+$. We further use δ for the Dirac delta function. For measuring distances between probability distributions, we use the Kullback-Leibler (KL) divergence D_{KL}, Total Variation (TV) divergence TV, and Wasserstein-p distance $\mathcal{W}_p$. The l_2 norm is denoted by $\|\cdot\|_2^2$.

B Supplementary Proofs and Justifications for Section 3

In this section, we provide detailed proofs and justifications for claims listed in Section 3. We will use the shorthand notation $f_{\boldsymbol{y}}(\boldsymbol{x}) = \exp(\mu_{\boldsymbol{y}}(\boldsymbol{x}))$ for the time-independent likelihood factor.

Lemma B.1. *The PDE dynamics governing the evolution of the unnormalized posterior distribution $\widehat{Q}_{\boldsymbol{y}}(\boldsymbol{x},t):\mathbb{R}^n \times [0,T] \to \mathbb{R}^+$ is given by*

$$
\begin{aligned}
\frac{\partial}{\partial t}\widehat{Q}_{\boldsymbol{y}} = &- \nabla_{\boldsymbol{x}} \cdot \left(\left(\widehat{\boldsymbol{H}}(\boldsymbol{x},t) - V(t)^2 \nabla_{\boldsymbol{x}}\mu_{\boldsymbol{y}} \right) \widehat{Q}_{\boldsymbol{y}} \right) + \frac{1}{2}V(t)^2 \Delta_x \widehat{Q}_{\boldsymbol{y}} \\
&+ \left(\frac{1}{2}V(t)^2 \left(\|\nabla_{\boldsymbol{x}}\mu_{\boldsymbol{y}}\|_2^2 - \Delta_{\boldsymbol{x}}\mu_{\boldsymbol{y}} \right) - \widehat{\boldsymbol{H}}(\boldsymbol{x},t)^{\mathsf{T}}\nabla_{\boldsymbol{x}}\mu_{\boldsymbol{y}} \right) \widehat{Q}_{\boldsymbol{y}},
\end{aligned}
\tag{B.1}
$$

where

$$
\widehat{\boldsymbol{H}}(\boldsymbol{x},t) := -F(t)\boldsymbol{x} + \frac{G(t)^2 + V(t)^2}{2}\phi_\theta(\boldsymbol{x},t)
\tag{B.2}
$$

denotes the original drift in the prior diffusion.

Proof. We begin by rewriting the PDE dynamics that need simplification:

$$\frac{\partial}{\partial t}\widehat{Q}_{\boldsymbol{y}} = -\frac{1}{f_{\boldsymbol{y}}}\nabla_{\boldsymbol{x}}\cdot\left(\widehat{\boldsymbol{H}}(\boldsymbol{x},t)\widehat{Q}_{\boldsymbol{y}}f_{\boldsymbol{y}}\right) + \frac{1}{2f_{\boldsymbol{y}}}V(t)^2\Delta_x(\widehat{Q}_{\boldsymbol{y}}f_{\boldsymbol{y}}). \tag{B.3}$$

Let I_1 and I_2 denote the two terms on the right-hand side:

$$I_1 := -\frac{1}{f_{\boldsymbol{y}}}\nabla_{\boldsymbol{x}}\cdot\left(\widehat{\boldsymbol{H}}(\boldsymbol{x},t)\widehat{Q}_{\boldsymbol{y}}f_{\boldsymbol{y}}\right),\ I_2 := \frac{1}{2f_{\boldsymbol{y}}}V(t)^2\Delta_x(\widehat{Q}_{\boldsymbol{y}}f_{\boldsymbol{y}}). \tag{B.4}$$

Note that $\widehat{\boldsymbol{H}}(\boldsymbol{x},t) : \mathbb{R}^{n+1} \to \mathbb{R}^n$ is vector-valued, while both $\widehat{Q}_{\boldsymbol{y}} : \mathbb{R}^{n+1} \to \mathbb{R}$ and $f_{\boldsymbol{y}} : \mathbb{R}^n \to \mathbb{R}$ are scalar-valued. A direct computation shows that the first term I_1 simplifies to:

$$\begin{aligned}
I_1 &= -\frac{1}{f_{\boldsymbol{y}}}\nabla_{\boldsymbol{x}}\cdot\left(\widehat{\boldsymbol{H}}(\boldsymbol{x},t)\widehat{Q}_{\boldsymbol{y}}f_{\boldsymbol{y}}\right)\\
&= -\frac{1}{f_{\boldsymbol{y}}}\left(\nabla_{\boldsymbol{x}}\cdot\left(\widehat{\boldsymbol{H}}(\boldsymbol{x},t)\right)\widehat{Q}_{\boldsymbol{y}}f_{\boldsymbol{y}} + \widehat{\boldsymbol{H}}(\boldsymbol{x},t)^{\mathsf{T}}\nabla_{\boldsymbol{x}}\left(\widehat{Q}_{\boldsymbol{y}}f_{\boldsymbol{y}}\right)\right)\\
&= -\nabla_{\boldsymbol{x}}\cdot\left(\widehat{\boldsymbol{H}}(\boldsymbol{x},t)\right)\widehat{Q}_{\boldsymbol{y}} - \frac{1}{f_{\boldsymbol{y}}}\widehat{\boldsymbol{H}}(\boldsymbol{x},t)^{\mathsf{T}}\left(\nabla_{\boldsymbol{x}}\widehat{Q}_{\boldsymbol{y}}f_{\boldsymbol{y}} + \widehat{Q}_{\boldsymbol{y}}\nabla_{\boldsymbol{x}}f_{\boldsymbol{y}}\right)\\
&= -\nabla_{\boldsymbol{x}}\cdot\left(\widehat{\boldsymbol{H}}(\boldsymbol{x},t)\right)\widehat{Q}_{\boldsymbol{y}} - \widehat{\boldsymbol{H}}(\boldsymbol{x},t)^{\mathsf{T}}\nabla_{\boldsymbol{x}}\widehat{Q}_{\boldsymbol{y}} - \left(\widehat{\boldsymbol{H}}(\boldsymbol{x},t)^{\mathsf{T}}\nabla_{\boldsymbol{x}}\mu_{\boldsymbol{y}}\right)\widehat{Q}_{\boldsymbol{y}},
\end{aligned} \tag{B.5}$$

where the last equality above follows from the fact that $\frac{1}{f_{\boldsymbol{y}}}\nabla_{\boldsymbol{x}}f_{\boldsymbol{y}} = \nabla_{\boldsymbol{x}}\mu_{\boldsymbol{y}}$ for $f_{\boldsymbol{y}} = \exp(\mu_{\boldsymbol{y}})$.

Similarly, expanding the Laplacian term $\Delta_{\boldsymbol{x}}(\widehat{Q}_{\boldsymbol{y}}f_{\boldsymbol{y}})$ allows us to simplify the second term I_2

$$\begin{aligned}
I_2 &= \frac{1}{2f_{\boldsymbol{y}}}V(t)^2\left(\left(\Delta_{\boldsymbol{x}}\widehat{Q}_{\boldsymbol{y}}\right)f_{\boldsymbol{y}} + 2\left(\nabla_{\boldsymbol{x}}\widehat{Q}_{\boldsymbol{y}}\right)^{\mathsf{T}}\nabla_{\boldsymbol{x}}f_{\boldsymbol{y}} + \widehat{Q}_{\boldsymbol{y}}\left(\Delta_{\boldsymbol{x}}f_{\boldsymbol{y}}\right)\right)\\
&= \frac{1}{2}V(t)^2\Delta_{\boldsymbol{x}}\widehat{Q}_{\boldsymbol{y}} + V(t)^2\left(\nabla_{\boldsymbol{x}}\widehat{Q}_{\boldsymbol{y}}\right)^{\mathsf{T}}\nabla_{\boldsymbol{x}}\mu_{\boldsymbol{y}} + \frac{1}{2}V(t)^2\left(\Delta_{\boldsymbol{x}}\mu_{\boldsymbol{y}} + \|\nabla_{\boldsymbol{x}}\mu_{\boldsymbol{y}}\|_2^2\right)\widehat{Q}_{\boldsymbol{y}},
\end{aligned} \tag{B.6}$$

where the last equality above follows from the fact that $\frac{1}{f_{\boldsymbol{y}}}\Delta_{\boldsymbol{x}}f_{\boldsymbol{y}} = \Delta_{\boldsymbol{x}}\mu_{\boldsymbol{y}} + \|\nabla_{\boldsymbol{x}}\mu_{\boldsymbol{y}}\|_2^2$ for $f_{\boldsymbol{y}} = \exp(\mu_{\boldsymbol{y}})$.

Summing the two expressions in (B.5) and (B.6) then yields

$$\begin{aligned}
\frac{\partial}{\partial t}\widehat{Q}_{\boldsymbol{y}} = I_1 + I_2 &= -\nabla_{\boldsymbol{x}}\cdot\left(\widehat{\boldsymbol{H}}(\boldsymbol{x},t)\right)\widehat{Q}_{\boldsymbol{y}} + \left(V(t)^2\nabla_{\boldsymbol{x}}\mu_{\boldsymbol{y}} - \widehat{\boldsymbol{H}}(\boldsymbol{x},t)\right)^{\mathsf{T}}\nabla_{\boldsymbol{x}}\widehat{Q}_{\boldsymbol{y}}\\
&\quad + \frac{1}{2}V(t)^2\Delta_{\boldsymbol{x}}\widehat{Q}_{\boldsymbol{y}} + \left(\frac{1}{2}V(t)^2\left(\Delta_{\boldsymbol{x}}\mu_{\boldsymbol{y}} + \|\nabla_{\boldsymbol{x}}\mu_{\boldsymbol{y}}\|_2^2\right) - \widehat{\boldsymbol{H}}(\boldsymbol{x},t)^{\mathsf{T}}\nabla_{\boldsymbol{x}}\mu_{\boldsymbol{y}}\right)\widehat{Q}_{\boldsymbol{y}}\\
&= -\nabla_{\boldsymbol{x}}\cdot\left(\left(\widehat{\boldsymbol{H}}(\boldsymbol{x},t) - V(t)^2\nabla_{\boldsymbol{x}}\mu_{\boldsymbol{y}}\right)\widehat{Q}_{\boldsymbol{y}}\right) - V(t)^2\Delta_{\boldsymbol{x}}\mu_{\boldsymbol{y}}\widehat{Q}_{\boldsymbol{y}}\\
&\quad + \frac{1}{2}V(t)^2\Delta_{\boldsymbol{x}}\widehat{Q}_{\boldsymbol{y}} + \left(\frac{1}{2}V(t)^2\left(\|\nabla_{\boldsymbol{x}}\mu_{\boldsymbol{y}}\|_2^2 + \Delta_{\boldsymbol{x}}\mu_{\boldsymbol{y}}\right) - \widehat{\boldsymbol{H}}(\boldsymbol{x},t)^{\mathsf{T}}\nabla_{\boldsymbol{x}}\mu_{\boldsymbol{y}}\right)\widehat{Q}_{\boldsymbol{y}}
\end{aligned} \tag{B.7}$$

which is exactly the dynamics given in (B.1), as desired. $\qquad\square$

Lemma B.2. *Consider the following PDE dynamics governing the evolution of some unnormalized density* $\widehat{Q}(\boldsymbol{x},t) : \mathbb{R}^n \times [0,T] \to \mathbb{R}^+$

$$\frac{\partial}{\partial t}\widehat{Q}(\boldsymbol{x},t) = -\nabla_{\boldsymbol{x}}\cdot\left(K(\boldsymbol{x},t)\widehat{Q}(\boldsymbol{x},t)\right) + \zeta(t)\Delta_{\boldsymbol{x}}\widehat{Q}(\boldsymbol{x},t) + J(\boldsymbol{x},t)\widehat{Q}(\boldsymbol{x},t), \tag{B.8}$$

where $\zeta : [0,T] \to \mathbb{R}^+$ *and* $K,J : \mathbb{R}^d \times [0,T] \to \mathbb{R}$. *Then we consider the normalized density* $\widehat{q}(\boldsymbol{x},t) : \mathbb{R}^n \times [0,T] \to [0,1]$ *defined as below*

$$\widehat{q}(\boldsymbol{x},t) := \frac{\widehat{Q}(\boldsymbol{x},t)}{\int_{\mathbb{R}^n}\widehat{Q}(\boldsymbol{x},t)\mathrm{d}\boldsymbol{x}},\ t \in [0,T]. \tag{B.9}$$

The PDE dynamics governing the evolution of the normalized density $\widehat{q}(\boldsymbol{x}, t)$ is then given by

$$
\begin{aligned}
\frac{\partial}{\partial t}\widehat{q}(\boldsymbol{x}, t) = &-\nabla_{\boldsymbol{x}} \cdot (K(\boldsymbol{x}, t)\widehat{q}(\boldsymbol{x}, t)) + \zeta(t)\Delta_{\boldsymbol{x}}\widehat{q}(\boldsymbol{x}, t) \\
&+ \left(J(\boldsymbol{x}, t) - \int_{\mathbb{R}^n} J(\boldsymbol{x}, t)\widehat{q}(\boldsymbol{x}, t)\mathrm{d}\boldsymbol{x} \right) \widehat{q}(\boldsymbol{x}, t).
\end{aligned}
\tag{B.10}
$$

Proof. By using $Z(t) := \int_{\mathbb{R}^n} \widehat{Q}(\boldsymbol{x}, t)\mathrm{d}\boldsymbol{x}$ to denote the normalizing constant for any $t \in [0, T]$, we can then compute the time derivative of $Z(t)$ by plugging in (B.8) as follows

$$
\begin{aligned}
\frac{\partial}{\partial t}Z(t) &= \frac{\partial}{\partial t}\left(\int_{\mathbb{R}^n} \widehat{Q}(\boldsymbol{x}, t)\mathrm{d}\boldsymbol{x} \right) = \int_{\mathbb{R}^n} \left(\frac{\partial}{\partial t}\widehat{Q}(\boldsymbol{x}, t) \right)\mathrm{d}\boldsymbol{x} \\
&= \int_{\mathbb{R}^n} \left(-\nabla_{\boldsymbol{x}} \cdot \left(K(\boldsymbol{x}, t)\widehat{Q}(\boldsymbol{x}, t) \right) + \zeta(t)\Delta_{\boldsymbol{x}}\widehat{Q}(\boldsymbol{x}, t) + J(\boldsymbol{x}, t)\widehat{Q}(\boldsymbol{x}, t) \right)\mathrm{d}\boldsymbol{x} \\
&= \int_{\mathbb{R}^n} J(\boldsymbol{x}, t)\widehat{Q}(\boldsymbol{x}, t)\mathrm{d}\boldsymbol{x} + \int_{\mathbb{R}^n} \nabla_{\boldsymbol{x}} \cdot \left(\zeta(t)\nabla_{\boldsymbol{x}}\widehat{Q}(\boldsymbol{x}, t) - K(\boldsymbol{x}, t)\widehat{Q}(\boldsymbol{x}, t) \right)\mathrm{d}\boldsymbol{x} \\
&= \int_{\mathbb{R}^n} J(\boldsymbol{x}, t)\widehat{Q}(\boldsymbol{x}, t)\mathrm{d}\boldsymbol{x}.
\end{aligned}
\tag{B.11}
$$

Furthermore, we may rewrite the normalized density as $\widehat{q}(\boldsymbol{x}, t) = \frac{1}{Z(t)}\widehat{Q}(\boldsymbol{x}, t)$ and differentiate the expression with respect to t, which yields

$$
\begin{aligned}
\frac{\partial}{\partial t}\widehat{q}(\boldsymbol{x}, t) &= \frac{1}{Z(t)^2}\left(\left(\frac{\partial}{\partial t}\widehat{Q}(\boldsymbol{x}, t) \right)Z(t) - \left(\frac{\partial}{\partial t}Z(t) \right)\widehat{Q}(\boldsymbol{x}, t) \right) \\
&= \frac{1}{Z(t)}\left(\frac{\partial}{\partial t}\widehat{Q}(\boldsymbol{x}, t) \right) - \frac{1}{Z(t)}\left(\frac{\partial}{\partial t}Z(t) \right)\left(\frac{1}{Z(t)}\widehat{Q}(\boldsymbol{x}, t) \right) \\
&= \frac{1}{Z(t)}\left(-\nabla_{\boldsymbol{x}} \cdot \left(K(\boldsymbol{x}, t)\widehat{Q}(\boldsymbol{x}, t) \right) + \zeta(t)\Delta_{\boldsymbol{x}}\widehat{Q}(\boldsymbol{x}, t) + J(\boldsymbol{x}, t)\widehat{Q}(\boldsymbol{x}, t) \right) \\
&\quad - \frac{1}{Z(t)}\left(\int_{\mathbb{R}^n} J(\boldsymbol{x}, t)\widehat{Q}(\boldsymbol{x}, t)\mathrm{d}\boldsymbol{x} \right)\widehat{q}(\boldsymbol{x}, t) \\
&= -\nabla_{\boldsymbol{x}} \cdot (K(\boldsymbol{x}, t)\widehat{q}(\boldsymbol{x}, t)) + \zeta(t)\Delta_{\boldsymbol{x}}\widehat{q}(\boldsymbol{x}, t) + \left(J(\boldsymbol{x}, t) - \int_{\mathbb{R}^n} J(\boldsymbol{x}, t)\widehat{q}(\boldsymbol{x}, t)\mathrm{d}\boldsymbol{x} \right)\widehat{q}(\boldsymbol{x}, t).
\end{aligned}
$$

where the second last equality above follows from (B.8) and (B.11) the last equality is deduced from the definition of the normalized density $\widehat{q}(\boldsymbol{x}, t)$. This concludes our proof. $\qquad\square$

Remark B.3. *By setting*

$$
K(\boldsymbol{x}, t) := \widehat{\boldsymbol{H}}(\boldsymbol{x}, t) - V(t)^2\nabla_{\boldsymbol{x}}\mu_{\boldsymbol{y}}(\boldsymbol{x}), \quad \zeta(t) := \frac{1}{2}V(t)^2,
$$

and

$$
J(\boldsymbol{x}, t) := \frac{1}{2}V(t)^2 \left(\|\nabla_{\boldsymbol{x}}\mu_{\boldsymbol{y}}(\boldsymbol{x})\|_2^2 - \Delta_{\boldsymbol{x}}\mu_{\boldsymbol{y}}(\boldsymbol{x}) \right) - \widehat{\boldsymbol{H}}(\boldsymbol{x}, t)^\intercal\nabla_{\boldsymbol{x}}\mu_{\boldsymbol{y}}(\boldsymbol{x}),
$$

one can use Lemma B.2 to deduce (3.4) from (3.3).

Lemma B.4. *Consider a single particle $(\boldsymbol{x}_t, \beta_t)$ governed by*

$$
\begin{cases}
\mathrm{d}\boldsymbol{x}_t &= \left(\widehat{\boldsymbol{H}}(\boldsymbol{x}_t, t) - V(t)^2\nabla_{\boldsymbol{x}}\mu_{\boldsymbol{y}}(\boldsymbol{x}_t) \right)\mathrm{d}t + V(t)\mathrm{d}\boldsymbol{w}_t, \\
\mathrm{d}\beta_t &= \left(U(\boldsymbol{x}_t, t) - \widehat{\boldsymbol{H}}(\boldsymbol{x}_t, t)^\intercal\nabla_{\boldsymbol{x}}\mu_{\boldsymbol{y}}(\boldsymbol{x}_t) \right)\beta_t\mathrm{d}t \\
&\quad - \left(\int_{\mathbb{R}^n} \left(U(\boldsymbol{x}, t) - \widehat{\boldsymbol{H}}(\boldsymbol{x}, t)^\intercal\nabla_{\boldsymbol{x}}\mu_{\boldsymbol{y}}(\boldsymbol{x}) \right)(P_\beta\gamma_t)(\boldsymbol{x})\mathrm{d}\boldsymbol{x} \right)\beta_t\mathrm{d}t,
\end{cases}
\tag{B.12}
$$

with initial condition $\boldsymbol{x}_0 = \boldsymbol{x}^*$ and $\beta_0 = 1$, where $\boldsymbol{x}^*$ is sampled from the initial posterior distribution $\widehat{q}_{\boldsymbol{y}}(\boldsymbol{x}, 0)$, $(\boldsymbol{w}_t)_{t \geq 0}$ is a standard Brownian motion in $\mathbb{R}^n$, $\gamma_t(\boldsymbol{x}, \beta)$ denotes the joint probability distribution of $(\boldsymbol{x}_t, \beta_t)$ on $\mathbb{R}^n \times \mathbb{R}$,

$$P_\beta \gamma_t(\boldsymbol{x}) := \int_{\mathbb{R}} \beta \gamma_t(\boldsymbol{x}, \beta) \mathrm{d}\beta$$

denotes the weighted projection of γ_t onto $\boldsymbol{x}$, and

$$U(\boldsymbol{x}, t) := \frac{1}{2} V(t)^2 \left(\|\nabla_{\boldsymbol{x}} \mu_{\boldsymbol{y}}(\boldsymbol{x})\|_2^2 - \Delta_{\boldsymbol{x}} \mu_{\boldsymbol{y}}(\boldsymbol{x}) \right).$$

Then we have that $P_\beta \gamma_t(\boldsymbol{x}) = \widehat{q}_{\boldsymbol{y}}(\boldsymbol{x}, t)$ for any $\boldsymbol{x} \in \mathbb{R}^n$ and $t \in [0, T]$, i.e. $P_\beta \gamma_t(\cdot)$ solves the following PDE:

$$\frac{\partial}{\partial t} \widehat{q}_{\boldsymbol{y}} = -\nabla_{\boldsymbol{x}} \cdot \left(\left(\widehat{\boldsymbol{H}}(\boldsymbol{x}, t) - V(t)^2 \nabla_{\boldsymbol{x}} \mu_{\boldsymbol{y}} \right) \widehat{q}_{\boldsymbol{y}} \right) + \frac{1}{2} V(t)^2 \Delta_x \widehat{q}_{\boldsymbol{y}}$$
$$+ \left(U(\boldsymbol{x}, t) - \widehat{\boldsymbol{H}}(\boldsymbol{x}, t)^{\mathsf{T}} \nabla_{\boldsymbol{x}} \mu_{\boldsymbol{y}} - \int_{\mathbb{R}^n} \left(U(\boldsymbol{x}, t) - \widehat{\boldsymbol{H}}(\boldsymbol{x}, t)^{\mathsf{T}} \nabla_{\boldsymbol{x}} \mu_{\boldsymbol{y}} \right) \widehat{q}_{\boldsymbol{y}} \mathrm{d}\boldsymbol{x} \right) \widehat{q}_{\boldsymbol{y}}. \tag{B.13}$$

The main idea is to derive the PDE governing the evolution of the joint distribution $\gamma_t(\boldsymbol{x}, \beta)$, which then leads to a PDE for its weighted projection $P_\beta \gamma_t(\boldsymbol{x})$. Our derivation here is mainly based on the theory of semigroups.

Definition B.5 (Semigroup Operator). *Given fixed time $s > 0$, consider a single particle $(\boldsymbol{x}_t, \beta_t)$ with initial condition $(\boldsymbol{x}_s, \beta_s) = (\boldsymbol{x}^*, \beta^*)$ for any $t > s$. Then the corresponding semigroup operator $\mathcal{T}_{s,t}^{(\boldsymbol{x}, \beta)}$ is defined via*

$$\mathcal{T}_{s,t}^{(\boldsymbol{x}, \beta)} \phi(\boldsymbol{x}^*, \beta^*) := \mathbb{E}\left[\phi(\boldsymbol{x}_t, \beta_t) \mid (\boldsymbol{x}_s, \beta_s) = (\boldsymbol{x}^*, \beta^*) \right], \tag{B.14}$$

where $\phi : \mathbb{R}^n \times \mathbb{R} \to \mathbb{R}$ above denotes an arbitrary test function. For the special case when $s = 0$, we write $\mathcal{T}_{0,t}^{(\boldsymbol{x}, \beta)} = \mathcal{T}_t^{(\boldsymbol{x}, \beta)}$.

Definition B.6 (Infinitesimal Generator). *Let $\mathbb{I}$ be the identity operator. Then for any fixed time $s > 0$ and suitable test function ϕ, the infinitesimal generator $\mathcal{L}_s^{(\boldsymbol{x}, \beta)}$ associated with the semigroup $\mathcal{T}_{s,t}^{(\boldsymbol{x}, \beta)}$ is defined by*

$$\mathcal{L}_s^{(\boldsymbol{x}, \beta)} \phi\left(\boldsymbol{x}^*, \beta^* \right) := \lim_{\Delta s \to 0^+} \frac{1}{\Delta s} \left(\mathcal{T}_{s, s + \Delta s}^{(\boldsymbol{x}, \beta)} \phi(\boldsymbol{x}^*, \beta^*) - \phi(\boldsymbol{x}^*, \beta^*) \right). \tag{B.15}$$

Moreover, for any test function $\phi : \mathbb{R}^n \times \mathbb{R} \to \mathbb{R}$ and input $(\boldsymbol{x}^*, \beta^*)$, we have

$$\mathcal{T}_{t_1 + t_2, t_1 + t_2 + t_3}^{(\boldsymbol{x}, \beta)} \circ \mathcal{T}_{t_1, t_1 + t_2}^{(\boldsymbol{x}, \beta)} \phi(\boldsymbol{x}^*, \beta^*) = \mathbb{E}\left[\phi(\boldsymbol{x}_{t_1 + t_2 + t_3}, \beta_{t_1 + t_2 + t_3}) \mid (\boldsymbol{x}_{t_1}, \beta_{t_1}) = (\boldsymbol{x}^*, \beta^*) \right]$$
$$= \mathcal{T}_{t_1, t_1 + t_2 + t_3}^{(\boldsymbol{x}, \beta)} \phi(\boldsymbol{x}^*, \beta^*) \tag{B.16}$$

demonstrating that $\mathcal{T}_{t_1 + t_2, t_1 + t_2 + t_3}^{(\boldsymbol{x}, \beta)} \circ \mathcal{T}_{t_1, t_1 + t_2}^{(\boldsymbol{x}, \beta)} = \mathcal{T}_{t_1, t_1 + t_2 + t_3}^{(\boldsymbol{x}, \beta)}$ for any time $t_1, t_2, t_3 > 0$.

Furthermore, combining (B.16) with the definition of the infinitesimal generator in (B.15), we can directly deduce the following equation for any time $0 < s < t$, input $(\boldsymbol{x}^*, \beta^*)$ and test function $\phi : \mathbb{R}^n \times \mathbb{R} \to \mathbb{R}$,

$$\frac{\partial}{\partial t} \mathcal{T}_{s,t}^{(\boldsymbol{x}, \beta)} \phi = \lim_{\Delta t \to 0^+} \frac{1}{\Delta t} \left(\mathcal{T}_{s, t + \Delta t}^{(\boldsymbol{x}, \beta)} - \mathcal{T}_{s,t}^{(\boldsymbol{x}, \beta)} \right) \phi\left(\boldsymbol{x}^*, \beta^* \right) = \lim_{\Delta t \to 0^+} \frac{1}{\Delta t} \mathcal{T}_{s,t}^{(\boldsymbol{x}, \beta)} \circ \left(\mathcal{T}_{t, t + \Delta t}^{(\boldsymbol{x}, \beta)} - \mathbb{I} \right) \phi\left(\boldsymbol{x}^*, \beta^* \right)$$
$$= \mathcal{T}_{s,t}^{(\boldsymbol{x}, \beta)} \circ \left(\lim_{\Delta t \to 0^+} \frac{1}{\Delta t} \left(\mathcal{T}_{t, t + \Delta t}^{(\boldsymbol{x}, \beta)} - \mathbb{I} \right) \right) \phi\left(\boldsymbol{x}^*, \beta^* \right) = \left(\mathcal{T}_{s,t}^{(\boldsymbol{x}, \beta)} \circ \mathcal{L}_t^{(\boldsymbol{x}, \beta)} \right) \phi\left(\boldsymbol{x}^*, \beta^* \right) \tag{B.17}$$

which is essentially the forward Kolgomorov equation expressed in terms of semigroups and infinitesimal generators. Moreover, for any $d \in \mathbb{Z}^+$ and two functions $\varphi^{(1)}, \varphi^{(2)} : \mathbb{R}^d \to \mathbb{R}$, we use

$$\left\langle \varphi^{(1)}, \varphi^{(2)} \right\rangle_{L^2(\mathbb{R}^d)} := \int_{\mathbb{R}^d} \varphi^{(1)}(\boldsymbol{x}) \varphi^{(2)}(\boldsymbol{x}) \mathrm{d}\boldsymbol{x}$$

to denote the inner product between $\varphi^{(1)}$ and $\varphi^{(2)}$. Should no confusion arise, we omit the subscript $L^2(\mathbb{R}^d)$ in the following.

Proposition B.7. *For any test function $\varphi : \mathbb{R}^n \times \mathbb{R} \to \mathbb{R}$, the joint distribution $\gamma_t = \gamma_t(\boldsymbol{x}, \beta)$ satisfies the following PDE:*

$$\frac{\partial}{\partial t}\gamma_t = -\nabla_{\boldsymbol{x}} \cdot (\boldsymbol{K}_t \gamma_t) - \frac{\partial}{\partial \beta}(b_t \gamma_t) + \frac{1}{2}V(t)^2 \Delta_{\boldsymbol{x}}\gamma_t, \tag{B.18}$$

with the initial condition $\gamma_0(\boldsymbol{x}, \beta) = \widehat{q}_{\boldsymbol{y}}(\boldsymbol{x}, 0) \times \delta_{\beta=1}$.

Proof. For any fixed time t and test function φ, integrating the function $\mathcal{T}_t^{(\boldsymbol{x},\beta)}\varphi$ over the initial joint distribution $\gamma_0(\boldsymbol{x}, \beta)$ yields

$$
\begin{aligned}
\left\langle \mathcal{T}_t^{(\boldsymbol{x},\beta)}\varphi, \gamma_0 \right\rangle &= \int_{\mathbb{R}^n \times \mathbb{R}} \mathcal{T}_t^{(\boldsymbol{x},\beta)}\varphi(\boldsymbol{x}^*, \beta^*)\gamma_0(\boldsymbol{x}^*, \beta^*)\, \mathrm{d}\boldsymbol{x}^* \mathrm{d}\beta^* \\
&= \int_{\mathbb{R}^n \times \mathbb{R}} \mathbb{E}\left[\varphi(\boldsymbol{x}_t, \beta_t) \mid (\boldsymbol{x}_0, \beta_0) = (\boldsymbol{x}^*, \beta^*)\right] \gamma_0(\boldsymbol{x}^*, \beta^*)\, \mathrm{d}\boldsymbol{x}^* \mathrm{d}\beta^* \\
&= \int_{\mathbb{R}^n \times \mathbb{R}} \varphi(\boldsymbol{x}^*, \beta^*)\gamma_t(\boldsymbol{x}^*, \beta^*)\mathrm{d}\boldsymbol{x}^* \mathrm{d}\beta^* = \langle \varphi, \gamma_t \rangle.
\end{aligned}
\tag{B.19}
$$

We integrate on both sides of (B.17) over the initial joint distribution $\gamma_0(\boldsymbol{x}, \beta)$ and plug in (B.19), which gives us that for any test function $\varphi : \mathbb{R}^n \times \mathbb{R} \to \mathbb{R}$,

$$
\begin{aligned}
\left\langle \varphi, \frac{\partial}{\partial t}\gamma_t \right\rangle &= \frac{\mathrm{d}}{\mathrm{d}t}\langle \varphi, \gamma_t \rangle = \frac{\mathrm{d}}{\mathrm{d}t}\left\langle \mathcal{T}_t^{(\boldsymbol{x},\beta)}\varphi, \gamma_0 \right\rangle = \left\langle \frac{\partial}{\partial t}\mathcal{T}_{0,t}^{(\boldsymbol{x},\beta)}\varphi, \gamma_0 \right\rangle \\
&= \left\langle \mathcal{T}_{0,t}^{(\boldsymbol{x},\beta)} \circ \mathcal{L}_t^{(\boldsymbol{x},\beta)}\varphi, \gamma_0 \right\rangle = \left\langle \mathcal{T}_t^{(\boldsymbol{x},\beta)} \circ \mathcal{L}_t^{(\boldsymbol{x},\beta)}\varphi, \gamma_0 \right\rangle = \left\langle \mathcal{L}_t^{(\boldsymbol{x},\beta)}\varphi, \gamma_t \right\rangle.
\end{aligned}
\tag{B.20}
$$

To further simplify the term on the RHS above, we need to compute the explicit form of the infinitesimal generator defined in (B.15). In fact, applying Itô's formula to the joint SDE (3.5) yields the following identity for any test function $\varphi : \mathbb{R}^n \times \mathbb{R} \to \mathbb{R}$,

$$\mathrm{d}\varphi(\boldsymbol{x}_t, \beta_t) = \left((\nabla_{\boldsymbol{x}}\varphi)^{\mathsf{T}} \boldsymbol{K}_t + \frac{\partial \varphi}{\partial \beta}b_t + \frac{1}{2}V(t)^2 \operatorname{Tr}\left(\nabla_{\boldsymbol{x}}^2 \varphi\right) \right)\mathrm{d}t + V(t)\left((\nabla_{\boldsymbol{x}}\varphi)^{\mathsf{T}} \mathrm{d}\boldsymbol{w}_t\right), \tag{B.21}$$

where $(\boldsymbol{w}_t)_{t \geq 0}$ is a standard Brownian motion on $\mathbb{R}^n$ and the two functions $\boldsymbol{K}_t : \mathbb{R}^d \to \mathbb{R}$ and $b_t : \mathbb{R}^d \times \mathbb{R} \to \mathbb{R}$ correspond to the drift terms in (3.5), *i.e.*,

$$
\begin{aligned}
\boldsymbol{K}_t(\boldsymbol{x}) &= \widehat{\boldsymbol{H}}(\boldsymbol{x}, t) - V(t)^2 \nabla_{\boldsymbol{x}}\mu_{\boldsymbol{y}}(\boldsymbol{x}), \\
b_t(\boldsymbol{x}, \beta) &= \left(U(\boldsymbol{x}, t) - \widehat{\boldsymbol{H}}(\boldsymbol{x}, t)^{\mathsf{T}}\nabla_{\boldsymbol{x}}\mu_{\boldsymbol{y}}(\boldsymbol{x}) \right)\beta \\
&\quad - \left(\int_{\mathbb{R}^n} \left(U(\boldsymbol{x}^*, t) - \widehat{\boldsymbol{H}}(\boldsymbol{x}^*, t)^{\mathsf{T}}\nabla_{\boldsymbol{x}}\mu_{\boldsymbol{y}}(\boldsymbol{x}^*) \right) (P_\beta \gamma_t)(\boldsymbol{x}^*)\mathrm{d}\boldsymbol{x}^* \right)\beta.
\end{aligned}
\tag{B.22}
$$

Taking expectation on both sides of (B.21) then yields the explicit expression of the infinitesimal generator for any test function $\varphi : \mathbb{R}^n \times \mathbb{R} \to \mathbb{R}$ as below:

$$\mathcal{L}_t^{(\boldsymbol{x},\beta)}\varphi = (\nabla_{\boldsymbol{x}}\varphi)^{\mathsf{T}} \boldsymbol{K}_t + \frac{\partial \varphi}{\partial \beta}b_t + \frac{1}{2}V(t)^2 \Delta_{\boldsymbol{x}}\varphi. \tag{B.23}$$

Below we use x_i and $\boldsymbol{K}_{t,i}$ to denote the i-th component of $\boldsymbol{x}$ and $\boldsymbol{K}_t$ for any $i \in [n]$. By substituting (B.23) into the RHS of (B.20), we obtain that for any test function $\varphi : \mathbb{R}^n \times \mathbb{R} \to \mathbb{R}$,

$$
\begin{aligned}
\left\langle \mathcal{L}_t^{(\boldsymbol{x},\beta)} \varphi, \gamma_t \right\rangle &= \left\langle (\nabla_{\boldsymbol{x}} \varphi)^{\intercal} \boldsymbol{K}_t + \frac{\partial \varphi}{\partial \beta} b_t + \frac{1}{2} V(t)^2 \Delta_{\boldsymbol{x}} \varphi, \gamma_t \right\rangle \\
&= \sum_{i=1}^n \left\langle \frac{\partial \varphi}{\partial x_i}, \boldsymbol{K}_{t,i} \gamma_t \right\rangle + \left\langle \frac{\partial \varphi}{\partial \beta}, b_t \gamma_t \right\rangle + \frac{1}{2} V(t)^2 \sum_{i=1}^n \left\langle \frac{\partial^2 \varphi}{\partial x_i^2}, \gamma_t \right\rangle \\
&= -\left\langle \varphi, \sum_{i=1}^n \frac{\partial}{\partial x_i} (\boldsymbol{K}_{t,i} \gamma_t) + \frac{\partial}{\partial \beta} (b_t \gamma_t) + \frac{1}{2} V(t)^2 \Delta_{\boldsymbol{x}} \gamma_t \right\rangle \\
&= \left\langle \varphi, -\nabla_{\boldsymbol{x}} \cdot (\boldsymbol{K}_t \gamma_t) - \frac{\partial}{\partial \beta} (b_t \gamma_t) + \frac{1}{2} V(t)^2 \Delta_{\boldsymbol{x}} \gamma_t \right\rangle,
\end{aligned}
\tag{B.24}
$$

where the second last equality above follows from integration by parts.

Substituting the last expression in (B.24) above into (B.20) then gives us the weak form of the PDE associated with the joint distribution γ_t in (B.18). $\qquad\square$

Proof of Lemma B.4. By defining

$$
\gamma_t^{\boldsymbol{P}}(\boldsymbol{x}) := P_\beta \gamma_t(\boldsymbol{x}) = \int_{\mathbb{R}} \beta \gamma_t(\boldsymbol{x}, \beta) \mathrm{d}\beta
$$

to be the weighted projection of γ_t, we then have that $\gamma_0^{\boldsymbol{P}}(\boldsymbol{x}) = \widehat{q}_{\boldsymbol{y}}(\boldsymbol{x}, 0)$. Below we proceed to derive the PDE govering the evolution of $\gamma_t^{\boldsymbol{P}}$ based on (B.18).

For any test function $\psi : \mathbb{R}^n \to \mathbb{R}$, taking $\varphi(\boldsymbol{x}, \beta) = \beta \psi(\boldsymbol{x}) : \mathbb{R}^n \times \mathbb{R} \to \mathbb{R}$ in the weak form derived in (B.20) and (B.24) yields

$$
\begin{aligned}
\left\langle \psi, \frac{\partial}{\partial t} \gamma_t^{\boldsymbol{P}} \right\rangle &= \frac{\mathrm{d}}{\mathrm{d}t} \left\langle \psi, \gamma_t^{\boldsymbol{P}} \right\rangle = \frac{\mathrm{d}}{\mathrm{d}t} \left(\int_{\mathbb{R}^n} \psi(\boldsymbol{x}) \left(\int_{\mathbb{R}} \beta \gamma_t(\boldsymbol{x}, \beta) \mathrm{d}\beta \right) \mathrm{d}\boldsymbol{x} \right) \\
&= \frac{\mathrm{d}}{\mathrm{d}t} \left\langle \varphi, \gamma_t \right\rangle = \left\langle \varphi, \frac{\partial}{\partial t} \gamma_t \right\rangle = \left\langle \varphi, -\nabla_{\boldsymbol{x}} \cdot (\boldsymbol{K}_t \gamma_t) - \frac{\partial}{\partial \beta} (b_t \gamma_t) + \frac{1}{2} V(t)^2 \Delta_{\boldsymbol{x}} \gamma_t \right\rangle \\
&= -\left\langle \varphi, \nabla_{\boldsymbol{x}} \cdot (\boldsymbol{K}_t \gamma_t) \right\rangle - \left\langle \varphi, \frac{\partial}{\partial \beta} (b_t \gamma_t) \right\rangle + \frac{1}{2} V(t)^2 \left\langle \varphi, \Delta_{\boldsymbol{x}} \gamma_t \right\rangle.
\end{aligned}
\tag{B.25}
$$

For the first and third terms in the last expression of (B.25), we can further simplify them as follows

$$
\begin{aligned}
\left\langle \varphi, \nabla_{\boldsymbol{x}} \cdot (\boldsymbol{K}_t \gamma_t) \right\rangle &= \int_{\mathbb{R}} \beta \left(\int_{\mathbb{R}^n} \psi(\boldsymbol{x}) \left(\nabla_{\boldsymbol{x}} \cdot (\boldsymbol{K}_t(\boldsymbol{x}) \gamma_t(\boldsymbol{x}, \beta)) \right) \mathrm{d}\boldsymbol{x} \right) \mathrm{d}\beta \\
&= \int_{\mathbb{R}^n} \psi(\boldsymbol{x}) \left(\nabla_{\boldsymbol{x}} \cdot \left(\boldsymbol{K}_t(\boldsymbol{x}) \left(\int_{\mathbb{R}} \beta \gamma_t(\boldsymbol{x}, \beta) \mathrm{d}\beta \right) \right) \right) \mathrm{d}\boldsymbol{x} \\
&= \int_{\mathbb{R}^n} \psi(\boldsymbol{x}) \left(\nabla_{\boldsymbol{x}} \cdot (\boldsymbol{K}_t(\boldsymbol{x}) \gamma_t^{\boldsymbol{P}}(\boldsymbol{x})) \right) \mathrm{d}\boldsymbol{x} \\
&= \left\langle \psi, \nabla_{\boldsymbol{x}} \cdot (\boldsymbol{K}_t \gamma_t^{\boldsymbol{P}}) \right\rangle
\end{aligned}
\tag{B.26}
$$

and

$$
\begin{aligned}
\left\langle \varphi, \Delta_{\boldsymbol{x}} \gamma_t \right\rangle &= \int_{\mathbb{R}} \beta \left(\int_{\mathbb{R}^n} \psi(\boldsymbol{x}) (\Delta_{\boldsymbol{x}} \gamma_t(\boldsymbol{x}, \beta)) \mathrm{d}\boldsymbol{x} \right) \mathrm{d}\beta \\
&= \int_{\mathbb{R}^n} \psi(\boldsymbol{x}) \left(\Delta_{\boldsymbol{x}} \left(\int_{\mathbb{R}} \beta \gamma_t(\boldsymbol{x}, \beta) \mathrm{d}\beta \right) \right) \mathrm{d}\boldsymbol{x} \\
&= \int_{\mathbb{R}^n} \psi(\boldsymbol{x}) \left(\Delta_{\boldsymbol{x}} \gamma_t^{\boldsymbol{P}} \right)(\boldsymbol{x}) \mathrm{d}\boldsymbol{x} = \left\langle \psi, \Delta_{\boldsymbol{x}} \gamma_t^{\boldsymbol{P}} \right\rangle,
\end{aligned}
\tag{B.27}
$$

respectively.

Moreover, for the second term in the last expression of (B.25), we use

$$\boldsymbol{J}_t(\boldsymbol{x}) := U(\boldsymbol{x}, t) - \widehat{\boldsymbol{H}}(\boldsymbol{x}, t)^\mathsf{T} \nabla_{\boldsymbol{x}} \mu_{\boldsymbol{y}}(\boldsymbol{x}) \tag{B.28}$$

to denote the integrand in the definition of b_t, which helps us rewrite b_t as follows

$$b_t(\boldsymbol{x}, \beta) = \left(\boldsymbol{J}_t(\boldsymbol{x}) - \int_{\mathbb{R}^n} \boldsymbol{J}_t(\boldsymbol{x}^*) \gamma_t^{\boldsymbol{P}}(\boldsymbol{x}^*) \mathrm{d}\boldsymbol{x}^* \right) \beta.$$

Then we apply integration by parts again to deduce that

$$
\begin{aligned}
\left\langle \varphi, \frac{\partial}{\partial \beta} (b_t \gamma_t) \right\rangle &= - \left\langle \frac{\partial}{\partial \beta} \varphi, b_t \gamma_t \right\rangle = - \left\langle \psi(\boldsymbol{x}), b_t \gamma_t \right\rangle \\
&= - \int_{\mathbb{R}} \psi(\boldsymbol{x}) \gamma_t(\boldsymbol{x}, \beta) \left(\boldsymbol{J}_t(\boldsymbol{x}) - \int_{\mathbb{R}^n} \boldsymbol{J}_t(\boldsymbol{x}^*) \gamma_t^{\boldsymbol{P}}(\boldsymbol{x}^*) \mathrm{d}\boldsymbol{x}^* \right) \beta \mathrm{d}\boldsymbol{x} \mathrm{d}\beta \\
&= - \int_{\mathbb{R}} \psi(\boldsymbol{x}) \gamma_t^{\boldsymbol{P}}(\boldsymbol{x}) \left(\boldsymbol{J}_t(\boldsymbol{x}) - \int_{\mathbb{R}^n} \boldsymbol{J}_t(\boldsymbol{x}^*) \gamma_t^{\boldsymbol{P}}(\boldsymbol{x}^*) \mathrm{d}\boldsymbol{x}^* \right) \mathrm{d}\boldsymbol{x} \\
&= - \left\langle \psi(\boldsymbol{x}), \gamma_t^{\boldsymbol{P}}(\boldsymbol{x}) \left(\boldsymbol{J}_t(\boldsymbol{x}) - \int_{\mathbb{R}^n} \boldsymbol{J}_t(\boldsymbol{x}^*) \gamma_t^{\boldsymbol{P}}(\boldsymbol{x}^*) \mathrm{d}\boldsymbol{x}^* \right) \right\rangle.
\end{aligned}
\tag{B.29}
$$

Substituting (B.26), (B.27), and (B.29) into (B.25) then gives us the weak form of the PDE governing the evolution of the projected measure $\gamma_t^{\boldsymbol{P}} = P_\beta \gamma_t$.

Hence, we finally have that $\gamma_t^{\boldsymbol{P}}(\boldsymbol{x}) = P_\beta \gamma_t(\boldsymbol{x})$ satisfies the following PDE

$$\frac{\partial}{\partial t} \gamma_t^{\boldsymbol{P}} = -\nabla_{\boldsymbol{x}} \cdot \left(\boldsymbol{K}_t \gamma_t^{\boldsymbol{P}} \right) + \frac{1}{2} V(t)^2 \Delta_{\boldsymbol{x}} \gamma_t^{\boldsymbol{P}} + \left(\boldsymbol{J}_t - \int_{\mathbb{R}^n} \boldsymbol{J}_t(\boldsymbol{x}^*) \gamma_t^{\boldsymbol{P}}(\boldsymbol{x}^*) \mathrm{d}\boldsymbol{x}^* \right) \gamma_t^{\boldsymbol{P}}, \tag{B.30}$$

with initial condition $\gamma_0^{\boldsymbol{P}}(\boldsymbol{x}) = \widehat{q}_{\boldsymbol{y}}(\boldsymbol{x}, 0)$.

Plugging in the expressions of $\boldsymbol{K}_t$ and $\boldsymbol{J}_t$ given in (B.22) and (B.28) indicates that equation (B.30) is exactly the PDE provided in (B.13). This concludes our proof. $\qquad\square$

Remark B.8 (Comparison with Concurrent Work (Skreta et al., 2025)). *We note that an alternative approach to derive the dynamics (3.5) for a weighted particle from the PDE (3.4) is to use the Feynman-Kac formula under the formulation of path integrals, as presented in the concurrent work (Skreta et al., 2025, Appendix A). Here we adopt the approach used for proving (Domingo-Enrich et al., 2020, Lemma 1 and 10), which is mainly based on the idea of lifting the projected measure to the joint measure and the weak form of PDE solutions.*

We adapt the FK Corrector dynamics from (Skreta et al., 2025, Proposition D.5) to provide a direct comparison with our dynamics of a weighted particle (derived from the PDE (3.4) and presented as (3.5)) for the setting of posterior sampling. This is achieved by setting the parameters in their notations as $\beta_t = 1$, the noise intensity $\sigma_t = V(t)^2$, and the reward function $r = -\mu_{\boldsymbol{y}}$. The resulting drift and reweighting terms for both methods are juxtaposed in Table 3.

It is noteworthy that if $V(t) = 0$ (i.e., in the absence of the diffusion-based corrector ϕ_θ and the gradient guidance $\nabla_{\boldsymbol{x}} \mu_{\boldsymbol{y}}$), both the AFDPS and the FK Corrector dynamics would simplify to the ODE dynamics, with their drift terms reducing to $-F(t)\boldsymbol{x}$. However, in the more general SDE case where $V(t) \neq 0$, the $-V(t)^2 \nabla_{\boldsymbol{x}} \mu_{\boldsymbol{y}}$ term in our AFDPS drift marks a critical difference. Our empirical results, detailed in Section 5, demonstrate that this specific term plays a vital role in effectively guiding the sampler towards regions of high likelihood, thereby enhancing performance.

In fact, by using $Q_{\boldsymbol{y}}(\boldsymbol{x}) := \breve{p}_t(\boldsymbol{x}) e^{-\mu_{\boldsymbol{y}}(\boldsymbol{x})}$ to denote the unnormalized posterior associated with the ground-truth backward SDE (2.4) with $G(t) = V(t)$, we can directly differentiate $Q_{\boldsymbol{y}}$ with respect to $\boldsymbol{x}$ to obtain that:

$$
\begin{aligned}
\nabla_{\boldsymbol{x}} Q_{\boldsymbol{y}} = \nabla_{\boldsymbol{x}} \left(\breve{p}_t e^{-\mu_{\boldsymbol{y}}} \right) &= \left(\nabla_{\boldsymbol{x}} \breve{p}_t \right) e^{-\mu_{\boldsymbol{y}}} - \breve{p}_t e^{-\mu_{\boldsymbol{y}}} \left(\nabla_{\boldsymbol{x}} \mu_{\boldsymbol{y}} \right) \\
&= \breve{p}_t e^{-\mu_{\boldsymbol{y}}} \left(\nabla_{\boldsymbol{x}} \log \breve{p}_t - \nabla_{\boldsymbol{x}} \mu_{\boldsymbol{y}} \right) = Q_{\boldsymbol{y}} \left(\nabla_{\boldsymbol{x}} \log \breve{p}_t - \nabla_{\boldsymbol{x}} \mu_{\boldsymbol{y}} \right)
\end{aligned}
\tag{B.31}
$$

Table 3: Drift and Reweighting Terms of AFDPS and FK Corrector

Term	AFDPS (Ours)	FK Corrector
Drift	$-F(t)\boldsymbol{x} + V(t)^2\boldsymbol{\phi}_\theta(\boldsymbol{x},t)$ $-V(t)^2\nabla_{\boldsymbol{x}}\mu_{\boldsymbol{y}}$	$-F(t)\boldsymbol{x} + V(t)^2\boldsymbol{\phi}_\theta(\boldsymbol{x},t)$
Reweighting	$\frac{1}{2}V(t)^2\left(\|\nabla_{\boldsymbol{x}}\mu_{\boldsymbol{y}}\|_2^2 - \Delta_{\boldsymbol{x}}\mu_{\boldsymbol{y}}\right)$ $+ \left(F(t)\boldsymbol{x} - V(t)^2\boldsymbol{\phi}_\theta(\boldsymbol{x},t)\right)^\intercal \nabla_{\boldsymbol{x}}\mu_{\boldsymbol{y}}$	$-\frac{1}{2}V(t)^2\left(\|\nabla_{\boldsymbol{x}}\mu_{\boldsymbol{y}}\|_2^2 - \Delta_{\boldsymbol{x}}\mu_{\boldsymbol{y}}\right)$ $+F(t)\boldsymbol{x}^\intercal\nabla_{\boldsymbol{x}}\mu_{\boldsymbol{y}}$

Moreover, a derivation similar to the proof of Lemma B.1 yields that the PDE dynamics governing the evolution of $Q_{\boldsymbol{y}}$ is given by

$$\frac{\partial}{\partial t}Q_{\boldsymbol{y}} = -\nabla_{\boldsymbol{x}} \cdot \left(\left(\boldsymbol{H}(\boldsymbol{x},t) - V(t)^2\nabla_{\boldsymbol{x}}\mu_{\boldsymbol{y}}\right)Q_{\boldsymbol{y}}\right) + \frac{1}{2}V(t)^2\Delta_x Q_{\boldsymbol{y}}$$
$$+ \left(\frac{1}{2}V(t)^2\left(\|\nabla_{\boldsymbol{x}}\mu_{\boldsymbol{y}}\|_2^2 - \Delta_{\boldsymbol{x}}\mu_{\boldsymbol{y}}\right) - \boldsymbol{H}(\boldsymbol{x},t)^\intercal\nabla_{\boldsymbol{x}}\mu_{\boldsymbol{y}}\right)Q_{\boldsymbol{y}} \tag{B.32}$$

where $\boldsymbol{H}(\boldsymbol{x},t) = -F(t)\boldsymbol{x} + V(t)^2\nabla_{\boldsymbol{x}}\log\breve{p}_t(\boldsymbol{x})$ is essentially obtained by replacing the neural network-based approximation $\boldsymbol{\phi}_\theta(\boldsymbol{x},t)$ in the expression of $\widehat{\boldsymbol{H}}(\boldsymbol{x},t)$ defined above with the true score function $\nabla_{\boldsymbol{x}}\log\breve{p}_t(\boldsymbol{x})$. For any fixed scalar $\eta \in \mathbb{R}$, we may further decompose the term $\nabla_{\boldsymbol{x}}\mu_{\boldsymbol{y}}$ above as the sum of $\eta\nabla_{\boldsymbol{x}}\mu_{\boldsymbol{y}}$ and $(1-\eta)\nabla_{\boldsymbol{x}}\mu_{\boldsymbol{y}}$ and directly simplify the RHS above as follows:

$$\frac{\partial}{\partial t}Q_{\boldsymbol{y}} = -\nabla_{\boldsymbol{x}} \cdot \left(\left(\boldsymbol{H}(\boldsymbol{x},t) - \eta V(t)^2\nabla_{\boldsymbol{x}}\mu_{\boldsymbol{y}}\right)Q_{\boldsymbol{y}}\right) + (1-\eta)V(t)^2\nabla_{\boldsymbol{x}} \cdot (Q_{\boldsymbol{y}}\nabla_{\boldsymbol{x}}\mu_{\boldsymbol{y}})$$
$$+ \frac{1}{2}V(t)^2\Delta_{\boldsymbol{x}}Q_{\boldsymbol{y}} + \left(\frac{1}{2}V(t)^2\left(\|\nabla_{\boldsymbol{x}}\mu_{\boldsymbol{y}}\|_2^2 - \Delta_{\boldsymbol{x}}\mu_{\boldsymbol{y}}\right) - \boldsymbol{H}(\boldsymbol{x},t)^\intercal\nabla_{\boldsymbol{x}}\mu_{\boldsymbol{y}}\right)Q_{\boldsymbol{y}}$$
$$= -\nabla_{\boldsymbol{x}} \cdot \left(\left(\boldsymbol{H}(\boldsymbol{x},t) - \eta V(t)^2\nabla_{\boldsymbol{x}}\mu_{\boldsymbol{y}}\right)Q_{\boldsymbol{y}}\right) + (1-\eta)V(t)^2\nabla_{\boldsymbol{x}}\mu_{\boldsymbol{y}}^\intercal\nabla_{\boldsymbol{x}}Q_{\boldsymbol{y}}$$
$$+ (1-\eta)V(t)^2 Q_{\boldsymbol{y}}\Delta_{\boldsymbol{x}}\mu_{\boldsymbol{y}} + \frac{1}{2}V(t)^2\Delta_{\boldsymbol{x}}Q_{\boldsymbol{y}}$$
$$+ \left(\frac{1}{2}V(t)^2\left(\|\nabla_{\boldsymbol{x}}\mu_{\boldsymbol{y}}\|_2^2 - \Delta_{\boldsymbol{x}}\mu_{\boldsymbol{y}}\right) - \boldsymbol{H}(\boldsymbol{x},t)^\intercal\nabla_{\boldsymbol{x}}\mu_{\boldsymbol{y}}\right)Q_{\boldsymbol{y}}$$
$$= -\nabla_{\boldsymbol{x}} \cdot \left(\left(\boldsymbol{H}(\boldsymbol{x},t) - \eta V(t)^2\nabla_{\boldsymbol{x}}\mu_{\boldsymbol{y}}\right)Q_{\boldsymbol{y}}\right) \tag{B.33}$$
$$+ (1-\eta)V(t)^2\nabla_{\boldsymbol{x}}\mu_{\boldsymbol{y}}^\intercal\left(\nabla_{\boldsymbol{x}}\log\breve{p}_t - \nabla_{\boldsymbol{x}}\mu_{\boldsymbol{y}}\right)Q_{\boldsymbol{y}} + \frac{1}{2}V(t)^2\Delta_{\boldsymbol{x}}Q_{\boldsymbol{y}}$$
$$+ \left(\frac{1}{2}V(t)^2\|\nabla_{\boldsymbol{x}}\mu_{\boldsymbol{y}}\|_2^2 + \left(\frac{1}{2} - \eta\right)V(t)^2\Delta_{\boldsymbol{x}}\mu_{\boldsymbol{y}} - \boldsymbol{H}(\boldsymbol{x},t)^\intercal\nabla_{\boldsymbol{x}}\mu_{\boldsymbol{y}}\right)Q_{\boldsymbol{y}}$$
$$= -\nabla_{\boldsymbol{x}} \cdot \left(\left(\boldsymbol{H}(\boldsymbol{x},t) - \eta V(t)^2\nabla_{\boldsymbol{x}}\mu_{\boldsymbol{y}}\right)Q_{\boldsymbol{y}}\right) + \frac{1}{2}V(t)^2\Delta_{\boldsymbol{x}}Q_{\boldsymbol{y}}$$
$$+ \left(\eta - \frac{1}{2}\right)V(t)^2\left(\|\nabla_{\boldsymbol{x}}\mu_{\boldsymbol{y}}\|_2^2 - \Delta_{\boldsymbol{x}}\mu_{\boldsymbol{y}}\right)Q_{\boldsymbol{y}}$$
$$+ \left(F(t)\boldsymbol{x} - \eta V(t)^2\nabla_{\boldsymbol{x}}\log\breve{p}_t(\boldsymbol{x})\right)^\intercal\nabla_{\boldsymbol{x}}\mu_{\boldsymbol{y}}Q_{\boldsymbol{y}}$$

where the second last equality above follows from plugging in (B.31).

By replacing the true score function $\nabla_{\boldsymbol{x}}\log\breve{p}_t(\boldsymbol{x})$ in the RHS above with the neural network-based estimator $\boldsymbol{\phi}_\theta(\boldsymbol{x},t)$, one then obtains the dynamics that can be used in practice. Specifically, for any fixed $\eta \in \mathbb{R}$, the drift term used in practice is given by

$$-F(t)\boldsymbol{x} + V(t)^2\boldsymbol{\phi}_\theta(\boldsymbol{x},t) - \eta V(t)^2\nabla_{\boldsymbol{x}}\mu_{\boldsymbol{y}}, \tag{B.34}$$

while the reweighting term used in practice is given by

$$\left(\eta - \frac{1}{2}\right)V(t)^2\left(\|\nabla_{\boldsymbol{x}}\mu_{\boldsymbol{y}}\|_2^2 - \Delta_{\boldsymbol{x}}\mu_{\boldsymbol{y}}\right) + \left(F(t)\boldsymbol{x} - \eta V(t)^2\boldsymbol{\phi}_\theta(\boldsymbol{x},t)\right)^\intercal\nabla_{\boldsymbol{x}}\mu_{\boldsymbol{y}} \tag{B.35}$$

By comparing the two terms above with Table 3, we note that $\eta = 0$ yields the FK Corrector dynamics while $\eta = 1$ yields the AFDPS dynamics. Therefore, for more difficult nonlinear inverse problems, we may control the magnitude of the term $V(t)^2 \nabla_{\boldsymbol{x}} \mu_{\boldsymbol{y}}$ by tuning the parameter η in practice. This also conforms to strategies used in existing practical work on guidance like (Dhariwal & Nichol, 2021; Ho & Salimans, 2022; Bansal et al., 2023; Song et al., 2023c; He et al., 2023; Guo et al., 2024; Ye et al., 2024). Finally, it would be of independent question to mathematically analyze how the discrepancy between the true dynamics (B.33) and the practical dynamics given by (B.34) and (B.35) depends on the parameter η in future work.

C Supplementary Proofs and Justifications for Section 4

In this section, we provide detailed proofs and justifications for claims listed in Section 4.

C.1 Proof of Theorem 4.1

We begin by listing two commonly used results as two lemmas below. Specifically, the first lemma below provides a quantitative bound on the discrepancy between two diffusion processes with different drift functions, while the second lemma describes the convergence of the forward process towards the target distribution when Gaussian noise is added.

Lemma C.1. *For any pair of diffusion processes $(\boldsymbol{x}_t)_{t \in [0,T]}$ and $(\widetilde{\boldsymbol{x}}_t)_{t \in [0,T]}$ on $\mathbb{R}^n$ defined as follows*

$$
\begin{aligned}
\mathrm{d}\boldsymbol{x}_t &= \boldsymbol{b}(\boldsymbol{x}_t, t)\mathrm{d}t + c(t)\mathrm{d}\boldsymbol{w}_t \\
and \quad \mathrm{d}\widetilde{\boldsymbol{x}}_t &= \widetilde{\boldsymbol{b}}(\widetilde{\boldsymbol{x}}_t, t)\mathrm{d}t + c(t)\mathrm{d}\boldsymbol{w}_t
\end{aligned}
\tag{C.1}
$$

where $\boldsymbol{b}, \widetilde{\boldsymbol{b}} : \mathbb{R}^n \times [0,T] \to \mathbb{R}^n$ are the two drift functions, $c : [0,T] \to \mathbb{R}^+$ and $(\boldsymbol{w}_t)_{t \in [0,T]}$ is a standard Brownian motion. Let ρ_t and $\widetilde{\rho}_t$ denote the distribution of $\boldsymbol{x}_t$ and $\widetilde{\boldsymbol{x}}_t$ respectively for any $t \in [0,T]$, then we have

$$
D_{\mathrm{KL}}(\rho_T \| \widetilde{\rho}_T) \le D_{\mathrm{KL}}(\rho_0 \| \widetilde{\rho}_0) + \int_0^T \int_{\mathbb{R}^n} \frac{1}{2c(t)^2} \left\| \boldsymbol{b}(\boldsymbol{x}, t) - \widetilde{\boldsymbol{b}}(\boldsymbol{x}, t) \right\|_2^2 \rho_t(\boldsymbol{x})\mathrm{d}\boldsymbol{x}\mathrm{d}t.
\tag{C.2}
$$

Proof. We remark that the proof of this lemma is essentially the same as the derivations in many previous works on the theoretical analysis of DMs and variants. Examples include, but are not limited to, (Chen et al., 2023a, Lemma C.1), (Albergo et al., 2023b, Lemma 2.22), and (Wu et al., 2024c, Lemma A.4). For the sake of completeness, we include a detailed derivation here.

The main idea is to use the Fokker-Planck equations associated with the diffusion processes in (C.1) and differentiate the KL divergence between the two evolving densities with respect to time. Specifically, we have that ρ_t and $\widetilde{\rho}_t$ satisfy the following Fokker-Planck equations:

$$
\begin{aligned}
\frac{\partial}{\partial t}\rho_t &= -\nabla_{\boldsymbol{x}} \cdot (\boldsymbol{b}(\boldsymbol{x}, t)\rho_t) + \frac{1}{2}c(t)^2 \Delta_{\boldsymbol{x}}\rho_t, \\
and \quad \frac{\partial}{\partial t}\widetilde{\rho}_t &= -\nabla_{\boldsymbol{x}} \cdot \left(\widetilde{\boldsymbol{b}}(\boldsymbol{x}, t)\widetilde{\rho}_t\right) + \frac{1}{2}c(t)^2 \Delta_{\boldsymbol{x}}\widetilde{\rho}_t.
\end{aligned}
\tag{C.3}
$$

From the definition of the KL divergence

$$
D_{\mathrm{KL}}(\rho_t \| \widetilde{\rho}_t) = \int_{\mathbb{R}^n} \log \frac{\rho_t(\boldsymbol{x})}{\widetilde{\rho}_t(\boldsymbol{x})} \rho_t(\boldsymbol{x})\mathrm{d}\boldsymbol{x},
$$

we can differentiate it with respect to the time variable t, which yields

$$
\begin{aligned}
\frac{\mathrm{d}}{\mathrm{d}t}D_{\mathrm{KL}}(\rho_t \| \widetilde{\rho}_t) &= \int_{\mathbb{R}^n} \log \frac{\rho_t}{\widetilde{\rho}_t} \frac{\partial \rho_t}{\partial t}\mathrm{d}\boldsymbol{x} + \int_{\mathbb{R}^n} \left(\frac{\partial}{\partial t}\log \rho_t - \frac{\partial}{\partial t}\log \widetilde{\rho}_t \right) \rho_t \mathrm{d}\boldsymbol{x} \\
&= \int_{\mathbb{R}^n} \log \frac{\rho_t}{\widetilde{\rho}_t} \frac{\partial \rho_t}{\partial t}\mathrm{d}\boldsymbol{x} + \int_{\mathbb{R}^n} \left(\frac{1}{\rho_t}\frac{\partial \rho_t}{\partial t} - \frac{1}{\widetilde{\rho}_t}\frac{\partial \widetilde{\rho}_t}{\partial t} \right) \rho_t \mathrm{d}\boldsymbol{x} \\
&= \int_{\mathbb{R}^n} \log \frac{\rho_t}{\widetilde{\rho}_t} \frac{\partial \rho_t}{\partial t}\mathrm{d}\boldsymbol{x} - \int_{\mathbb{R}^n} \frac{\rho_t}{\widetilde{\rho}_t}\frac{\partial \widetilde{\rho}_t}{\partial t}\mathrm{d}\boldsymbol{x}
\end{aligned}
\tag{C.4}
$$

For the first term in (C.4) above, we plug in (C.3) and use integration by parts, which yields

$$
\int_{\mathbb{R}^n} \log \frac{\rho_t}{\widetilde{\rho}_t} \frac{\partial \rho_t}{\partial t} \mathrm{d}\boldsymbol{x}
$$

$$
= -\int_{\mathbb{R}^n} (\log \rho_t - \log \widetilde{\rho}_t) \nabla_{\boldsymbol{x}} \cdot \left(\left(\boldsymbol{b} - \frac{c(t)^2}{2} \nabla_{\boldsymbol{x}} \log \rho_t \right) \rho_t \right) \mathrm{d}\boldsymbol{x} \tag{C.5}
$$

$$
= \int_{\mathbb{R}^n} (\nabla_{\boldsymbol{x}} \log \rho_t - \nabla_{\boldsymbol{x}} \log \widetilde{\rho}_t)^{\mathsf{T}} \left(\boldsymbol{b} - \frac{c(t)^2}{2} \nabla_{\boldsymbol{x}} \log \rho_t \right) \rho_t \mathrm{d}\boldsymbol{x}.
$$

To simplify the second term in (C.4), we plug in (C.3) apply integration by parts again to obtain that

$$
-\int_{\mathbb{R}^n} \frac{\rho_t}{\widetilde{\rho}_t} \frac{\partial \widetilde{\rho}_t}{\partial t} \mathrm{d}\boldsymbol{x} = \int_{\mathbb{R}^n} \frac{\rho_t}{\widetilde{\rho}_t} \nabla_{\boldsymbol{x}} \cdot \left(\left(\widetilde{\boldsymbol{b}} - \frac{c(t)^2}{2} \nabla_{\boldsymbol{x}} \log \widetilde{\rho}_t \right) \widetilde{\rho}_t \right) \mathrm{d}\boldsymbol{x}
$$

$$
= \int_{\mathbb{R}^n} \left[\nabla_{\boldsymbol{x}} \cdot \left(\widetilde{\boldsymbol{b}} - \frac{c(t)^2}{2} \nabla_{\boldsymbol{x}} \log \widetilde{\rho}_t \right) \rho_t + \left(\widetilde{\boldsymbol{b}} - \frac{c(t)^2}{2} \nabla_{\boldsymbol{x}} \log \widetilde{\rho}_t \right)^{\mathsf{T}} \frac{\nabla_{\boldsymbol{x}} \widetilde{\rho}_t}{\widetilde{\rho}_t} \rho_t \right] \mathrm{d}\boldsymbol{x} \tag{C.6}
$$

$$
= \int_{\mathbb{R}^n} \left(\widetilde{\boldsymbol{b}} - \frac{c(t)^2}{2} \nabla_{\boldsymbol{x}} \log \widetilde{\rho}_t \right)^{\mathsf{T}} (\nabla_{\boldsymbol{x}} \log \widetilde{\rho}_t - \nabla_{\boldsymbol{x}} \log \rho_t) \rho_t \mathrm{d}\boldsymbol{x}
$$

Furthermore, substituting and into then yields

$$
\frac{\mathrm{d}}{\mathrm{d}t} D_{\mathrm{KL}}(\rho_t \| \widetilde{\rho}_t) = \int_{\mathbb{R}^n} (\nabla_{\boldsymbol{x}} \log \rho_t - \nabla_{\boldsymbol{x}} \log \widetilde{\rho}_t)^{\mathsf{T}} \left(\boldsymbol{b} - \frac{c(t)^2}{2} \nabla_{\boldsymbol{x}} \log \rho_t \right) \rho_t \mathrm{d}\boldsymbol{x}
$$

$$
+ \int_{\mathbb{R}^n} (\nabla_{\boldsymbol{x}} \log \widetilde{\rho}_t - \nabla_{\boldsymbol{x}} \log \rho_t)^{\mathsf{T}} \left(\widetilde{\boldsymbol{b}} - \frac{c(t)^2}{2} \nabla_{\boldsymbol{x}} \log \widetilde{\rho}_t \right) \rho_t \mathrm{d}\boldsymbol{x}
$$

$$
= -\frac{c(t)^2}{2} \int_{\mathbb{R}^n} \| \nabla_{\boldsymbol{x}} \log \widetilde{\rho}_t - \nabla_{\boldsymbol{x}} \log \rho_t \|_2^2 \rho_t \mathrm{d}\boldsymbol{x} \tag{C.7}
$$

$$
+ \int_{\mathbb{R}^n} \left(\boldsymbol{b} - \widetilde{\boldsymbol{b}} \right)^{\mathsf{T}} (\nabla_{\boldsymbol{x}} \log \rho_t - \nabla_{\boldsymbol{x}} \log \widetilde{\rho}_t) \rho_t \mathrm{d}\boldsymbol{x}
$$

$$
\leq \frac{1}{2c(t)^2} \int_{\mathbb{R}^n} \left\| \boldsymbol{b} - \widetilde{\boldsymbol{b}} \right\|_2^2 \rho_t \mathrm{d}\boldsymbol{x} = \frac{1}{2c(t)^2} \int_{\mathbb{R}^n} \left\| \boldsymbol{b}(\boldsymbol{x}, t) - \widetilde{\boldsymbol{b}}(\boldsymbol{x}, t) \right\|_2^2 \rho_t(\boldsymbol{x}) \mathrm{d}\boldsymbol{x}
$$

where the last inequality follows from the AM-GM inequality, *i.e.* $\boldsymbol{x}^{\mathsf{T}}\boldsymbol{y} \leq \frac{1}{2c(t)^2} \|\boldsymbol{x}\|_2^2 + \frac{c(t)^2}{2} \|\boldsymbol{y}\|_2^2$ for any vectors $\boldsymbol{x}, \boldsymbol{y} \in \mathbb{R}^n$ and $t \in [0, T]$.

Integrating (C.7) from $t = 0$ to $t = T$ then yields (C.2), which concludes our proof. $\qquad\square$

Lemma C.2. *For any distribution p on $\mathbb{R}^n$ with bounded second moment m_2^2, i.e., $\mathbb{E}_{\boldsymbol{x} \sim p}[\|\boldsymbol{x}\|_2^2] \leq m_2^2$, we have $D_{\mathrm{KL}}\left(p * \mathcal{N}(\boldsymbol{0}, \sigma^2 \boldsymbol{I}_n) \| \mathcal{N}(\boldsymbol{0}, \sigma^2 \boldsymbol{I}_n)\right) \leq \frac{m_2^2}{2\sigma^2}$, where $(p * q)(\boldsymbol{x}) := \int_{\mathbb{R}^n} p(\boldsymbol{y}) q(\boldsymbol{x} - \boldsymbol{y}) \mathrm{d}\boldsymbol{y}$ denotes the convolution of the two probability distributions p, q.*

Proof. We remark that this is the same as (Wang et al., 2024, Lemma 10), where a complete proof is already provided. $\qquad\square$

With Lemma C.1 and Lemma C.2 listed above, we then prove Theorem 4.1.

Proof of Theorem 4.1. Consider the backward process associated with the true score function under the EDM framework, which can be formally written as

$$
\mathrm{d}\breve{\boldsymbol{x}}_t = \left[-\frac{\dot{s}(t)}{s(t)} \breve{\boldsymbol{x}}_t + 2s(t)^2 \dot{\sigma}(t)\sigma(t) \nabla \log \breve{p}_t(\breve{\boldsymbol{x}}_t) \right] \mathrm{d}t + s(t)\sqrt{2\dot{\sigma}(t)\sigma(t)} \mathrm{d}\boldsymbol{w}_t. \tag{C.8}
$$

with initial condition

$$
\breve{\boldsymbol{x}}_0 \sim \breve{p}_0 = p_T = p_0 * \mathcal{N}(\boldsymbol{0}, T^2 \boldsymbol{I}_n),
$$

where the last identity follows from results derived in Appendix B.1 in the paper (Karras et al., 2022) that proposes the EDM framework as well as our particular choices of the scaling functions $s(t) = 1$ and $\sigma(t) = t$.

Then we consider applying Lemma C.1 to compare the two diffusion processes $(\overleftarrow{x}_t)_{t \in [0,T]}$ and $(\widehat{\overleftarrow{x}}_t)_{t \in [0,T]}$ defined in (C.8) and (2.5) respectively.

By setting $c(t) = s(t)\sqrt{2\dot{\sigma}(t)\sigma(t)} = \sqrt{2}t$,

$$\boldsymbol{b}(\boldsymbol{x}, t) = -\frac{\dot{s}(t)}{s(t)}\boldsymbol{x} + 2s(t)^2\dot{\sigma}(t)\sigma(t)\nabla \log \overleftarrow{p}_t(\boldsymbol{x}) = 2t\nabla \log \overleftarrow{p}_t(\boldsymbol{x})$$

and

$$\widetilde{\boldsymbol{b}}(\boldsymbol{x}, t) = -\frac{\dot{s}(t)}{s(t)}\boldsymbol{x} + 2s(t)^2\dot{\sigma}(t)\sigma(t)\boldsymbol{\phi}_\theta(\boldsymbol{x}, t) = 2t\boldsymbol{\phi}_\theta(\boldsymbol{x}, t),$$

we have

$$
\begin{aligned}
D_{\mathrm{KL}}(p_0\|\widehat{\overleftarrow{p}}_T) &= D_{\mathrm{KL}}(\overleftarrow{p}_T\|\widehat{\overleftarrow{p}}_T) \\
&\le D_{\mathrm{KL}}(\overleftarrow{p}_0\|\widehat{\overleftarrow{p}}_0) + \int_0^T \int_{\mathbb{R}^n} \frac{1}{4t}\left\|2t\left(\boldsymbol{\phi}_\theta(\boldsymbol{x}, t) - \nabla_{\boldsymbol{x}}\log \overleftarrow{p}_t(\boldsymbol{x})\right)\right\|_2^2 \overleftarrow{p}_t(\boldsymbol{x})\mathrm{d}\boldsymbol{x}\mathrm{d}t \\
&= D_{\mathrm{KL}}\left(p_0 * \mathcal{N}(\boldsymbol{0}, T^2\boldsymbol{I}_n)\|\mathcal{N}(\boldsymbol{0}, T^2\boldsymbol{I}_n)\right) \\
&\quad + \int_0^T \int_{\mathbb{R}^n} t\left\|\boldsymbol{\phi}_\theta(\boldsymbol{x}, t) - \nabla_{\boldsymbol{x}}\log \overleftarrow{p}_t(\boldsymbol{x})\right\|_2^2 \overleftarrow{p}_t(\boldsymbol{x})\mathrm{d}\boldsymbol{x}\mathrm{d}t \le \frac{m_2^2}{2T^2} + \frac{1}{2}T^2\epsilon_{\boldsymbol{s}}^2,
\end{aligned}
\tag{C.9}
$$

where the second lest inequality above follows from Lemma C.1 and the last inequality follows from Assumption 4.2, Assumption 4.3 and Lemma C.2.

Applying Pinsker's inequality helps us further bound the TV divergence between p_0 and $\widehat{\overleftarrow{p}}_T$ as follows

$$\mathrm{TV}\left(\widehat{\overleftarrow{p}}_T, p_0\right) = \mathrm{TV}\left(p_0, \widehat{\overleftarrow{p}}_T\right) \le \sqrt{\frac{1}{2}D_{\mathrm{KL}}(p_0\|\widehat{\overleftarrow{p}}_T)} \le \frac{1}{2}\sqrt{\frac{m_2^2}{T^2} + T^2\epsilon_{\boldsymbol{s}}^2}. \tag{C.10}$$

Based on the bounds on the distance between the two prior distributions above, we proceed to bound the distance between the two associated posterior distributions.

Since

$$\widehat{q}_{\boldsymbol{y}, T}(\boldsymbol{x}) \propto \widehat{\overleftarrow{p}}_T(\boldsymbol{x})e^{-\mu_{\boldsymbol{y}}(\boldsymbol{x})} \quad \text{and} \quad q_{\boldsymbol{y}, 0}(\boldsymbol{x}) \propto p_0(x)e^{-\mu_{\boldsymbol{y}}(\boldsymbol{x})},$$

we use

$$\widehat{Z}(\boldsymbol{y}) := \int_{\mathbb{R}^n} \widehat{\overleftarrow{p}}_T(\boldsymbol{x})e^{-\mu_{\boldsymbol{y}}(\boldsymbol{x})}\mathrm{d}\boldsymbol{x} \quad \text{and} \quad Z(\boldsymbol{y}) := \int_{\mathbb{R}^n} p_0(x)e^{-\mu_{\boldsymbol{y}}(\boldsymbol{x})}\mathrm{d}\boldsymbol{x}$$

to denote the two corresponding normalizing constants. Then we have

$$\left|\widehat{Z}(\boldsymbol{y}) - Z(\boldsymbol{y})\right| = \left|\int_{\mathbb{R}^n} e^{-\mu_{\boldsymbol{y}}(\boldsymbol{x})}\left(\widehat{\overleftarrow{p}}_T(\boldsymbol{x}) - p_0(\boldsymbol{x})\right)\mathrm{d}\boldsymbol{x}\right| \le 2e^{-C_{\boldsymbol{y}}^{(1)}}\mathrm{TV}\left(\widehat{\overleftarrow{p}}_T, p_0\right) \tag{C.11}$$

where the inequality above follows from Assumption 4.1. Then we can use the bound on the difference between the normalizing constants above to deduce that further

$$
\begin{aligned}
\mathrm{TV}(\widehat{q}_{\boldsymbol{y},T}, q_{\boldsymbol{y},0}) &= \frac{1}{2} \int_{\mathbb{R}^n} \left| \frac{1}{\widehat{Z}(\boldsymbol{y})} \widehat{\widetilde{p}}_T(\boldsymbol{x}) e^{-\mu_{\boldsymbol{y}}(\boldsymbol{x})} - \frac{1}{Z(\boldsymbol{y})} p_0(\boldsymbol{x}) e^{-\mu_{\boldsymbol{y}}(\boldsymbol{x})} \right| \mathrm{d}\boldsymbol{x} \\
&\le \frac{1}{2} \int_{\mathbb{R}^n} \left| \frac{1}{\widehat{Z}(\boldsymbol{y})} \widehat{\widetilde{p}}_T(\boldsymbol{x}) e^{-\mu_{\boldsymbol{y}}(\boldsymbol{x})} - \frac{1}{Z(\boldsymbol{y})} \widehat{\widetilde{p}}_T(\boldsymbol{x}) e^{-\mu_{\boldsymbol{y}}(\boldsymbol{x})} \right| \mathrm{d}\boldsymbol{x} \\
&\quad + \frac{1}{2} \int_{\mathbb{R}^n} \left| \frac{1}{Z(\boldsymbol{y})} \widehat{\widetilde{p}}_T(\boldsymbol{x}) e^{-\mu_{\boldsymbol{y}}(\boldsymbol{x})} - \frac{1}{Z(\boldsymbol{y})} p_0(\boldsymbol{x}) e^{-\mu_{\boldsymbol{y}}(\boldsymbol{x})} \right| \mathrm{d}\boldsymbol{x} \\
&= \frac{|Z(\boldsymbol{y}) - \widehat{Z}(\boldsymbol{y})|}{2 Z(\boldsymbol{y}) \widehat{Z}(\boldsymbol{y})} \left(\int_{\mathbb{R}^n} \widehat{\widetilde{p}}_T(\boldsymbol{x}) e^{-\mu_{\boldsymbol{y}}(\boldsymbol{x})} \mathrm{d}\boldsymbol{x} \right) \\
&\quad + \frac{1}{2 Z(\boldsymbol{y})} \left| \int_{\mathbb{R}^n} e^{-\mu_{\boldsymbol{y}}(\boldsymbol{x})} \left(\widehat{\widetilde{p}}_T(\boldsymbol{x}) - p_0(\boldsymbol{x}) \right) \mathrm{d}\boldsymbol{x} \right| \\
&\le \frac{1}{2 Z(\boldsymbol{y})} \left(\left| \widehat{Z}(\boldsymbol{y}) - Z(\boldsymbol{y}) \right| + 2 e^{-C_{\boldsymbol{y}}^{(1)}} \mathrm{TV}\left(\widehat{\widetilde{p}}_T, p_0 \right) \right) \\
&\le \frac{2 e^{-C_{\boldsymbol{y}}^{(1)}}}{Z(\boldsymbol{y})} \mathrm{TV}\left(\widehat{\widetilde{p}}_T, p_0 \right) \le \frac{e^{-C_{\boldsymbol{y}}^{(1)}}}{Z(\boldsymbol{y})} \sqrt{\frac{m_2^2}{T^2} + T^2 \epsilon_{\boldsymbol{s}}^2},
\end{aligned}
$$

where the first inequality above follows from triangle inequality, the second inequality above follows from Assumption 4.1, the third inequality follows from (C.11) and the last inequality above follows from (C.10).

By setting

$$
C_{\boldsymbol{y}}^{(2)} := \frac{e^{-C_{\boldsymbol{y}}^{(1)}}}{Z(\boldsymbol{y})}
$$

in the last expression above, which is some constant that only depends on $\boldsymbol{y}$, we conclude our proof of Theorem 4.1.

Moreover, balancing the two terms in the last expression above also yields $\frac{m_2^2}{T^2} = T^2 \epsilon_{\boldsymbol{s}}^2$, $i.e.$, $T = \sqrt{\frac{m_2}{\epsilon_s}}$ gives us the optimal upper bound

$$
\mathrm{TV}(\widehat{q}_{\boldsymbol{y},T}, q_{\boldsymbol{y},0}) \le C_{\boldsymbol{y}}^{(2)} \sqrt{m_2 \epsilon_{\boldsymbol{s}}},
$$

which is proportional to the square root of the score matching error defined in Assumption 4.3. $\qquad\square$

C.2 Proof of Theorem 4.2

Our proof of Theorem 4.2 is mainly based on arguments from propagation of chaos (Sznitman, 1991; Lacker, 2018).

Recall that

$$
\gamma_\tau^N(\boldsymbol{x}, \beta) = \frac{1}{N} \sum_{i=1}^N \delta_{(\boldsymbol{x}_\tau^{(i)}, \beta_\tau^{(i)})}
$$

denotes the joint measured formed by the N weighted particles $\left\{ \left(\boldsymbol{x}_\tau^{(i)}, \beta_\tau^{(i)} \right) \right\}_{i=1}^N$ given by (3.6) and γ_τ is the joint probability distribution of the single weighted particle $(\boldsymbol{x}_\tau, \beta_\tau)$ satisfying (3.5).

Now we consider an auxiliary system of N weighted particles $\{(\widetilde{\boldsymbol{x}}_t^{(i)}, \widetilde{\beta}_t^{(i)})\}_{i=1}^N$ sampled identically and independently from the single particle dynamics (3.5), $i.e.$,

$$
\begin{cases}
\mathrm{d}\widetilde{\boldsymbol{x}}_t^{(i)} &= \left(\widehat{\boldsymbol{H}}(\widetilde{\boldsymbol{x}}_t^{(i)}, t) - V(t)^2 \nabla_{\boldsymbol{x}} \mu_{\boldsymbol{y}}(\widetilde{\boldsymbol{x}}_t^{(i)}) \right) \mathrm{d}t + V(t) \mathrm{d}\boldsymbol{w}_t^{(i)}, \\
\mathrm{d}\widetilde{\beta}_t^{(i)} &= \left(U(\widetilde{\boldsymbol{x}}_t^{(i)}, t) - \widehat{\boldsymbol{H}}(\widetilde{\boldsymbol{x}}_t^{(i)}, t)^\intercal \nabla_{\boldsymbol{x}} \mu_{\boldsymbol{y}}(\widetilde{\boldsymbol{x}}_t^{(i)}) \right) \widetilde{\beta}_t^{(i)} \mathrm{d}t \\
&\quad - \left(\int_{\mathbb{R}^n} \left(U(\boldsymbol{x}, t) - \widehat{\boldsymbol{H}}(\boldsymbol{x}, t)^\intercal \nabla_{\boldsymbol{x}} \mu_{\boldsymbol{y}}(\boldsymbol{x}) \right) (P_\beta \gamma_t)(\boldsymbol{x}) \mathrm{d}\boldsymbol{x} \right) \widetilde{\beta}_t^{(i)} \mathrm{d}t.
\end{cases} \tag{C.12}
$$

We note that the initial conditions of (C.12) are given by $\widetilde{\boldsymbol{x}}_0^{(i)} = \boldsymbol{x}_0^{(i)} \sim \widehat{q}_{\boldsymbol{y}}(\cdot, 0)$ and $\widetilde{\beta}_0^{(i)} = 1$ for $i \in [N]$. Moreover, we have that the $\left(\boldsymbol{w}_t^{(i)}\right)_{t \in [0,T]}$ is the same standard Brownian motion used in (3.6) for any $i \in [N]$, which implies $\boldsymbol{x}_t^{(i)} \equiv \widetilde{\boldsymbol{x}}_t^{(i)}$ for any $i \in [N]$ and $t \in [0,T]$. Then we consider the joint empirical measure

$$\widetilde{\gamma}_t^N(\boldsymbol{x}, \beta) = \frac{1}{N} \sum_{i=1}^N \delta_{\left(\widetilde{\boldsymbol{x}}_t^{(i)}, \widetilde{\beta}_t^{(i)}\right)} \tag{C.13}$$

formed by the N weighted particles $\left\{\left(\widetilde{\boldsymbol{x}}_t^{(i)}, \widetilde{\beta}_t^{(i)}\right)\right\}_{i=1}^N$ given by (C.12).

Before we proceed, we establish the following upper bound:

Lemma C.3. *The following upper bound on the absolute values of the weights holds for any $t \in [0,T]$*

$$\max_{i \in [N]} \left\{ |\beta_t|, \left|\beta_t^{(i)}\right|, \left|\widetilde{\beta}_t^{(i)}\right| \right\} \leq \exp\left(B_{\boldsymbol{y}} t^2\right). \tag{C.14}$$

Proof. Below we will only prove the upper bound in (C.14) above for the weight $\widetilde{\beta}_t^{(i)}$ governed by (C.12), as the same upper bound for $\beta_t^{(i)}$ governed by (3.6) and β_t governed by (3.5) can be proved via the same procedure.

By integrating from 0 to t on both sides of (C.12) and applying the bound on I provided in the statement of Theorem 4.2, we have that

$$\begin{aligned}
\left|\widetilde{\beta}_t^{(i)}\right| &\leq \left|\int_0^t \left(U\left(\widetilde{\boldsymbol{x}}_\tau^{(i)}, \tau\right) - \widehat{\boldsymbol{H}}\left(\widetilde{\boldsymbol{x}}_\tau^{(i)}, \tau\right)^\intercal \nabla_{\boldsymbol{x}} \mu_{\boldsymbol{y}}\left(\widetilde{\boldsymbol{x}}_\tau^{(i)}\right)\right) \widetilde{\beta}_\tau^{(i)} \mathrm{d}\tau\right| + \widetilde{\beta}_0^{(i)} \\
&\quad + \left|\int_0^t \left(\int_{\mathbb{R}^n} \left(U(\boldsymbol{x}, \tau) - \widehat{\boldsymbol{H}}(\boldsymbol{x}, \tau)^\intercal \nabla_{\boldsymbol{x}} \mu_{\boldsymbol{y}}(\boldsymbol{x})\right) (P_\beta \gamma_\tau)(\boldsymbol{x}) \mathrm{d}\boldsymbol{x}\right) \widetilde{\beta}_\tau^{(i)} \mathrm{d}\tau\right| \\
&\leq \int_0^t \left|\tau I\left(\widetilde{\boldsymbol{x}}_\tau^{(i)}, \tau\right) \widetilde{\beta}_\tau^{(i)}\right| \mathrm{d}\tau + \int_0^t \left|\tau \left(\int_{\mathbb{R}^n} I(\boldsymbol{x}, \tau)(P_\beta \gamma_\tau)(\boldsymbol{x}) \mathrm{d}\boldsymbol{x}\right) \widetilde{\beta}_\tau^{(i)}\right| \mathrm{d}\tau + 1 \\
&\leq 2 \int_0^t B_{\boldsymbol{y}} \tau \left|\widetilde{\beta}_\tau^{(i)}\right| \mathrm{d}\tau + 1,
\end{aligned} \tag{C.15}$$

where the last inequality above follows from the assumed upper bound on I and Lemma B.4, which shows that the weighted projection $P_\beta \gamma_t$ is a probability measure on $\mathbb{R}^n$ for any $t \in [0,T]$. Applying Gronwall's inequality to (C.15) then yields the upper bound in (C.14), as desired. $\qquad\square$

Proof of Theorem 4.2. By recalling the definition of the Wasserstein-2 distance as follows

$$\mathcal{W}_2^2(\mu, \nu) := \inf_{\Gamma \in \Pi(\mu, \nu)} \left(\int_{\mathbb{R}^d \times \mathbb{R}^d} \|\boldsymbol{x} - \boldsymbol{y}\|_2^2 \Gamma(\boldsymbol{x}, \boldsymbol{y}) \mathrm{d}\boldsymbol{x} \mathrm{d}\boldsymbol{y}\right), \tag{C.16}$$

where $\Pi(\mu, \nu)$ denotes the set of couplings between any two distributions μ, ν on $\mathbb{R}^d$ for fixed d, we can apply triangle inequality

$$\|a + b\|_2^2 \leq 2\left(\|a\|_2^2 + \|b\|_2^2\right),$$

and take expectation on both sides to deduce that for any fixed $t \in [0,T]$ and $\tau \in [0,t]$, the following inequality

$$\mathbb{E}\left[\mathcal{W}_2^2(\gamma_\tau^N, \gamma_\tau)\right] \leq 2\mathbb{E}\left[\mathcal{W}_2^2(\gamma_\tau^N, \widetilde{\gamma}_\tau^N)\right] + 2\mathbb{E}\left[\mathcal{W}_2^2(\widetilde{\gamma}_\tau^N, \gamma_\tau)\right] \tag{C.17}$$

holds for any N.

Taking supremum with respect to $\tau \in [0,t]$ on both sides above then yields

$$\sup_{\tau \in [0,t]} \mathbb{E}\left[\mathcal{W}_2^2(\gamma_\tau^N, \gamma_\tau)\right] \leq 2 \sup_{\tau \in [0,t]} \mathbb{E}\left[\mathcal{W}_2^2(\gamma_\tau^N, \widetilde{\gamma}_\tau^N)\right] + 2 \sup_{\tau \in [0,t]} \mathbb{E}\left[\mathcal{W}_2^2(\widetilde{\gamma}_\tau^N, \gamma_\tau)\right]. \tag{C.18}$$

We then need to bound the two terms on the RHS of (C.17).

For the first term in (C.17), we note that the empirical measure

$$\frac{1}{N} \sum_{i=1}^{N} \delta_{(\boldsymbol{x}_\tau^{(i)}, \beta_\tau^{(i)}), (\widetilde{\boldsymbol{x}}_\tau^{(i)}, \widetilde{\beta}_\tau^{(i)})}$$

defined on $\mathbb{R}^{n+1} \times \mathbb{R}^{n+1}$ is a coupling between γ_τ^N and $\widetilde{\gamma}_\tau^N$ for any time $\tau \in [0, t]$. Setting Γ in (C.13) to be such a coupling then gives us the following upper bound on the expected Wasserstein-2 distance:

$$
\begin{aligned}
\sup_{\tau \in [0,t]} \mathbb{E}\left[\mathcal{W}_2^2(\gamma_\tau^N, \widetilde{\gamma}_\tau^N)\right] &\leq \sup_{\tau \in [0,t]} \left(\frac{1}{N} \sum_{i=1}^{N} \mathbb{E}\left[\left\|\boldsymbol{x}_t^{(i)} - \widetilde{\boldsymbol{x}}_t^{(i)}\right\|_2^2 + \left|\beta_t^{(i)} - \widetilde{\beta}_t^{(i)}\right|^2\right]\right) \\
&= \frac{1}{N} \sum_{i=1}^{N} \sup_{\tau \in [0,t]} \mathbb{E}\left[\left|\beta_t^{(i)} - \widetilde{\beta}_t^{(i)}\right|^2\right].
\end{aligned}
\tag{C.19}
$$

where the equality above follows from the observation $\boldsymbol{x}_t^{(i)} \equiv \widetilde{\boldsymbol{x}}_t^{(i)}$ for any $i \in [N]$ and $t \in [0, T]$.

Below, we use
$$L(\boldsymbol{x}, t) := U(\boldsymbol{x}, t) - \widehat{\boldsymbol{H}}(\boldsymbol{x}, t)^\intercal \nabla_{\boldsymbol{x}} \mu_{\boldsymbol{y}}(\boldsymbol{x})$$
to denote the drift function appearing in the dynamics (3.6) and (C.12). By plugging in the choices $s(t) = 1, \sigma(t) = t$ stated in Theorem 4.2, we then have

$$L = U - \widehat{\boldsymbol{H}}^\intercal \nabla_{\boldsymbol{x}} \mu_{\boldsymbol{y}} = t\left(\|\nabla_{\boldsymbol{x}} \mu_{\boldsymbol{y}}\|_2^2 - \Delta_{\boldsymbol{x}} \mu_{\boldsymbol{y}}\right) - 2t\phi_\theta^\intercal \left(\nabla_{\boldsymbol{x}} \mu_{\boldsymbol{y}}\right) = tI, \tag{C.20}$$

where $I = I(\boldsymbol{x}, t)$ is defined in the statement of Theorem 4.2.

Now we return to bound the RHS of (C.19). By taking the difference between the two dynamics (3.6) and (C.12) and applying triangle inequality, we then plug in $\widetilde{\boldsymbol{x}}_t^{(i)} \equiv \boldsymbol{x}_t^{(i)}$ to obtain the following decomposed upper bound for any $\tau' \in [0, \tau]$ with fixed $\tau \in [0, t]$ and $i \in [N]$:

$$
\begin{aligned}
\left|\frac{\mathrm{d}}{\mathrm{d}\tau'} \beta_{\tau'}^{(i)} - \frac{\mathrm{d}}{\mathrm{d}\tau'} \widetilde{\beta}_{\tau'}^{(i)}\right| &\leq \left|L\left(\boldsymbol{x}_{\tau'}^{(i)}, \tau'\right)\left(\beta_{\tau'}^{(i)} - \widetilde{\beta}_{\tau'}^{(i)}\right)\right| \\
&\quad + \left|\left(\int_{\mathbb{R}^n} L\left(\boldsymbol{x}, \tau'\right)(P_\beta \gamma_{\tau'})(\boldsymbol{x})\mathrm{d}\boldsymbol{x}\right)\left(\beta_{\tau'}^{(i)} - \widetilde{\beta}_{\tau'}^{(i)}\right)\right| \\
&\quad + \left|\int_{\mathbb{R}^{n+1}} \beta L\left(\boldsymbol{x}, \tau'\right)\left(\gamma_{\tau'}^N(\boldsymbol{x}, \beta) - \gamma_{\tau'}(\boldsymbol{x}, \beta)\right)\mathrm{d}\boldsymbol{x}\mathrm{d}\beta\right|\left|\beta_{\tau'}^{(i)}\right| \\
&\leq 2B_{\boldsymbol{y}} \tau' \left|\beta_{\tau'}^{(i)} - \widetilde{\beta}_{\tau'}^{(i)}\right| \\
&\quad + \left|\int_{\mathbb{R}^{n+1}} \beta I\left(\boldsymbol{x}, \tau'\right)\left(\gamma_{\tau'}^N(\boldsymbol{x}, \beta) - \gamma_{\tau'}(\boldsymbol{x}, \beta)\right)\mathrm{d}\boldsymbol{x}\mathrm{d}\beta\right|\tau' \exp\left(B_{\boldsymbol{y}} \tau'^2\right),
\end{aligned}
\tag{C.21}
$$

where the last inequality above follows from (C.14) and assumed upper bound on the function $I = \frac{1}{t}L$.

Furthermore, we recall the following property of the Wasserstein distances $\mathcal{W}_1$ and $\mathcal{W}_2$:

$$\mathcal{W}_1(\mu, \nu) := \sup_{g:\mathbb{R}^n \to \mathbb{R}, \ \mathrm{Lip}(g) \leq 1} \int_{\mathbb{R}^n} g(\boldsymbol{x})(\mu(\boldsymbol{x}) - \nu(\boldsymbol{x}))\mathrm{d}\boldsymbol{x} \leq \mathcal{W}_2(\mu, \nu). \tag{C.22}$$

From the assumed upper bound on $\mathrm{Lip}(I)$ given in Theorem 4.2, we have $\mathrm{Lip}\left(\frac{1}{B_{\boldsymbol{y}}} I\right) \leq 1$. Setting

$$g(\boldsymbol{x}, \beta) := \frac{\beta I(\boldsymbol{x}, \tau')}{e^{B_{\boldsymbol{y}} \tau'^2} B_{\boldsymbol{y}}},$$

$\mu := \gamma_{\tau'}^N$, and $\nu := \gamma_{\tau'}$ in (C.22) above for any $\tau' \in [0, \tau]$ then implies

$$\left| \int_{\mathbb{R}^n} \beta I\left(\boldsymbol{x}, \tau'\right) \left(\gamma_{\tau'}^N(\boldsymbol{x}, \beta) - \gamma_{\tau'}(\boldsymbol{x}, \beta)\right) \mathrm{d}\boldsymbol{x}\mathrm{d}\beta \right| \leq B_{\boldsymbol{y}} e^{B_{\boldsymbol{y}}\tau'^2} \mathcal{W}_1\left(\gamma_{\tau'}^N, \gamma_{\tau'}\right)$$
$$\leq B_{\boldsymbol{y}} e^{B_{\boldsymbol{y}}\tau'^2} \mathcal{W}_2\left(\gamma_{\tau'}^N, \gamma_{\tau'}\right). \tag{C.23}$$

Substituting (C.23) into (C.21), squaring on both sides and applying AM-GM inequality indicate that for any $\tau' \in [0, \tau]$ and $i \in [N]$:

$$\left| \frac{\mathrm{d}}{\mathrm{d}\tau'} \beta_{\tau'}^{(i)} - \frac{\mathrm{d}}{\mathrm{d}\tau'} \widetilde{\beta}_{\tau'}^{(i)} \right|^2 \leq \left(2B_{\boldsymbol{y}}\tau' \left| \beta_{\tau'}^{(i)} - \widetilde{\beta}_{\tau'}^{(i)} \right| + B_{\boldsymbol{y}}\tau' \exp\left(2B_{\boldsymbol{y}}\tau'^2\right) \mathcal{W}_2\left(\gamma_{\tau'}^N, \gamma_{\tau'}\right) \right)^2$$
$$\leq 8B_{\boldsymbol{y}}^2\tau'^2 \left| \beta_{\tau'}^{(i)} - \widetilde{\beta}_{\tau'}^{(i)} \right|^2 + 2B_{\boldsymbol{y}}^2\tau'^2 \exp\left(4B_{\boldsymbol{y}}\tau'^2\right) \mathcal{W}_2^2\left(\gamma_{\tau'}^N, \gamma_{\tau'}\right). \tag{C.24}$$

Integrating from $\tau' = 0$ to $\tau' = \tau$ on both sides above and applying Cauchy-Schwarz inequality imply that for any $\tau \in [0, t]$ and $i \in [N]$:

$$\left| \beta_\tau^{(i)} - \widetilde{\beta}_\tau^{(i)} \right|^2 = \left| \int_0^\tau \left(\frac{\mathrm{d}}{\mathrm{d}\tau'} \beta_{\tau'}^{(i)} - \frac{\mathrm{d}}{\mathrm{d}\tau'} \widetilde{\beta}_{\tau'}^{(i)} \right) \mathrm{d}\tau' \right|^2 \leq \tau \left(\int_0^\tau \left| \frac{\mathrm{d}}{\mathrm{d}\tau'} \beta_{\tau'}^{(i)} - \frac{\mathrm{d}}{\mathrm{d}\tau'} \widetilde{\beta}_{\tau'}^{(i)} \right|^2 \mathrm{d}\tau' \right)$$
$$\leq 8B_{\boldsymbol{y}}^2\tau \int_0^\tau \tau'^2 \left| \beta_{\tau'}^{(i)} - \widetilde{\beta}_{\tau'}^{(i)} \right|^2 \mathrm{d}\tau' \tag{C.25}$$
$$+ 2\tau \int_0^\tau B_{\boldsymbol{y}}^2\tau'^2 \exp\left(4B_{\boldsymbol{y}}\tau'^2\right) \mathcal{W}_2^2\left(\gamma_{\tau'}^N, \gamma_{\tau'}\right) \mathrm{d}\tau'.$$

Applying Gronwall's inequality to the function $\frac{1}{\tau'} \left| \beta_{\tau'}^{(i)} - \widetilde{\beta}_{\tau'}^{(i)} \right|^2$ in (C.25) above then yields

$$\frac{1}{\tau} \left| \beta_\tau^{(i)} - \widetilde{\beta}_\tau^{(i)} \right|^2 \leq 2 \left(\int_0^\tau B_{\boldsymbol{y}}^2\tau'^2 \exp\left(4B_{\boldsymbol{y}}\tau'^2\right) \mathcal{W}_2^2\left(\gamma_{\tau'}^N, \gamma_{\tau'}\right) \mathrm{d}\tau' \right) e^{\int_0^\tau 8B_{\boldsymbol{y}}^2\tau'^3 \mathrm{d}\tau'}. \tag{C.26}$$

Then we multiply τ and take the expectation on both sides of (C.26). A direct application of Fubini's Theorem then indicates that for any $i \in [N]$ and $\tau \in [0, t]$:

$$\mathbb{E}\left[\left| \beta_\tau^{(i)} - \widetilde{\beta}_\tau^{(i)} \right|^2 \right] \leq 2\tau e^{2B_{\boldsymbol{y}}^2\tau^4} \int_0^\tau B_{\boldsymbol{y}}^2\tau'^2 \exp\left(4B_{\boldsymbol{y}}\tau'^2\right) \mathbb{E}\left[\mathcal{W}_2^2\left(\gamma_{\tau'}^N, \gamma_{\tau'}\right) \right] \mathrm{d}\tau'$$
$$\leq 2B_{\boldsymbol{y}}^2\tau^3 e^{2B_{\boldsymbol{y}}^2\tau^4 + 4B_{\boldsymbol{y}}\tau^2} \int_0^\tau \sup_{\tau'' \in [0, \tau']} \mathbb{E}\left[\mathcal{W}_2^2\left(\gamma_{\tau''}^N, \gamma_{\tau''}\right) \right] \mathrm{d}\tau'. \tag{C.27}$$

Taking supremum with respect to $\tau \in [0, t]$ on both sides of (C.27) further implies

$$\sup_{\tau \in [0, t]} \mathbb{E}\left[\left| \beta_\tau^{(i)} - \widetilde{\beta}_\tau^{(i)} \right|^2 \right] \leq 2B_{\boldsymbol{y}}^2 t^3 e^{2B_{\boldsymbol{y}}^2 t^4 + 4B_{\boldsymbol{y}} t^2} \int_0^t \sup_{\tau' \in [0, \tau]} \mathbb{E}\left[\mathcal{W}_2^2\left(\gamma_{\tau'}^N, \gamma_{\tau'}\right) \right] \mathrm{d}\tau, \tag{C.28}$$

for any $i \in [N]$ and $t \in [0, T]$.

Substituting (C.28) above into (C.19) and then (C.18) indicates

$$\sup_{\tau \in [0, t]} \mathbb{E}\left[\mathcal{W}_2^2(\gamma_\tau^N, \gamma_\tau) \right] \leq 4B_{\boldsymbol{y}}^2 t^3 e^{2B_{\boldsymbol{y}}^2 t^4 + 4B_{\boldsymbol{y}} t^2} \int_0^t \sup_{\tau' \in [0, \tau]} \mathbb{E}\left[\mathcal{W}_2^2\left(\gamma_{\tau'}^N, \gamma_{\tau'}\right) \right] \mathrm{d}\tau$$
$$+ 2 \sup_{\tau \in [0, t]} \mathbb{E}\left[\mathcal{W}_2^2(\widetilde{\gamma}_\tau^N, \gamma_\tau) \right]$$
$$\leq \int_0^t 4B_{\boldsymbol{y}}^2 T^3 e^{2B_{\boldsymbol{y}}^2 T^4 + 4B_{\boldsymbol{y}} T^2} \sup_{\tau' \in [0, \tau]} \mathbb{E}\left[\mathcal{W}_2^2\left(\gamma_{\tau'}^N, \gamma_{\tau'}\right) \right] \mathrm{d}\tau$$
$$+ 2 \sup_{\tau \in [0, t]} \mathbb{E}\left[\mathcal{W}_2^2(\widetilde{\gamma}_\tau^N, \gamma_\tau) \right], \tag{C.29}$$

for any $t \in [0, T]$.

Applying Gronwall's inequality again to the function $\sup_{\tau \in [0,t]} \mathbb{E}\left[\mathcal{W}_2^2(\gamma_\tau^N, \gamma_\tau)\right]$ further implies that

$$\sup_{\tau \in [0,t]} \mathbb{E}\left[\mathcal{W}_2^2(\gamma_\tau^N, \gamma_\tau)\right] \leq 2 \exp\left(4B_{\boldsymbol{y}}^2 T^4 e^{2B_{\boldsymbol{y}}^2 T^4 + 4B_{\boldsymbol{y}} T^2}\right) \sup_{\tau \in [0,t]} \mathbb{E}\left[\mathcal{W}_2^2(\widetilde{\gamma}_\tau^N, \gamma_\tau)\right] \tag{C.30}$$

for any $t \in [0, T]$.

By setting $t = T$ in (C.30) above and taking the limit $N \to \infty$, we then have

$$\lim_{N \to \infty} \mathbb{E}\left[\mathcal{W}_2^2(\gamma_\tau^N, \gamma_\tau)\right] = \lim_{N \to \infty} \mathbb{E}\left[\mathcal{W}_2^2(\widetilde{\gamma}_\tau^N, \gamma_\tau)\right] = 0,$$

for any $\tau \in [0, T]$ with T fixed, where the last equality above follows from Lemma B.4 and the law of large numbers (See, for instance, (Lacker, 2018, Corollary 2.14)). This concludes our proof. $\qquad\square$

Remark C.4. *We note that one may also adopt similar arguments used in (Domingo-Enrich et al., 2020) to prove existence and uniqueness of solutions to the SDE systems (3.6) and (3.5). In fact, such type of mean field analysis based on arguments from propogation of chaos have been widely adopted for studying different types of PDEs arising from subfields of not only physical sciences but also data sciences, such as fluid dynamics (Goodman et al., 1990), kinetic theory (Carrillo & Vaes, 2021; Borghi & Pareschi, 2025), theory of two layer neural networks (Mei et al., 2019; Hu et al., 2021), ensemble-based sampling and variational inference (Lu et al., 2019a; Kelly et al., 2014; Schillings & Stuart, 2017; 2018; Ding & Li, 2021a;b). For some good reference on related mathematical models, one may refer to (Muntean et al., 2016). Therefore, it would be of independent interest to investigate whether we can develop more refined mathematical theory for the two sampling algorithms proposed in this paper by combining perspectives from gradient flows or numerical analysis. Moreover, it would also be interesting to investigate how existing mathematical theory (Eberle & Marinelli, 2006; Schweizer, 2012; Eberle & Marinelli, 2013; Beskos et al., 2014b;a; 2016; Giraud & Del Moral, 2017) developed for SMC can be applied to analyze Algorithm 2 and Algorithm 4 that we proposed here.*

D   Additional Implementation Details

D.1   Datasets, model checkpoints and inverse problem setups

Data usage   We mainly test our methods and the baseline methods on the FFHQ-256 (Karras et al., 2019) dataset and the ImageNet-256 (Deng et al., 2009) dataset. All images used for the tests in this paper are in RGB. For FFHQ-256, the 100 testing images were selected to be the first 100 images in the dataset, whoses indexes range from 00000 to 00099. For ImageNet-256, the 100 testing images were selected to be the first 100 images in the ImageNet-1k validation set. However, when we further test only the two algorithms AFDPS-SDE and AFDPS-ODE proposed in this paper and exhibit their performance in Appendix E, we have enlarged the testing dataset to be the whole FFHQ-dataset and ImageNet 1k-validation dataset.

Model checkpoints   The two pretrained score functions for the FFHQ-256 and the ImageNet-256 datasets used in this paper were directly taken from the ones used in (Chung et al., 2022), which are available in the following Google Drive [1]. However, since these checkpoints were all trained based on the DDPM formulation (Ho et al., 2020), we adpoted the same transformation used in (Wu et al., 2024c) to convert the pretrained score function from the DDPM formulation to the EDM formulation (Karras et al., 2022). One may refer to the "Preconditioning" subsection in Appendix C.2 of (Wu et al., 2024c) for an explicit formula of the transformation deployed here.

Inverse problem setups   Below we provide a discussion on the mathematical formulations of the four inverse problems we tested on here.

---

[1]Pretrained score functions used in (Chung et al., 2022)

Super-resolution The forward model in (2.1) associated with the super-resolution problem we test on here can be written as

$$\boldsymbol{y} = P_f \boldsymbol{x} + \boldsymbol{n}$$

where $P_f \in \mathbb{R}^{\frac{n}{f} \times n}$ implements a block averaging filter that downscales each image by a factor of f and $\boldsymbol{n} \sim \mathcal{N}(\boldsymbol{0}, 0.2\boldsymbol{I}_{\frac{n}{f}})$. Using similar setups as many previous work (Chung et al., 2022; Kawar et al., 2022; Wu et al., 2024c) on solving inverse problems via diffusion models, here we pick $f = 4$.

Gaussian and motion deblurring The forward model associated with any deblurring problem can be summarized as

$$\boldsymbol{y} = B_k \boldsymbol{x} + \boldsymbol{n}$$

where $\boldsymbol{n} \sim \mathcal{N}(\boldsymbol{0}, 0.2\boldsymbol{I}_n)$ and $B_k \in \mathbb{R}^{n \times n}$ is a circulant matrix that realizes a convolution with the kernel k under circular boundary condition. Again, we adopt the same settings used in most previous work (Chung et al., 2022; Kawar et al., 2022; Wu et al., 2024c).

Specifically, for the Gaussian deblurring problem, the convolutional kernel k is fixed to be a Gaussian kernel of standard deviation 3.0 and size 61×61. For the motion deblurring problem, the kernel k is randomly generated via code used in previous work (Kawar et al., 2022; Wu et al., 2024c), where the size is chosen to be 61×61 and the intensity is set to be 0.5. In order to ensure a fair comparison, we use the same motion kernel k for each image across different methods.

Box inpainting The forward model for the box inpainting problem is given by

$$\boldsymbol{y} = D\boldsymbol{x} + \boldsymbol{n}$$

where $\boldsymbol{n} \sim \mathcal{N}(\boldsymbol{0}, 0.2\boldsymbol{I}_n)$ and D is a diagonal matrix with either 0 or 1 on its diagonal. In particular, here we choose D such that a centered square patch of size 64×64 (i.e., the side length is a quarter of the original image's side length) is masked out.

D.2 Implementation details of AFDPS and all baseline methods

Regarding computing resources, all experiments included in this paper were conducted on NVIDIA RTX A100 and A6000 GPUs. A major part of the code implementing Algorithm 2 and 4 in this paper were adapted from the following Github repository[2]. Specifically, we used the same numerical discretization as that of the EDM framework (Karras et al., 2019), which is also deployed in (Wu et al., 2024c). One major difference is that we had tuned the terminal time to be $T = 8$ for both AFDPS-SDE (Alg. 2) and AFDPS-ODE (Alg. 4), while T is set to be 80 for both the SGS-EDM method (Wu et al., 2024c) and the original EDM framework (Karras et al., 2022). Moreover, we increased the number of discretized timesteps as our methods avoids running multiple backward diffusion processes for different iterations. Specifically, for AFDPS-SDE the number particles and discretized timesteps were set to be 10 and 2000, respectively. For the AFDPS-ODE method, in order to control the total number of evaluations (NFEs), we set the number of particles, discretized timesteps and number of corrector steps at each time to be 5, 1000 and 4, respectively. Moreover, for both AFDPS-SDE (Algorithm 2) and AFDPS-ODE (Algorithm 4), we save computational cost by skipping the resampling step specified in Algorithm 1 in our implementation, which allows us to implement the dynamics of the particles' positions and weights in a parallel way. Finally, we return the particle associated with the largest weight as our best estimator of the recovered image. Given that we already take the logarithm of the weights in both AFDPS-SDE and AFDPS-ODE, they are guaranteed to remain numerically stable as time increases.

Here we further elaborate on the implementation details associated with the baseline methods. One thing to note is that two extra baselines are included in the extended numerical results presented in Tables 1 and 2 above. The following list provides an extended summary of these baselines and how we choose the parameters:

- *DPS (Chung et al., 2022)*: a method that performs posterior sampling by guiding the reverse diffusion process with manifold-constrained gradients derived from the measurement likelihood, enabling efficient

---

[2]Source code for (Wu et al., 2024c)

inference in general noisy (non)linear inverse problems. We adopt most parameters usedin the default setting. The only difference is that we increase the number of discretized timesteps from 1000 to 1500, which helps make the method more tolerant of problems with higher observational noises

- *DCDP (Li et al., 2024b)*: a framework that alternates between data-consistent reconstruction and diffusion-based purification, which decouples data fidelity and prior sampling to improve flexibility and performance in image restoration tasks. In order to make the DCDP method adaptive to problems with higher observational noise, we change their settings by picking the number of iterations involved in both the data-reconstruction step and the diffusion-based purification step to be 100. Regarding the learning rates used for the data-reconstruction step, we have tuned them to yield the best possible performance. Specifically, the learning rates for the Gaussian deblurring, box inpainting, motion deblurring and super-resolution problems were set to be $10, 7, 10$ and 3, respectively.
- *SGS-EDM (Wu et al., 2024c)*: a method that couples a split Gibbs sampler with a diffusion model, interpreting posterior inference as alternating between likelihood-based updates and Gaussian denoising via a learned generative prior. For the SGS-EDM method, we adopt the default setting used in (Wu et al., 2024c).
- *FK-Corrector (Skreta et al., 2025)*: a method that uses the Feynman-Kac formula to design corrector steps within a sequential Monte Carlo framework, improving the accuracy of samples from forward diffusion trajectories. We use the same set of parameters deployed in the AFDPS-SDE method by setting the number of particles and discretized timesteps to be 10 and 2000 as well, which ensures a fair comparison.
- *PF-SMC-DM (Dou & Song, 2024)*: a framework that formulates posterior sampling as a particle filtering problem, combining sequential Monte Carlo with diffusion models for efficient inference in high-dimensional spaces. Again, to ensure a fair comparison, we increase the number of particles and discretized timesteps to be 10 and 2000 for PF-SMC-DM as well.

E   Additional Experimental Results and Discussions

In this section, we provide additional experimental results and detailed qualitative comparisons between our proposed methods and existing baselines.

Summary.   Across the diverse inverse problems evaluated on FFHQ-256 and ImageNet-256 (detailed in Table 1 and Table 2), the AFDPS framework consistently delivers strong results. The AFDPS-SDE variant, in particular, frequently distinguishes itself by producing visually compelling outcomes, excelling in the generation of sharp details and fine textures that contribute to high perceptual quality. This is evident in Figures 3-6, where AFDPS-SDE's reconstructions often appear more intricate and realistic. The AFDPS-ODE variant also provides coherent results, which are typically characterized by a notable smoothness. For tasks where capturing the utmost detail and textural accuracy is paramount, AFDPS-SDE often provides a particularly effective solution, frequently leading in or strongly competing for the best perceptual metrics (LPIPS).

Gaussian Deblurring.   In Gaussian deblurring, AFDPS-SDE showcases its ability to produce perceptually rich outputs, achieving the best LPIPS on ImageNet-256 (0.3925) and a competitive LPIPS on FFHQ-256 (0.2580). Figure 3 highlights SDE's strength in rendering sharp, defined textures like the dog's fur (ImageNet, row 2). Concurrently, AFDPS-ODE achieves high PSNR on both datasets and the best LPIPS on FFHQ-256 (24.98 PSNR, 0.2560 LPIPS), delivering notably clean and smooth outputs, for example, on the baby's facial skin (FFHQ, row 2).

Motion Deblurring.   For motion deblurring, AFDPS-SDE demonstrates strong perceptual quality, securing the best LPIPS score (0.2869) on FFHQ-256, while PF-SMC-DM leads in PSNR. Figure 4 emphasizes SDE's proficiency in transforming blurred images into sharp, detailed reconstructions, meticulously recovering fine details like individual hair strands in FFHQ portraits (e.g., row 5). AFDPS-ODE also effectively removes blur, yielding coherent results, typically with a characteristically smoother finish.

Super-Resolution.   AFDPS-SDE stands out in super-resolution, achieving the best PSNR and LPIPS scores on both FFHQ-256 (22.96 PSNR, 0.3063 LPIPS) and ImageNet-256 (20.97 PSNR, 0.4643 LPIPS).

Figure 5 compellingly shows SDE generating sharp, highly detailed images from severely degraded inputs, adeptly reconstructing fine facial features (FFHQ, row 2 and 5) and intricate object textures like butterfly patterns (ImageNet, row 2). AFDPS-ODE also provides coherent upscaled outputs, especially for FFHQ dataset, reaffirming the metrics in the tables.

Box Inpainting. In box inpainting combined with denoising, AFDPS-SDE shows robust performance, securing the highest PSNR on ImageNet-256 (23.15). Figure 6 highlights SDE's ability to generate detailed and realistically textured inpainted regions, such as the intricate dog fur (ImageNet, row 1) or sharp keyboard key structures (ImageNet, row 4). AFDPS-ODE also performs strongly, achieving best LPIPS on both datasets (FFHQ: 0.1969, ImageNet: 0.2716) and best PSNR on FFHQ (25.73), producing notably smooth and coherent fills, like seamless facial features (FFHQ, row 1).
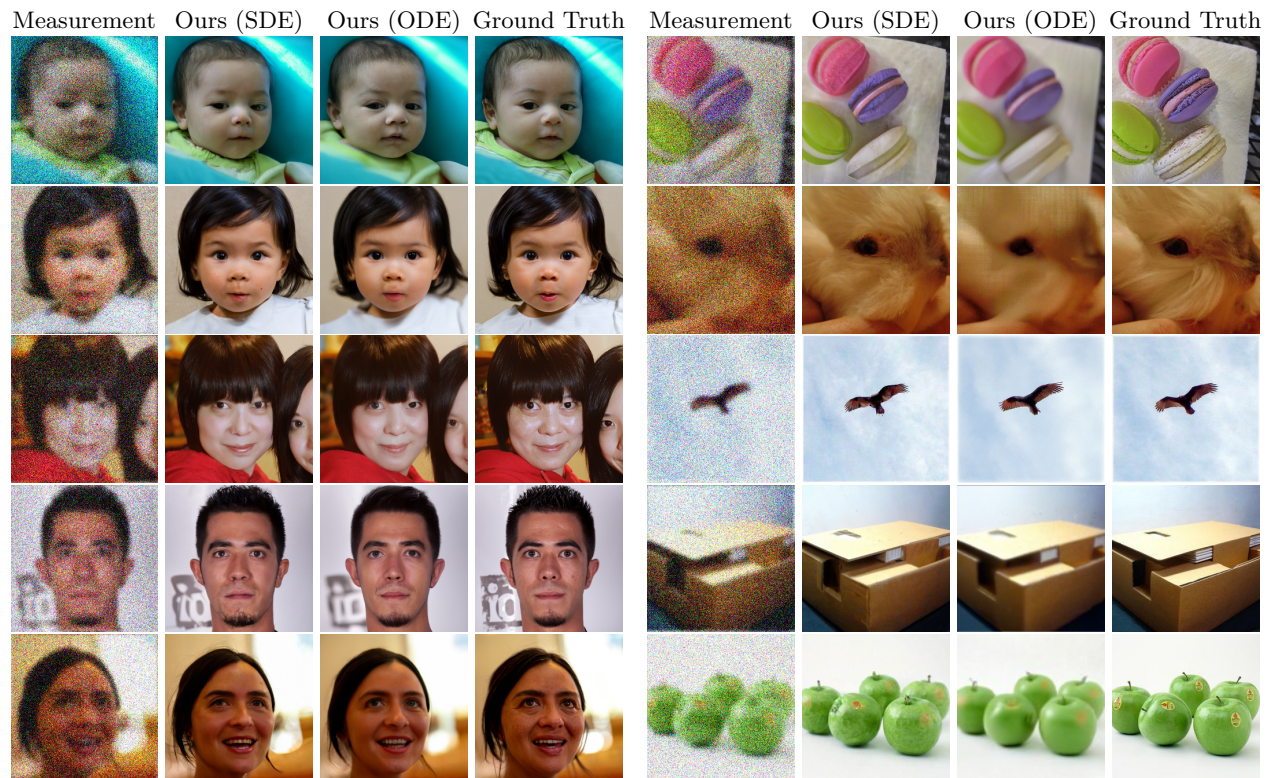
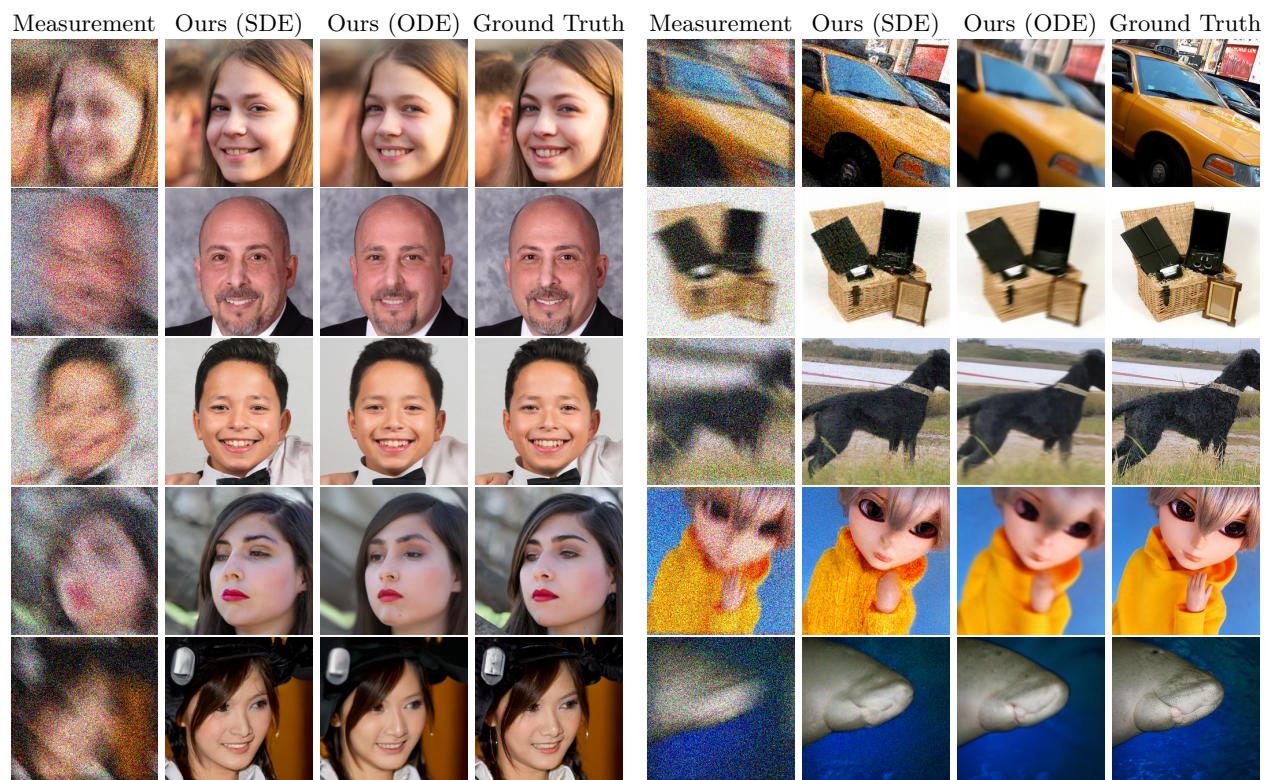Figure 3: Additional visual examples for the Gaussian deblurring problem on FFHQ and ImageNet.

Figure 4: Additional visual examples for the motion deblurring problem on FFHQ and ImageNet.
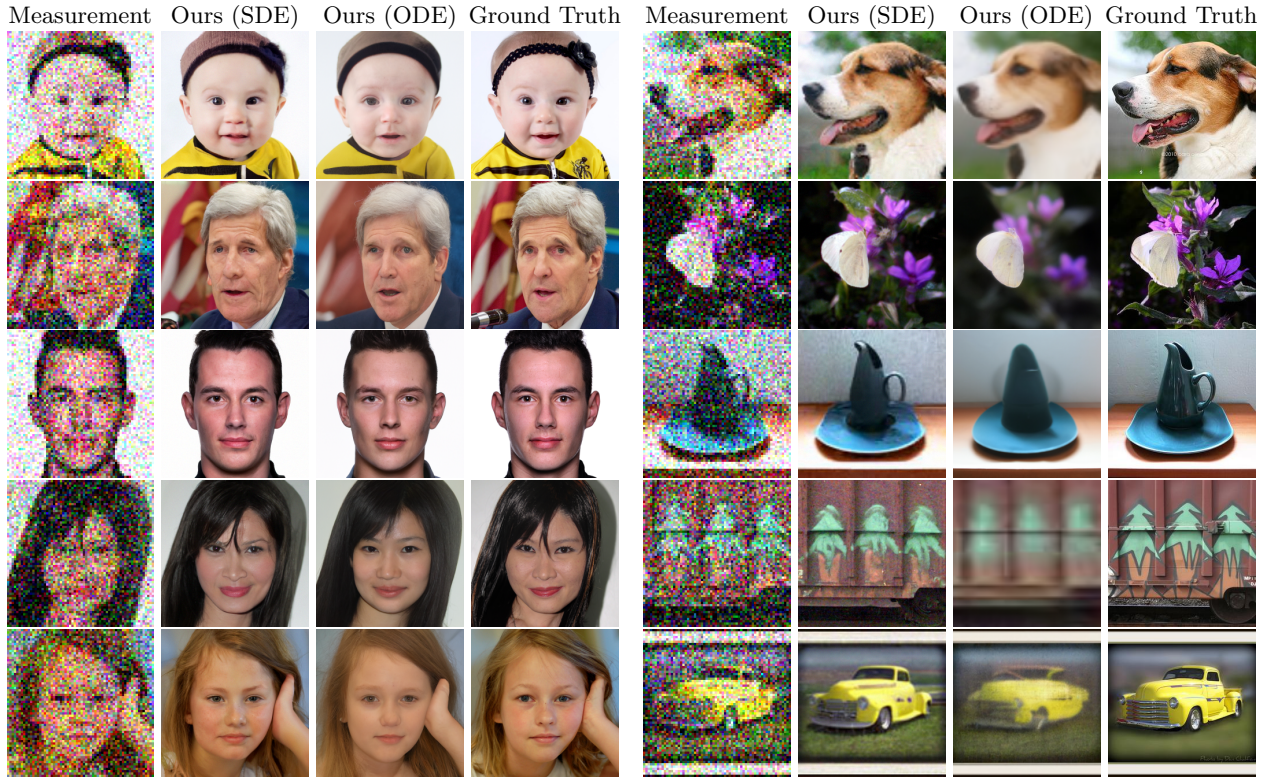
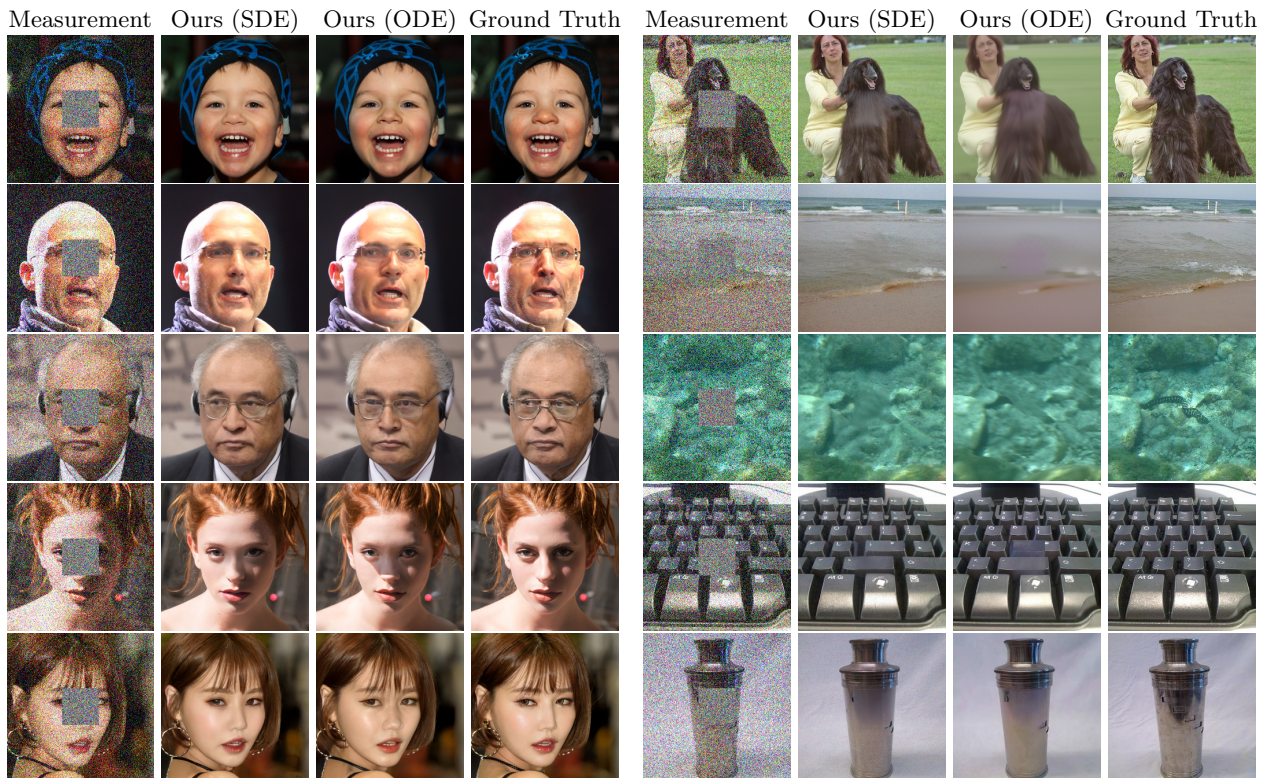Figure 5: Additional visual examples for the super-resolution problem on FFHQ and ImageNet.

Figure 6: Additional visual examples for the box inpainting problem on FFHQ and ImageNet.